

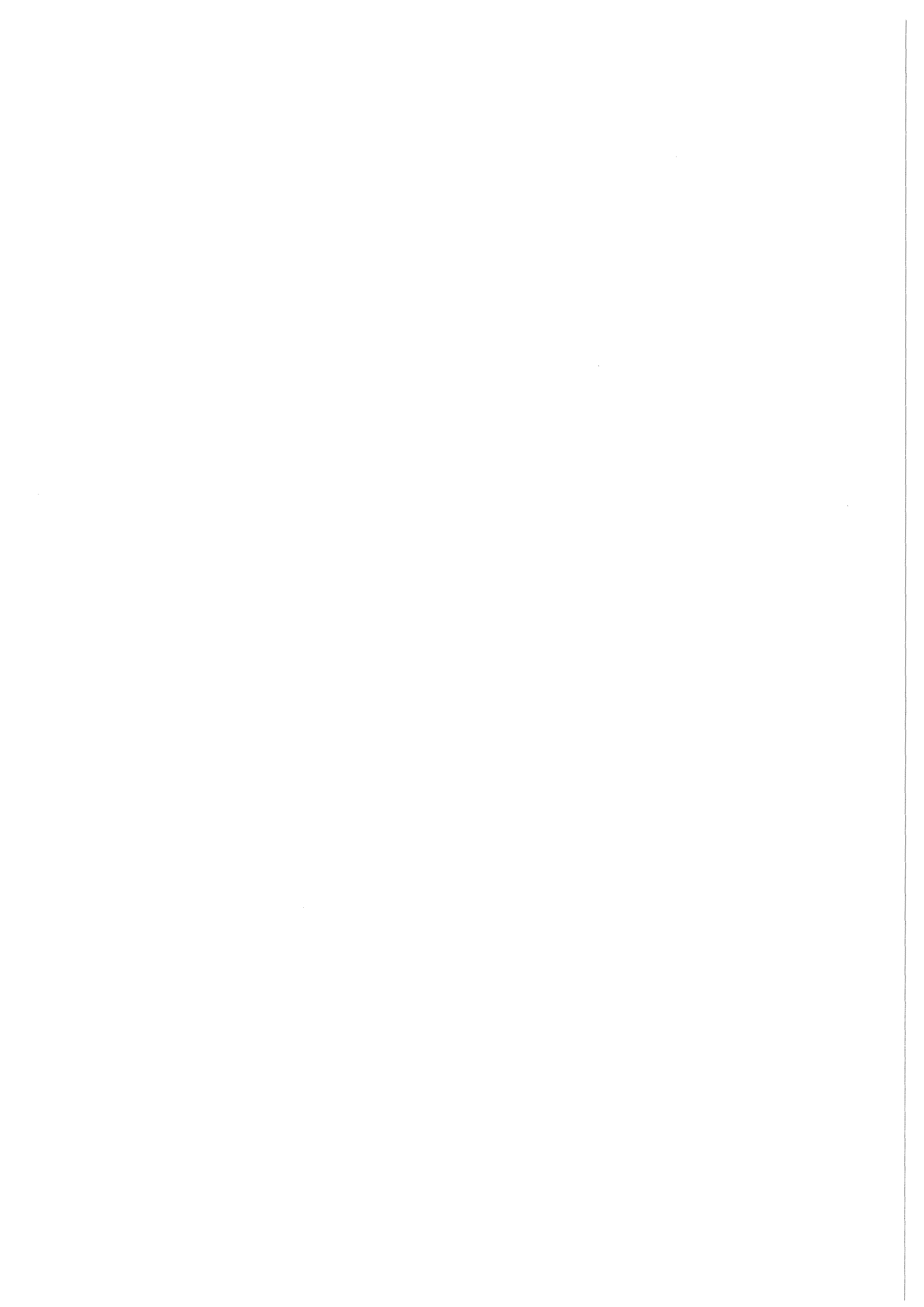
**KfK 4488
EUR 11392 EN
Oktober 1988**

**Nuclear Fusion Project
Semi-annual Report of the
Association KfK/EURATOM**

April 1988 - September 1988

Projekt Kernfusion

Kernforschungszentrum Karlsruhe



KfK 4488
EUR 11392 EN
Oktober 1988

**Nuclear Fusion Project
Semi-annual Report of the
Association KfK/EURATOM
April 1988 - September 1988**

compiled by
G. Kast

Kernforschungszentrum Karlsruhe

Als Manuskript vervielfältigt
Für diesen Bericht behalten wir uns alle Rechte vor

Kernforschungszentrum Karlsruhe GmbH
Postfach 3640, 7500 Karlsruhe 1

ISSN 0303-4003

Contents

	page
Report on Technology Tasks	
B1	Blanket Design Studies 1
B 2	Development of Computational Tools for Neutronics 4
B6	Corrosion of Structural Materials in Flowing Pb-17Li 6
B 6.3	Fatigue of Structural Material in Pb-17Li 7
B9	Tritium Extraction from Liquid Pb-17Li by the Use of Solid Getters 8
B 11-16	Development of Ceramic Breeder Materials 10
M1	The Large Coil Task 16
M 3	Development of High Field Composite Conductors 17
M 4	Superconducting Poloidal Field Coil Development 19
M 8	Design and Construction of a Poloidal Field Coil for TORE SUPRA as NET-Prototype Coil 22
M 9	Structural Materials Fatigue Characterization at 4 K 23
M 12	Low Electrical Conductivity Structures Development 25
MAT 1.6	Development and Qualification of MANET 1 27
MAT 1.9	Pre- and Post-Irradiation Fatigue Properties of 1.4914 Martensitic Steel 28
MAT 1.11	Post-Irradiation Fracture Toughness of Type 1.4914 Martensitic Steel 31
MAT 2.2	In-Pile Creep-Fatigue Testing of Type 316 and 1.4914 Steels 32
MAT 6/ MAT 13	Ceramics for First-Wall Protection and for RF Windows 33
MAT 9.2	Investigation of Fatigue Under Dual Beam Irradiation 36
MAT 18	Development of Low Activation Ferritic-Martensitic Steels 38
N1	Design Study of Plasma Facing Components 40
N2	Shield Design Studies 42
N3	Development of Procedures and Tools for Structural Design Evaluation 43
N5	Development of Theory and Tools for Evaluation of Magnetic Field Effects on Liquid-Metal Breeder Blankets 46
N6	Studies of Pebble Beds of Ceramic Compounds 49
RM1	Background Studies on Remote Maintenance 50

RM2	Mechanical Components Assembly	52
RM 3	Handling Equipment for In-Vessel Components	53
S + E 4.1.2	Safety Aspects of the Cryosystem	62
S + E 4.1.3	Safety Aspects of Superconducting Magnets	64
S + E 5.4	Overall Plant Accident Scenarios for NET	66
S + E 5.5	Development of Safety Guidelines for the Design of NET	67
S + E 7	Generic Environmental Impact Assessment for a Fusion Facility	68
T 6	Industrial Development of Large Components for Plasma Exhaust Pumping	69
T 7	Optimization of Cryogenic Vacuum Pumping of Helium	70
T 10 A	Plasma Exhaust Purification by Means of Cryosorption on Molecular-Sieves or alternative Adsorbents	72
T 10 C	Plasma Exhaust Gas Purification by Use of Hot-Metal Getters	73
T 10 E	Adsorption of DT on Heated Metal Beds other than Uranium	75
T 10 H	Catalyst Development for the Exhaust Purification Process	77
	Development of ECRH Power Sources	79
	NET Study Contracts	81
	Availability of the LCT Plant	81
	Investigation of the Vacuum and Exhaust Performance of NET	81
	Study about the NET TF Pancake Test	81
	Evaluation of Crack Growth Delay in Multilayer Sheets	82
	CAD Data Exchange between NET and KfK	82
	CAD Data Exchange for ITER	83
	NET Blanket Handling Device	83
Appendix I:	Table of Fusion Technology Contracts	86
Appendix II:	Table of NET Study Contracts	88
Appendix III:	KfK Departments contributing to the Fusion Projekt	89
Appendix IV:	Fusion Project Management Staff (PKF-PL)	90

B 1 Blanket Design Studies

Two design concepts are studied at KfK: a helium cooled ceramic blanket and a blanket with Pb-17Li eutectic as breeder material and coolant. The studies include small scale experiments and collaboration with industry for special feasibility problems.

In the reporting period a reorganization took place. The solid breeder blanket design studies are now part of a joint effort of KfK, CEA and ENEA. In the liquid breeder field a group consisting of CEA, KfK and JRC-Ispra was formed. Coordination of work is done by blanket executive groups.

1. Helium-cooled Ceramic Breeder Blanket

As already reported previously (progress report 1986 KfK 4076) measurements were made on the effective thermal conductivity of a pebble bed and of the heat transfer coefficient at the bed walls. Whereas in the previous measurements simulant materials were used a bed of 0.5 mm diameter Li_4SiO_4 pebbles was now available. Fig. 1 shows

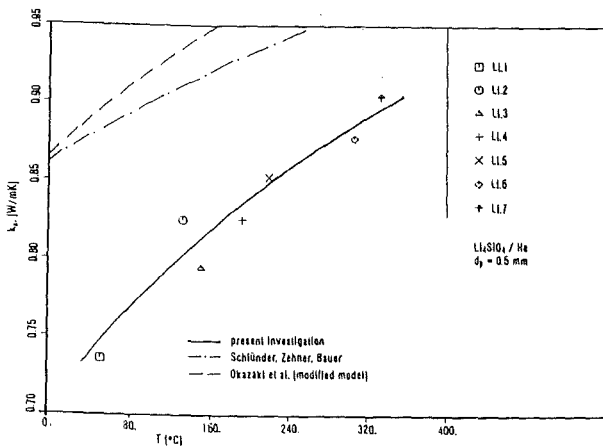


Fig. 1: Thermal conductivity of $\text{Li}_4\text{SiO}_4/\text{He}$ pebble bed, 0.5 mm diameter pebbles

the measured thermal conductivity vs. temperature together with model calculations /1/. In Fig. 2 the improvement of effective thermal conductivity is illustrated when a mixture of ceramic and beryllium pebbles is used. Such a modification could be necessary for fusion reactors of high neutron wall load.

The wall heat transfer coefficient is about $0.5 \text{ W/cm}^2\text{K}$. When a stainless steel wire gauze is located between bed and wall it decreases to about $0.1 \text{ W/cm}^2\text{K}$. The temperature drop at the wall still remains small as compared to the temperature gradient in the bed.

With respect to the NET-Test-objects it was stated that only a plug position will be needed rather than a full segment and that austenitic steel 316L shall be used as structural material. The DEMO relevant blanket design will however be based on the martensitic steel MANET.

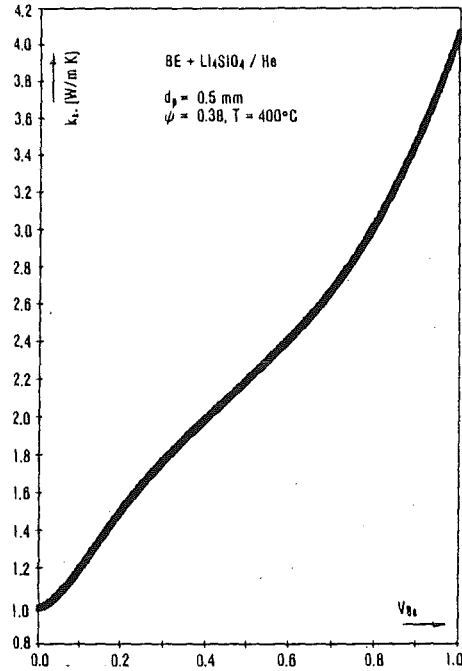


Fig. 2: Thermal conductivity of a mixture of Li_4SiO_4 - and beryllium pebbles as function of the Be volume fraction

Design studies for the coolant loops and the tritium recovery system were started.

The shielding properties of a solid breeder blanket are significantly worse than that of a steel/water shield module. Thus a detailed study with a three-dimensional Monte Carlo code was made /2/. The total neutron flux attenuation factor is 5 across the solid breeder blanket and 24 across the water/steel module. There is a strong poloidal peaking factor at the position of the superconducting coil. The impact of a gap between the segments is primarily an overall enhancement of the dose level which is a factor of about 1.2 for the solid breeder and a factor of 2.5 to 3 for the shield blanket.

Calculations are being made on the electro-magnetic forces induced by plasma disruptions. To assess the accuracy of the calculations a simple geometry experiment is in preparation which will be performed in ASDEX at Garching.

Staff:

L. Boccaccini
 E. Bojarsky
 M. Dalle Donne
 U. Fischer
 M. Kühle
 P. Norajitra
 G. Reimann
 H. Reiser
 G. Sordon

2. Liquid Metal-Cooled Blanket

The development of a blanket concept where the eutectic lithium-lead alloy Pb-17Li serves both as breeder material and as coolant has been continued. The goal of the blanket programme is to develop concepts for electricity producing reactors. Therefore, it has to be shown for each blanket concept that it can meet the conditions of a DEMO-reactor. These conditions are not really fixed but cover a range of required power density, thermal efficiency and life time.

As a first check of the reactor relevance, the NET-team has proposed the following minimum requirements for a DEMO-reactor blanket:

- Total tritium breeding ratio > 1.
- Average neutron wall loading $\geq 2 \text{ MW/m}^2$.
- Full power life time $\geq 20\,000 \text{ h}$.
- Coolant conditions for electricity production with $\eta_{\text{net}} \geq 20 \%$.

Based on these requirements, two alternative blanket concepts have been investigated, depending on the tokamak design:

A) The blanket, shown schematically in Fig. 3A, has a rather thick layer of beryllium as neutron multiplier in order to avoid the need for breeding blankets at the inboard side of the torus. This concept is suitable for a machine like NET, designed for blanket exchange in vertical direction. In this case both coolant inlet and outlet tubes have to be arranged at the top end of the torus, which makes the design of a self-cooled inboard blanket extremely difficult due to the higher magnetic field strength and the smaller space available at the inboard side of the torus.

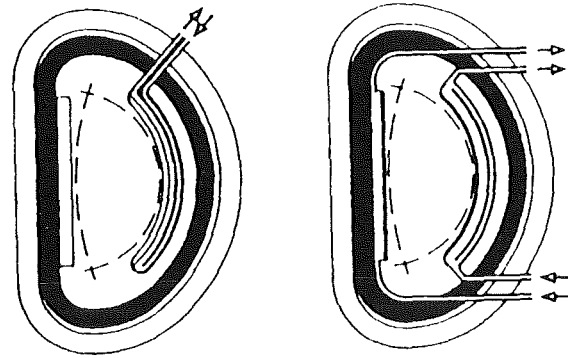
B) The blanket, shown schematically in Fig. 3B, does not need a beryllium multiplier, but inboard breeding instead. This concept, however, requires coolant access tubes at both the upper and lower end of the blanket segments in order to allow inboard blankets without excessive large MHD pressure drops.

Both concepts are based on the following features:

- Eutectic alloy Pb-17Li as breeding material/coolant.
- Ferritic steel as structural material.
- Poloidal-toroidal flow concept with integrated first wall.
- Laminated flow channel inserts installed in all poloidal ducts.

The neutronic performance of both blanket concepts has been analyzed on the basis of Monte Carlo calculations with the MCNP code. The analysis has been performed in a realistic three-dimensional geometrical representation of the DEMO double null configuration. The results of this analysis are shown in Table 1.

It is obvious that tritium self-sufficiency can be obtained for both blanket concepts in the DEMO double null configuration. Concept A requires roughly the same amount of beryl-



A) Inboard breeding only B) Outboard and inboard breeding

Fig. 3: Arrangement of breeding blankets and coolant access tubes

	concept A (with beryllium)			concept B (without beryllium)		
	3d	2d	1d	3d	2d	1d
Pb-17Li	1.05	1.26	1.27	1.07	1.47	1.52
Li-30	1.17	1.39	1.40	1.10	1.29	1.37
Li-nat	1.07	1.29	1.30	1.04	1.24	1.35

Table 1: Tritium breeding ratio of the liquid metal self-cooled blanket in the DEMO double null configuration, results from one-, two- and three-dimensional Monte Carlo calculations

lium as all other ceramic breeder or liquid breeder blanket concepts (in the range of 200 to 300 tons for a 2500 MW_{thermal} DEMO-reactor). The only exception is the self-cooled liquid metal breeder concept with breeding blankets arranged at the inboard and outboard side. In this case (concept B) no beryllium at all is needed to obtain tritium self-sufficiency.

The selected tritium removal technique for the self-cooled Pb-17Li blanket with an intermediate NaK loop consists of tritium permeation into the NaK and precipitation as tritide in a cold trap. For tritium recovery, the cold trap is heated up and the tritium is pumped off.

Presently, the building-up of the test loop for hydrogen (protium) precipitation is finished. Operation will start at the end of 1988.

Screening tests were performed to recover the hydrogen by thermal decomposition of the hydride. First, NaH-powder and NaH-crystals were decomposed, the latter were generated in the reaction vessel shown in Fig. 4.

This test apparatus is also used for the present experiments to generate hydride crystals in NaK and to investigate hydrogen recovery. The Figure 5 shows this new results and a comparison with the system NaH: The hydrogen release rate, characterized by the reaction coefficient k , is higher for NaK as long as hydrogen release by hydrogen bubbling exists. This increase can be explained by the higher saturation pressure of (NaK)-hydride. In contrast to Na, hydrogen release without bubbling plays a more important role. This release mechanism occurs at low temperatures and/or small values of the residual hydride mass. Presently, it is not clear, if the rate-determining step is the diffusion in the liquid metal or effects near the NaK-surface.

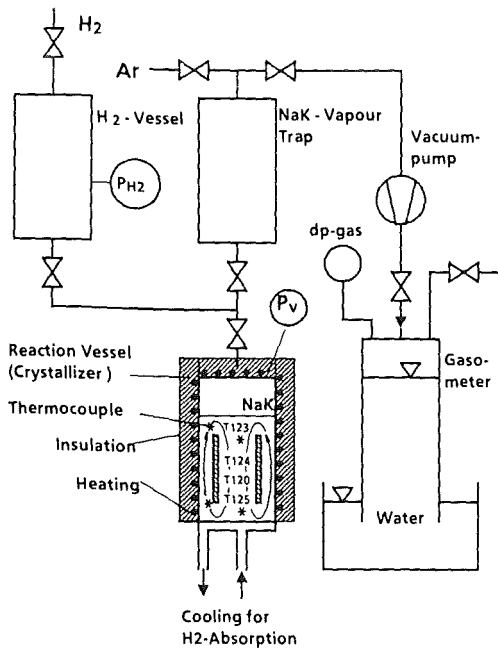


Fig. 4: Test Apparatus for Hydrogen Recovery

Staff:

- K. Arheidt
- H.J. Brinkmann
- V. Casal
- H. Deckers
- G. Eisele
- U. Fischer
- H. John
- S. Malang
- D. Rackel
- J. Reimann
- H. Reiser
- K. Rust

Publications:

1. M. Dalle Donne and G. Sordon:
Measurements of the Effective Thermal Conductivity of a Bed of Li_4SiO_4 Pebbles, 15th Soft, Utrecht, September 19-23, 1988

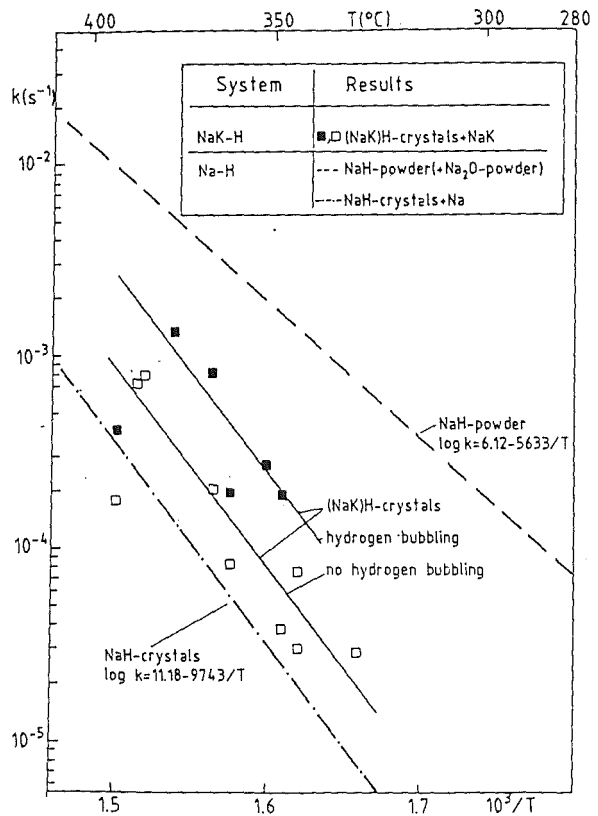


Fig. 5: Arrhenius Plot of Reaction Coefficient

2. U. Fischer:
Montecarlo Shielding Analysis in the Double-Null configuration of NET, 15th Soft, Utrecht, September 19-23, 1988
3. S. Malang, K. Arheidt, U. Fischer:
Test Module in NET for a Self-cooled Liquid Metal Blanket Concept. 15th Symp on Fusion Technology, Utrecht, 19-23 Sept. 1988.
4. K. Rust, S. Malang, G. Schmidt:
Thermo-mechanical Analysis of a self-cooled outboard Blanket. 15th Symp. on Fusion Technology, Utrecht, 19-23 Sept. 1988.
5. J. Reimann:
Tritium Separation from Pb-17Li Permeation into NaK and cold trapping: First Experiments on Recovery from cold Traps. 3rd Top. Meet. on Tritium Technology in Fission, Fusion and Isotopic Applications, Toronto, Cd, May 1-6, 1988.
6. J. Reimann, H. John, S. Malang:
Tritium Separation and Recovery from NaK by cold Traps: Results on Hydrogen Recovery from Na and NaK. 15th Symp. on Fusion Technology, Utrecht, 19-23 Sept. 1988.

B 2 Development of Computational Tools for Neutronics

The KfK-activities to improve the computational tools for fusion neutronics comprise the evaluation and processing of relevant nuclear data, the development of new calculational procedures as the adoption of existing methods and programmes for use in fusion neutronics.

The efforts to develop a general transport code system for a rigorous treatment of the neutron scattering have been further continued. The development of the two-dimensional transport module ANTRA 2, based on the TWOTRAN transport programme, is being finalized. At present ANTRA 2 is tested numerically.

The study on the multiplication of 14 MeV neutrons in beryllium, based on the consistent use of double-differential cross-section data (DDX) from the European Fusion File EFF-1, has been further continued. New experimental data on the neutron multiplication of thin beryllium spherical shells, performed at the Kurchatov Institute Moscow and at the University of Texas Austin, have become available at the ISFNT-conference at Tokyo. Good agreement is obtained between the measured and the calculated neutron multiplication. This further supports the rather well established $(n, 2n)$ -cross-section evaluation of beryllium. For larger shell thicknesses (> 8 cm), however, the energy-angle distribution of the scattered neutrons becomes important for the neutron multiplication. However, large uncertainties exist for this distribution, and, furthermore, no reliable experimental data are available for the neutron multiplication of thick beryllium spherical shells, but rather incomplete and contradictory data. Thus there is still a strong need for integral beryllium experiments including the measurement of the neutron leakage energy spectra.

The Monte Carlo code MCNP is in use for fusion applications at KfK. The actual version 3A already had been implemented on the KfK computing facility during the last semi-annual period. Meanwhile its handling has been made more efficient by installing the plotting module for interactive operation.

MCNP has been proven to be very powerful for analyzing shielding and neutron streaming problems. Various problems of this kind have been analyzed for NET (see section B1), including the penetration of 14 MeV neutrons through a 3 m thick steel slab and the streaming effect in a 2 cm wide gap throughout the slab. Fig.6, shows the two-dimensional model used for analyzing the neutron streaming through toroidal blanket segment gaps of NET and its impact on the shielding performance of the vacuum vessel. Several variance reduction techniques, that are available in MCNP, have been applied in these calculations to assess their potentials and limitations: the importance sampling technique with geometry splitting and Russian roulette has been proven to be very reliable and very efficient; its application is straight forward and provides physical insight into the problems treated. The application

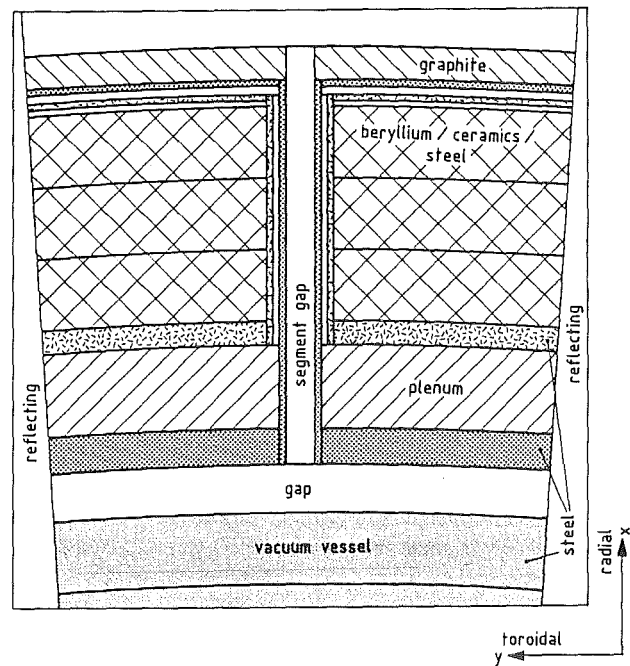


Fig 6: Two-dimensional sector model of NET for analyzing the neutron streaming through the blanket segment gaps

of the automatically self-generated weight window, on the other hand, seems to be somewhat inefficient and insufficient: it requires several long computing runs to generate an appropriate weight window set (varying in space and energy), and yet its spatial variation remains unsatisfactory, if it is not improved manually.

The work on the neutron emission spectra for continuum inelastic scattering on Cu has been completed and documented in an internal report. The new 'test data', which take into account preequilibrium reactions on the basis of the geometry dependent hybrid model of M. Blann, have been applied in integral calculations. The influence of the data on the leakage spectrum of a copper sphere already had been described previously. In the meantime we also investigated neutron flux density spectra in a copper layer of 4 cm thickness within a spherical assembly consisting mainly of beryllium. The calculations were performed with the two-dimensional transport code TWODANT in 171 energy groups and S_{16}/P_3 -approximation. The spectra in the copper layer clearly show the influence of the preequilibrium data; the effect, however, is much smaller than the one we found for the leakage spectrum of the Cu-sphere. Relative deviations between spectra calculated with the new copper data and spectra calculated with the data of the VITAMIN-C library are about - 40 % in the energy region around 4 MeV and about + 25 % in the energy region around 11.5 MeV. For the leakage spectrum of the copper sphere we obtained relative deviations of about - 60 % for energies around 4 MeV and + 290 % for energies around 11 MeV.

it is intended to use the new 'test data' of copper for the coupled neutron photon group constant set, that is in preparation at KfK.

Publications:

U. Fischer: Monte Carlo Shielding Calculations in the Double
Null Configuration of NET, KfK-4411, May 1988

Staff:

I. Broeders

U. Fischer

B. Krieg

H. Küsters

A. Schwenk-Ferrero

E. Stein

E. Wiegner

B 6 Corrosion of Structural Materials in Flowing Pb-17 Li

A second test series in the PICOLO loop at a test temperature of 500°C was started in January 1988, first results gained with specimens of the NET batch of steel 1.4914 are now available. As in the first test series, the velocity of the liquid alloy Pb-17Li was maintained at 0.3 m/s corresponding to a Reynolds number of 20950. The temperature gradient in these tests was ~200K.

Weight and diameter controls of selected specimens were performed after 1000, 3000 and 4117 hours of exposure in the test section of PICOLO. The measurements of diameters of the corroded specimens indicated that the removal of material was varying along the circumference of the cylindrical specimens. Fig. 7 shows the corrosion effects around the specimen no. 12, which was exposed for 3000 hours. Such diameter analyses were used as the basis for a kinetic study of the average losses of material in the corrosion test series. As in the earlier test series which was performed at 550°C, an initial period was observed showing a lower corrosion rate. After an exposure time larger than 3000h the corrosion rate was considerably larger. It cannot yet be concluded that a steady state corrosion was already reached. The initial corrosion rate was lower than at 550°C, the accelerated corrosion of the roughened specimens exhibited a similar relationship as in the first test series. Fig. 8 compares the results which have been gained so far in the PICOLO loop. Metallic and non-metallic contaminants of the eutectic alloy were chemically analyzed.

The chemical activity of oxygen in the liquid alloy Pb-17Li was estimated by means of electrochemical oxygen meters. The solid electrolytes used for these meters were tubes of calcia stabilized zirconia (CSZ) resp. yttria stabilized zirconia (YSZ), the system indium/indium oxide served as reference electrode. The cell voltages of Pb-17Li saturated with lithium oxide and after removal of oxygen by means of gettering with zirconium or yttrium were only slightly different. This indicates a low solubility of oxygen in the liquid alloy. The oxygen contents were also measured in parallel analyses by means of the vacuum hot extraction method. The chemical activity of lithium in the liquid eutectic could be deduced from these measurements. At 600°C a_{Li} was found to be $\sim 10^{-5}$ at a concentration of 17 at-% Li. The temperature gradient is given by the equation

$$\log a_{Li} = 0.795 - \frac{3591}{T(K)}$$

Staff:

Ch. Adelhelm	G. Frees
N.P. Bhat	Z. Perić
H.U. Borgstedt	G. Streib
G. Drechsler	S. Winkler

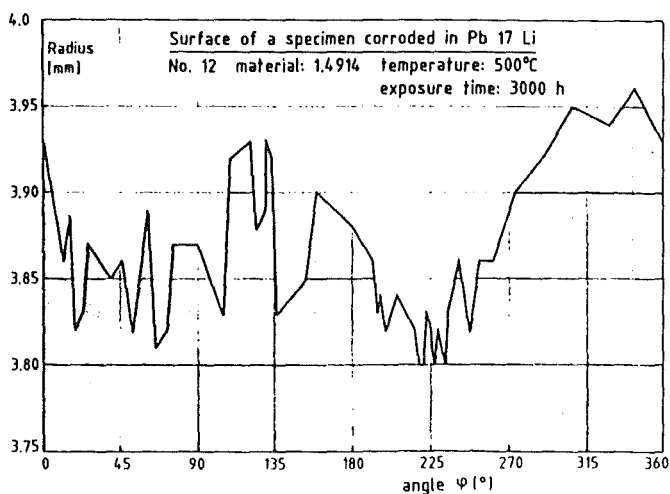


Fig. 7: Depth of corrosion around one circumference of the specimen no. 12 (3000h at 500°C).

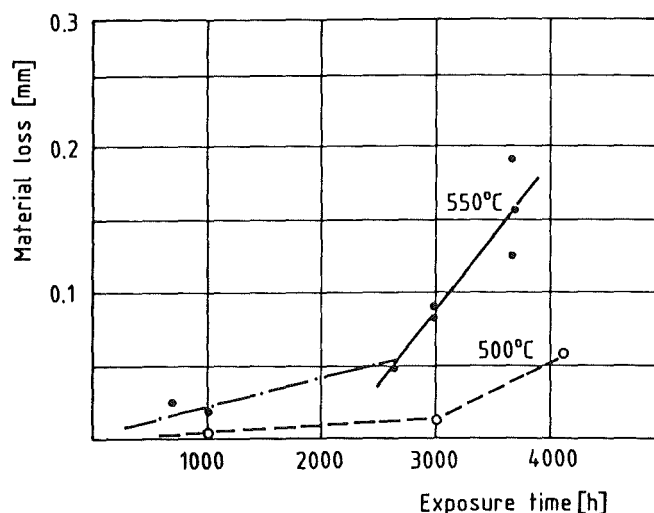


Fig. 8: Results of corrosion tests of steel 1.4914 in PICOLO at 550 and 500°C

Publications:

1. Z. Perić, G. Drechsler, G. Frees, H.U. Borgstedt, The Corrosion of Steels in Liquid Pb-17 Alloy, Fourth Internat. Conf. on Liquid Metal Engineering and Technology, 17-21 October 1988, Avignon, France, Paper 522
2. N.P. Bhat, Ch. Adelhelm, H.U. Borgstedt, Oxygen Measurements in Liquid Pb-17Li Eutectic, Fourth Internat. Conf. on Liquid Metal Engineering and Technology, 17-21 October 1988, Avignon, France, Paper 623

B 6.3 Fatigue of Structural Material in Pb-17Li

A series of lcf-tests of specimens (21mm gauge length, 8.8 mm minimal diameter, hour-glass shape) of the martensitic steel X 18 Cr Mo V Nb 12 1 (1.4914) has been completed. The tests were made with thermally treated (see semi-annual report KfK 4418, page 12) material in stagnant Pb-17Li and in argon and with pre-corroded specimens in the liquid metal. The pre-corrosion was performed in static capsules in which the specimens were exposed for 1000 hours at 550°C.

The average values of numbers of cycles before failure are compared in Fig. 9. The life time of the specimens is larger in the liquid metal than in the gaseous environment, even after a pre-corrosion of the material, though a pre-corrosion gradually reduces the number of cycles before failure.

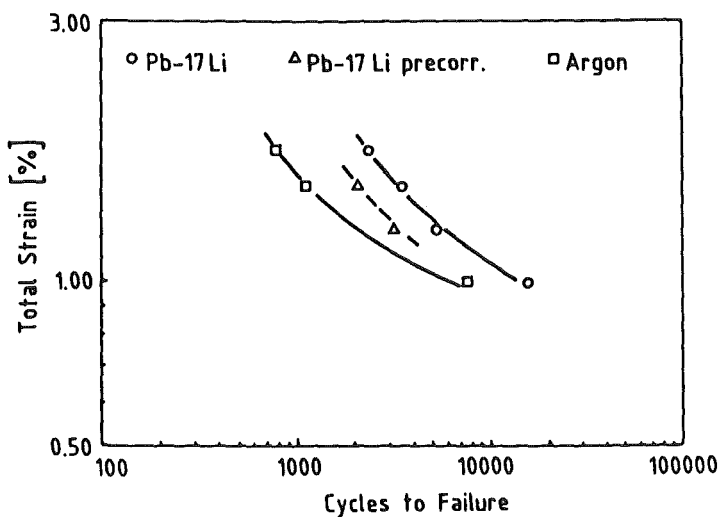


Fig. 9: Fatigue life of 1.4914 NET as a function of the total strain amplitude in Argon atmosphere and in Pb-17Li.

Staff:

H.U. Borgstedt
M. Grundmann
Z. Perić
B. Seith

Publications:

1. H.U. Borgstedt, M. Grundmann, The influence of liquid Pb-17Li eutectic on the mechanical properties of structural materials. Fusion Engineering and Design 6 (1988)
2. M. Grundmann, H.U. Borgstedt, M. Schirra, The creep-rupture behaviour of the martensitic steel X 18 Cr Mo V Nb 12 1 (no. 1.4914) in liquid Pb-17Li at 550 and 600°C. Fourth Internat. Conf. on Liquid Metal Engineering and Technology, 17-21 October 1988, Avignon, France, Paper 511.

B 9 Tritium Extraction from Liquid Pb-17Li by the Use of Solid Getters

Several methods were proposed for the extraction of tritium from a liquid Pb-17Li blanket. Task B9 is concerned with the use of solid getters.

A delay in the start-up of the facility TRITEX was used to study the behavior of deuterium in a small thermal convection loop, THERCOL-3.

The loop was fabricated from steel 1.4571. Its main piping was a tube with 10 mm inner diameter and a wall thickness of 2 mm. About 4 kg of the molten eutectic were circulating. There were expansion volumes with separated covergas supplies on top of the hot and the cold leg. In each expansion volume a thin walled spiral tube made of low carbon α -iron was submerged into the molten alloy.

Deuterium was dissolved in the Pb-17Li from sample gas streams with partial pressures between 1 and 1000 mbar. Two kinds of dissolution has been investigated: permeation from the sample gas through one of the iron tubes into the liquid metal, and direct dissolution of deuterium in the liquid metal via the covergas interface. Because of losses of deuterium by permeation, no equilibrium between the sample gas and the liquid eutectic was attained. The measured partial pressure of deuterium over the eutectic was always more than one order of magnitude lower than in the sample gas.

Results

The figure shows permeation rates for deuterium through low carbon α -iron. Line 1 was measured for the permeation from a gas phase through the iron into a pure argon gas phase at the down stream side. The permeation rates are lower than expected from the literature (1), the activation energy higher (line 2). Such an effect was already observed for the ferritic steel 1.4922 (2) and is probably caused by chemical reactions between the deuterium and thin oxide layers on the metal surface.

Line 3 was obtained using THERCOL-3: deuterium was permeating from a gas phase through the iron into liquid Pb-17Li. The measurements were done using a sample gas with a deuterium partial pressure of 100 mbar.

The influence of the Pb-17Li on the deuterium permeation is remarkable. At 600 °C the permeation rate is reduced by a factor of 10, the difference is smaller at lower temperatures. The activation energy for the permeation dropped from -68 kJ/mol in case of permeation from a gas into a gas at the down stream side to -23 kJ/mol for the permeation into the liquid eutectic.

A similar effect was recently observed (3) (4) for the permeation of hydrogen through stainless steel 316. It was attributed to the permeation resistance of a stagnant Pb17Li boundary layer near the steel surface. The activation energy

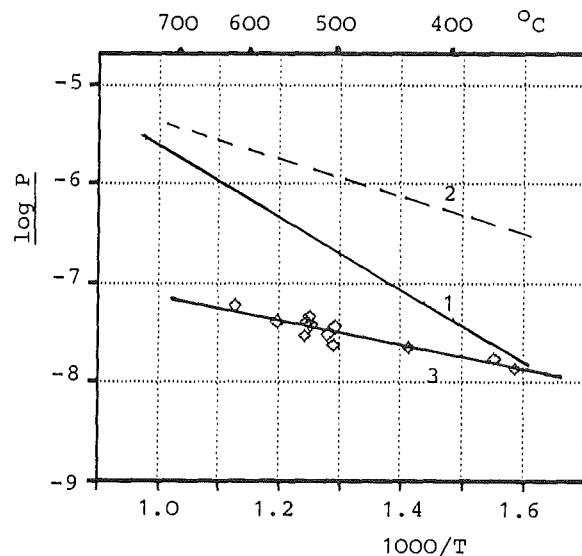


Fig. 10: Permeation rates for deuterium through low carbon α -iron.

P is given in $(\text{mol} \cdot \text{mm} / \text{s} \cdot \text{m}^2 \cdot \text{mbar}^{1/2})$.

Measurements with a deuterium partial pressure of 100 mbar. Line 1 permeation from a gas phase through the membrane into another gas phase.

Line 2 function of Gonzales (1) for α -iron. Line 3 permeation from a gas phase through the membrane into Pb-17Li.

for the permeation was reduced by the Pb-17Li from -51 to -33 kJ/mol.

The dissolution rates of deuterium into Pb-17Li from a covergas phase were found within a factor of 2 to 10 identical with the permeation rates through α -iron. This observation is in agreement with the assumption of the influence of a Pb-17Li boundary layer.

Summary

The permeation rate of deuterium from a gas through an α -iron membran was strongly reduced if the down stream side of the membran was immersed into molten Pb-17Li. This effect is probably caused by the diffusion resistance of a liquid metal boundary layer. Such a boundary layer is also effective in the case of the dissolution of deuterium from a gas phase into the molten eutectic.

Staff:

H. Feuerstein

H. Gräbner

S. Horn

References:

- [1] A.D. LeClaire, AERE-R-10598 (1982)
- [2] H. Feuerstein et.al., ICFRM-3, Karlsruhe,
Oct. 4-10, 1987
- [3] A. Viola and G. Pierini, Tokio 1988
- [4] O. Gautsch and G. Hoddap, J. Nucl. Mater. 152
(1988)
35-40

B 11 - 16 Development of Ceramic Breeder Materials

The KfK contribution concentrates on the Li-Silicates and includes all the steps necessary to achieve a product to be used in the helium-cooled blanket design. The development starts with fabrication and characterization of pellets and pebbles. Physical, mechanical and chemical properties are measured before and after irradiation. The irradiation program makes use of several reactors within the European and the Beatrix Cooperation. Lithium-Orthosilicate has been proven to be the most promising candidate for the NET reference ceramic breeder material.

1. Fabrication and Characterization of Breeder Materials (B11, B12)

The preparation and characterization of lithium containing monosilicates, especially Li_4SiO_4 , and lithium metazirconate, Li_2ZrO_3 , are under development to be used as breeder materials for fusion reactors within the European Fusion Program (Task B11 and B12). Progress has been obtained in preparation of ceramic Li_4SiO_4 sintered granulates using an experimental fluidized-bed equipment for sintering of the prepared granulates. Samples of pellets with cylindrical shape were prepared from aluminium doped orthosilicate powders, $\text{Li}_{4-3x}\text{Al}_x\text{SiO}_4$, and lithium metazirconate powders, to be irradiated within the German-French experiment LILA / LISA 1, which is of special interest for a low-temperature fusion blanket concept.

Characterization of Ceramic Breeder Materials

The release of tritium from the ceramic breeder material in a helium-cooled blanket depends on several factors. One of these factors is the specific surface area of the material. One method of its determination is based on the theory developed by Brunauer, Emmett, and Teller about the adsorption of nitrogen at its boiling point and the measurement of the nitrogen volume adsorbed. This method was applied to analyze lithium orthosilicate specimens of different shapes (pellets, spheres, sintered granulates, and small molten spheres) which had been fabricated following different fabrication routes. The values of the specific surface areas found with pellets and spheres of densities between 2.1 and 2.3 g/cm^3 ranged from 0.2 to 2.2 m^2/g . Pellets of densities between 1.7 and 1.9 g/cm^3 showed values larger than 6 m^2/g . The values determined for sintered granulates and small molten spheres lay between 2 and 6 m^2/g .

Parallel to the experimental determination by means of the method mentioned above the specific surface area was calculated using two simple structure models. One model simplifies the grains of the material by spheres of uniform mean diameter which can be deduced by methods of image analysis. The other model describes the open porosity of the material which is measured by means of mercury porosimetry by cylindrically shaped channels of uniform mean diameter. The values resulting from the two models

differ, in general, significantly from each other (Table 2). The measured values of the high-density pellets lay between the calculated values, those of the mean - and low - density spheres and pellets, respectively, were larger than the calculated ones. This comparison demonstrates that the use of structure models for theoretical calculations is insufficient. Measured values are more realistic.

Experiment	Specimen density (g/cm^3)	Specific surface area according to		
		sphere model (m^2/g)	cylinder model (m^2/g)	measurement (m^2/g)
VOM-23H	2.11	0.11	0.17	2.2
LISA 1	2.27	0.05	3.3	0.77
LISA 2	2.18	0.07	3.1	0.20
DELICE 02	1.89	-	0.26	6.1
ELIMA	1.71	0.05	0.17	6.36
	2.15	0.03	4.4	1.54

Table 2: Specific surface areas of various lithium orthosilicate specimens of some irradiation experiments

The helium-cooled blanket module which is designed by KfK involves the ceramic breeder material in the form of a pebble bed. Permeation measurements have been carried out with various test beds in order to determine permeation coefficients which are needed for the calculation of the pressure drop across the pebble bed canisters. Values were found between 1 and 2 $\cdot 10^{-6} \text{ cm}^2$ according to the densities of the beds.

Preparation of Ceramic Sintered Granulates

Granulates of lithium orthosilicate, prepared by powder metallurgical techniques, have been rounded and sintered in a fluidized-bed equipment at temperatures of up to 1150 $^{\circ}\text{C}$. Such sintered granulates showed to be more spherical in shape and the surfaces of the sintered granulates are much more flattened as compared to granulates sintered in a rotating kiln. The rub-off behavior of such granulates is negligible small under mechanical treatment. Further development is needed to obtain a higher bulk density of the granulates, which up to now mainly depends on the geometrical shape of the sintered granulates

Chemical analysis was carried out on lithium orthosilicate after different sintering temperatures concerning the main constituents and metallic impurities.

Preparation of Pellets for the LILA / LISA 1 Irradiation Experiment

It has been shown from first irradiation experiments that lithium metazirconate (Li_2ZrO_3) and aluminium doped orthosilicate ($\text{Li}_{3,7}\text{Al}_{0,1}\text{SiO}_4$) have a better behavior in tritium release at low temperatures (300 to 350 °C) as compared to the pure lithium orthosilicate. Pellets of these materials have been prepared to be irradiated in the LILA / LISA 1 experiment with tritium extraction by purge gas. The preparation of the doped orthosilicate was carried-out following the suspension method in methanol, already described in detail. As starting materials aluminum isopropoxide ($(\text{C}_3\text{H}_7\text{O})_3\text{Al}$), LiOH, and SiO_2 ("Aerosil") have been used in stoichiometric amounts. The metazirconate has been prepared from a suspension of LiOH in zirconium n-propoxide ($(\text{C}_3\text{H}_7\text{O})_4\text{Zr}$), which has been hydrolyzed by addition of water and subsequently distilling-off the propanol. The suspensions have been spray-dried, and the powders obtained have been calcinated, pressed, and sintered to specified shape (see Table 3).

material	number of samples	shape of samples	density (% TD)
$\text{Li}_{0,7}\text{Al}_{0,1}\text{SiO}_4$	10	8 mm \varnothing 8 mmH	~ 90
Li_2ZrO_3	10	8 mm \varnothing 8 mmH	≥ 80
Li_4SiO_4	10	8 mm \varnothing 8 mmH	≥ 90
additional 40 pellets of each material were prepared for characterization and chemical analysis			

Table 3: Irradiation samples for the LILA / LISA 1 experiment

Publications:

D. Vollath, H. Wedemeyer, E. Günther, H. Elbel:
"Semi-Industrial Production of Li_4SiO_4 Powder and Pebbles",
International Symposium on Fusion Nuclear Technology (ISFNT), 10.-19.4.1988, Tokyo

A. Skokan, D. Vollath, H. Wedemeyer, E. Günther, H. Werle:
Preparation, Phase Relationships and first Irradiation Results of Lithium Orthosilicate doped with Al^{3+} - and P^{5+} -Ions, 15th Symposium on Fusion Technology (SOFT), 19.-23.9 1988, Utrecht

Staff:

- B. Dörzapf
- H. Elbel
- E. Günther
- R. Hanselmann
- J. Heger
- W. Laub
- H. Nagel
- R. Scherwinsky
- D. Vollath
- Dr. H. Wedemeyer
- M. Wittmann
- C. Adelhelm
- S. Winkler

2. Measurement of Physical, Mechanical and Chemical Properties (B 13)

Physical and Mechanical Properties

A comparative evaluation was made for mechanical properties of Li_4SiO_4 , which is based on data measured at KfK and ANL. It proved to be possible to propose correlations with the microstructure parameters porosity P and grain size d. The Young's modulus will mainly depend on the porosity and can be represented by the correlation $E = 110 (1 - P)^3$ GPa for a well developed microstructure (Fig. 11). The best fit for the bend strength data (ANL) resulted to be $\sigma_b = 195 (1 - P)^3 \cdot d^{-0.44}$ MPa (d in μm), which should be converted to a $d^{-0.5}$ dependence for general application. For the compressive strength a first approximation was given by $\sigma_c = 975 (1 - P)^{1.5} \cdot d^{-0.44}$ MPa (d in μm), but the data base (KfK) was still poor. It seems possible that a larger dependence on the porosity has to be considered, as found for Li_2SiO_3 of well developed microstructure: $\sigma_c = 1800 (1 - P)^3 \cdot d^{-0.5}$ MPa (d in μm).

It was impossible to find a common correlation for the creep rate data from compressive creep tests on Li_4SiO_4 samples. This is probably due to the far different pressure loads applied in the comparable temperature range (850 - 950 °C), which were 10 MPa at KfK and mostly ≥ 100 MPa at ANL. The creep mechanism seems to be sensitively dependent on the stress.

Staff:

- M. Blumhofer
- H. Zimmermann

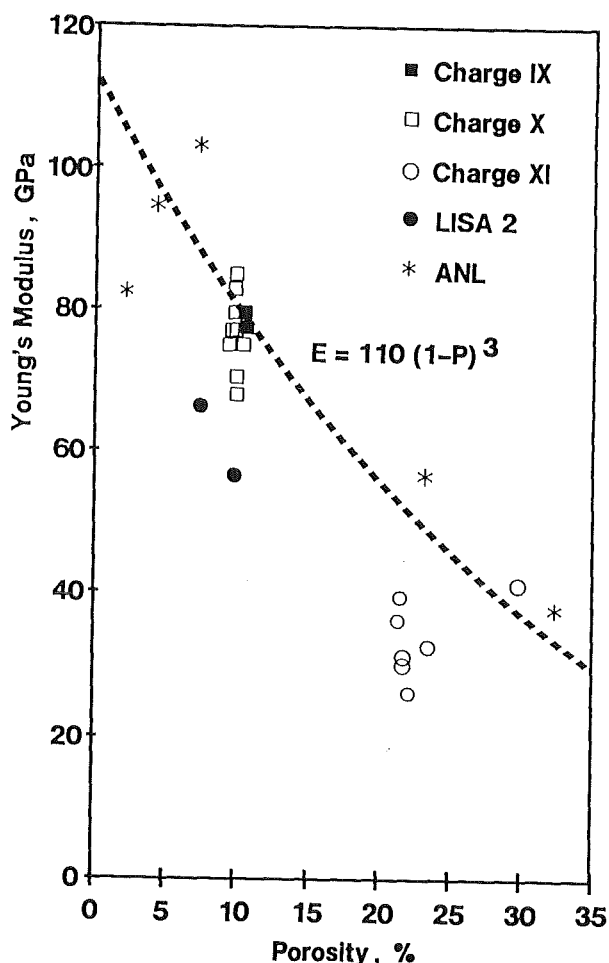


Fig. 11: The porosity dependence of the Young's modulus of Li_4SiO_4 .

Constitution, Interaction with Water Vapour

The experimental investigation of the $\text{Li}_2\text{O}-\text{ZrO}_2$ phase relations was continued in the region $\text{Li} : \text{Zr} < 2$. Between 800 and 1460 °C no intermediate compounds of Li_2ZrO_3 and ZrO_2 were found, in accordance with literature. The interpretation of an endothermal effect at 1460 °C needs further investigations.

The uptake of water vapour by dried Li_4SiO_4 samples was studied at three temperatures (25, 200 and 500 °C) by transient release experiments up to 850 °C (5 °C/min). Depending on the temperature during the adsorption, H_2O is released in several distinct steps. This result points to different bonding conditions. From the samples loaded with water vapour at ambient temperature the release occurs at ~ 100, ~ 150 and ~ 300 °C, similar to SiO_2 and TiO_2 . These samples loaded at 200 °C show only one peak at ~ 300 °C, except when the loading time is prolonged to ~ 400 h. Then an additional flat release maximum at ~ 400 - 500 °C is observed. H_2O loading tests at 500 °C show that at this temperature no water vapour is adsorbed. The association of the distinct release steps to the different bonding mechanisms (physically adsorbed water, capillary water, chemisorbed

water or water dissolved in the Li_4SiO_4 matrix) is under investigation by comparison of the heat effects

Staff:

- C. Adelhelm
- D. Linder
- V. Schauer
- G. Schlickeiser
- A. Skokan

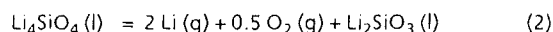
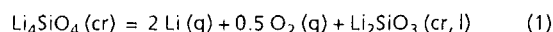
The Thermochemistry of Lithium Orthosilicate

A useful experimental technique to study the thermochemical properties of breeder ceramics consists in the mass spectrometric analysis of Knudsen effusates. The method was been applied to Li_4SiO_4 samples.

The measured ion intensities I_i in the Knudsen cell are converted into partial pressures p_i of the species i employing the equation

$$P_i = K \frac{I_i \cdot T}{\sigma_i \gamma_i x_i}$$

where K is a calibration constant of the instrument, σ_i is the ionization cross section of an atom or molecule i , γ_i is the electron multiplier gain and x_i is the atom fraction of the measured isotope. Fig. 12 shows the partial pressures of the liquid lithium orthosilicate as a function of temperature. Since the LiO peak ($m/e = 23$) is perturbed by background. Na the partial pressure of this species were confirmed using Li_4SiO_4 enriched in Li-6 (the synthesis of this compound was carried out at the IMF by Dr. Wedemeyer). From the obtained data the following mechanism can be derived to describe the main vaporization process of solid and liquid lithium orthosilicate:



A second process described by the equations



contributes to the decomposition to a lesser extent (see Fig. 12).

Average reaction enthalpies calculated from equilibrium constants and Gibbs free energy functions are summarized in Table 4.

From these data and the heat of sublimation of crystalline Li_2O (427.814 kJ/mol) the enthalpy change for the reaction

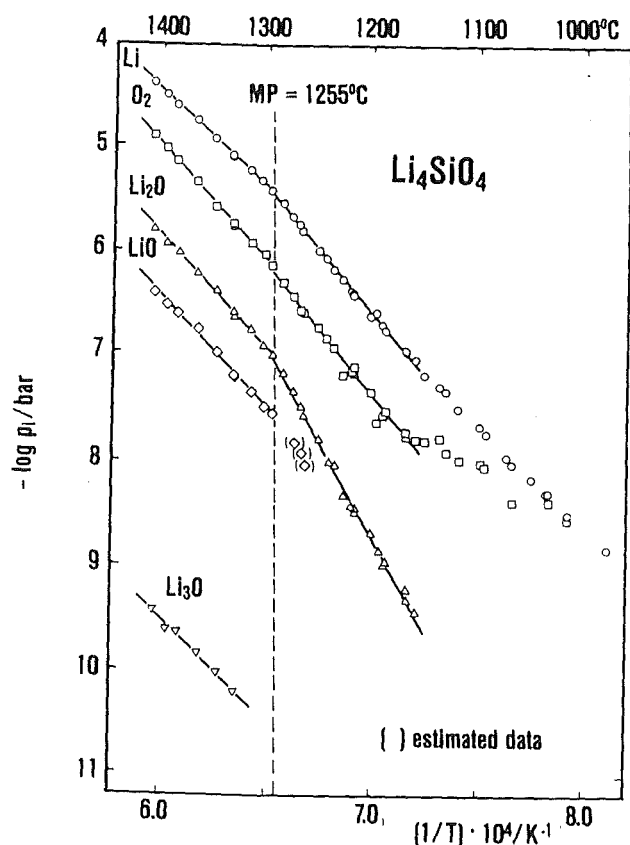


Fig. 12: Partial pressure of atoms and molecules over solid and liquid Li_4SiO_4 as a function of temperature



was calculated to be $\Delta H^\circ 298.15, r = 92.656 \text{ kJ/mol}$.

Assuming thermodynamic equilibrium and excluding effects from structural materials which reduced the oxygen activities tritium will be released from lithium orthosilicate predominantly as T_2O in the temperature range of operation of a reactor blanket. An examination of the ceramic compounds of the systems $\text{Li}_2\text{O} / \text{Al}_2\text{O}_3$, $\text{Li}_2\text{O} / \text{ZrO}_2$ and $\text{Li}_2\text{O} / \text{SiO}_2$ reveals that among the ceramics of each particular system the thermochemical stability varies in the reversed order of the lithium density, which is related to the breeding capability. Of the three systems discussed the lithium silicates show the highest thermal stability among the ceramics of comparable lithium density.

Staff:
 H.R. Ihle
 R.-D. Penzhorn
 P. Schuster
 K. Zmbov (visiting scientist)

3. Compatibility with Metallic Materials (B 14)

Li_2SiO_3 and Li_4SiO_4 are thermodynamically unstable with respect to metallic beryllium, which is of interest as neutron multiplier material in fusion reactor blankets. Therefore, chemical interactions have to be expected. To study the reaction kinetics, annealing experiments were performed in the temperature range between 600 and 900 °C with maximum annealing times of 1000 h. The experimental results for the system $\text{Be}/\text{Li}_4\text{SiO}_4$ are shown in Fig. 13. The chemical attack of the Li-silicates by Be can be divided in a uniform attack and an additional localized attack, which is very strong at temperatures ≥ 700 °C. The compatibility of Li_2SiO_3 seems to be sufficient up to 650 °C whereas that of Li_4SiO_4 is sufficient up to 700 °C.

As a result of the interaction between Be and Li-silicates, the compounds BeO , Li_xSi_y and either $\text{Li}_2\text{BeSiO}_4$ (Li_2SiO_3) or $\text{Li}_2\text{Be}_2\text{O}_3$ (Li_4SiO_4) are formed. The Li-silicides Li_xSi_y are partially liquid at higher temperatures and are the reason for the strong localized attack which amounts to 600 μm in depth for Li_2SiO_3 and 180 μm for Li_4SiO_4 (Fig. 2) after 1000 h at 750 °C. In an independent study the complicated phase relations and the possible reaction products in the system Li-Be-Si-O have been investigated.

Already at 600 °C Be interacts with stainless steel (AISI 316) as cladding material, including the formation of the compound BeNi with a Ni depletion of the steel matrix. The interaction becomes very extensive at temperatures above 700 °C. At 600 °C it occurs locally with maximum reaction depths of 25 μm . It seems that the compatibility problem in the system Be/Li-silicate/stainless steel under isothermal conditions could be governed by the Be/steel interaction.

Staff:
 O. Götzmann
 P. Hofmann
 K.-H. Kurz
 H. Metzger
 E. Nold

4. Irradiation Testing of Ceramic Breeder Materials (B 15 and B 15.3)

In assessing the performance of solid breeders, tritium release is an important aspect. KfK concentrates on lithium silicates. In addition to in-pile tests (B16), tritium release is studied in out-of-pile annealing experiments.

A large number of tests confirmed previous observations, that tritium release from our samples, especially from orthosilicate, is controlled, besides by diffusion, by several surface processes. Work is in progress to develop quantitative models to describe tritium release. Tritium release from various doped orthosilicate samples ($\text{Li}_{4-x}\text{Si}_{1-x}\text{Al}_x\text{O}_4$, $\text{Li}_{4-x}\text{Al}_x\text{SiO}_4$, $\text{Li}_{4-x}\text{Si}_{1-x}\text{P}_x\text{O}_4$, $\text{Li}_4\text{SiO}_4\text{-Li}_3\text{PO}_4$, $\text{Li}_{3+x}\text{P}_{1-x}\text{Si}_x\text{O}_4$) has

Reaction		$\Delta H^{\circ}298,r$ (kJ/mol)
solid Li_4SiO_4		
$\text{Li}_4\text{SiO}_4(\text{cr}) = 2 \text{Li}(\text{g}) + 0,5 \text{O}_2(\text{g}) + \text{Li}_2\text{SiO}_3(\text{cr})$	(1)	960.698 ± 2.38
$\text{Li}_4\text{SiO}_4(\text{cr}) = \text{Li}_2\text{O}(\text{g}) + \text{Li}_2\text{SiO}_3(\text{cr})$	(3)	520.430 ± 2.69
$\text{Li}_2\text{O}(\text{g}) = 2 \text{Li}(\text{g}) + 0,5 \text{O}_2(\text{g})$	(5)	440.228 ± 1.44
$\text{Li}_2\text{O}(\text{g}) = \text{Li}(\text{g}) + \text{Li}(\text{g})$	(6)	360.608 ± 0.84
liquid Li_4SiO_4		
$\text{Li}_4\text{SiO}_4(\text{l}) = 2 \text{Li}(\text{g}) + 0,5 \text{O}_2(\text{g}) + \text{Li}_2\text{SiO}_3(\text{l})$	(2)	946.335 ± 0.73
$\text{Li}_4\text{SiO}_4(\text{l}) = \text{Li}_2\text{O}(\text{g}) + \text{Li}_2\text{SiO}_3(\text{l})$	(4)	510.874 ± 2.51
$\text{Li}_2\text{O}(\text{g}) = 2 \text{Li}(\text{g}) + 0,5 \text{O}_2(\text{g})$	(7)	435.377 ± 2.15
$\text{Li}_2\text{O}(\text{g}) = \text{Li}(\text{g}) + \text{Li}(\text{g})$	(8)	361.909 ± 0.74

Table 4: Standard reaction enthalpy*

* Symbols taken from JANAF [8]

cr = crystalline l = liquid g = gas

The standard temperature 298.15 is given abbreviated as 298 K throughout this work.

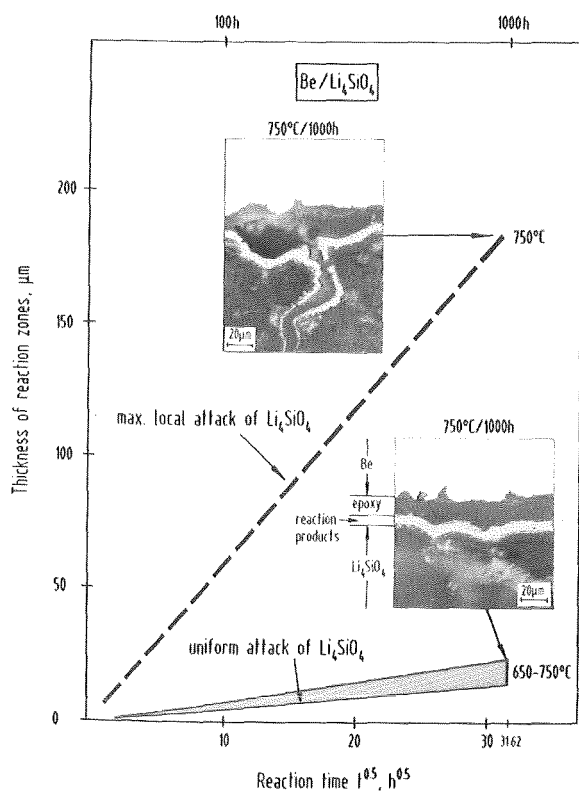


Fig. 13: Chemical interaction of Be with Li_4SiO_4 .
Penetration depth of the reaction in Li_4SiO_4 .

been studied. Tritium release from $\text{Li}_{4-3x}\text{Al}_x\text{SiO}_4$ was faster, that of the other doped samples slower than that of pure

orthosilicate. $\text{Li}_{4-3x}\text{Al}_x\text{SiO}_4$ shall therefore be tested in the next in-pile experiment (LILA/LISA).

Two metasilicate pellets from the Mol irradiation HFPIF, intended for an interlaboratory comparison of out-of-pile tritium release, have been annealed. Tritium release from the Mol pellets was remarkably faster than from KfK pellets used in LISA-1 and DELICE-01.

For all types of uncladded DELICE-01 metasilicate pellets tritium release and for sample F*6 (see Table 5), in addition, ceramographic studies have been performed. Some results are given in Table 5. Tritium retention is high at 500 °C and generally larger for the high density samples. Residence times are about two orders of magnitude larger than for orthosilicate.

The irradiation experiment DELICE 03 in the thermal flux of the OSIRIS reactor will start shortly as an international intercomparison irradiation of breeding ceramic specimens entitled COMPLIMENT (Comparison of Lithium Materials Damage Effects by Fast Neutrons and $^6\text{Li}(n,\alpha)\text{T}$ -Reactions). The experiment is scheduled for a duration of 80 full power days (FPD). The corresponding experiment in the fast neutron flux (with cadmium as the shielding material), ELIMA 2, has been under way at HFR/Petten since this April and is scheduled for a duration of 175 FPD. Consequently, both irradiation experiments will be terminated still in 1988. KfK is responsible for coordinating the COMPLIMENT activities. It is planned to perform most of the PIE work at KfK, beginning in the second half of 1989, after the irradiated 72 specimen rods have been returned.

Staff:

W. Breitung
 T. Eberle
 H. Elbel
H.E. Häfner
 K. Heckert
 J. Lebkücher
 K. Philipp
 H.-J. Ritzhaupt-Kleissl
 G. Schumacher
H. Werle

5. Tritium Recovery from Ceramic Breeder Material (B 16)

Tritium recovery from ceramic breeder material is important in assessing the performance of breeder blankets. The behaviour of lithium silicates is studied by KfK in the LISA-series of in-pile tests performed in the SILOE reactor at CEN Grenoble.

Some preliminary results from the last test (LISA-2, which was finished December 1987, have already been discussed in the last semi-annual report. Evaluation of residence times by $\tau_i = I/p$ (I inventory, p production rate) and from the slopes to the time-dependent release (τ_s) has been completed. Average sample temperatures T_{av} have been determined taking into account the temperature gradients due to internal heating, including the corrections for flux depression. Residence times are shown in Fig. 14 for sample P6 together with the fits to τ_i for the other samples and out-of-pile annealing data for 3 mm diameter orthosilicate spheres (97 %TD) of Ihle et al. Work is in progress to explain the large differences and to improve release from our samples, especially at low temperatures.

A common experiment with CEN Grenoble (LILA/LISA) is planned to start end of 1988. Samples of aluminate, doped aluminate, metazirconate (delivered by CEN) and of orthosilicate, doped orthosilicate and metazirconate (delivered by KfK) will be tested.

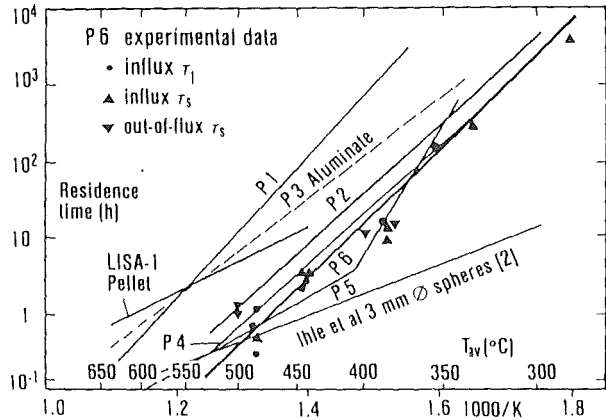


Fig. 14: Residence times for orthosilicate samples of LISA-2 P1: 0.5 mm granules, P2: 0.5 mm spheres, P4: 1.25 mm tempered spheres, P5: 8 mm dia. pellets, P6: 0.5 mm tempered spheres. For comparison data on aluminate pellets (P3) are given.

Publication

W. Breitung, M. Briec and H. Werle, Tritium Release from Lithium Silicate, Int. Symp. Fusion Nuclear Technology, Tokyo, 1988, paper B2-03

Staff:

H. Elbel
 H.E. Häfner
H. Werle

TD (%)		65		85	
Sample No.		F*6	G*1	F*4	G*4
Irrad. temp. (°C)		700	500	700	500
T-prod./pellet	P (mC)	690		800	
T-prod. rate/pellet	p (mC/h)	1.11		1.28	
Inventory/pellet	I (mC)	2.74	346	8.46	583
out-of-pile annealing He + 0.1 vol% H2				12.61	
Retention	I/P (%)	0.40	50	≈ 1.3	73
Residence time	I/p (h)	2.50	312(13d)	≈ 8.2	455(19d)

Table 5: Annealing results for lithium metasilicate, therm. fluence $6.6 \cdot 10^{19}$ 1/cm²

M 1 The Large Coil Task

The Large Coil Task was an experiment of the International Energy Agency with contributions of four nations. The goal of the experiment was to make the superconducting magnet technology available for Tokamaks. The European Community contributes to this experiment with one superconducting coil. The coil was designed, developed and constructed on behalf of Euratom by KfK-Karlsruhe together with two German companies: Vacuumschmelze, Hanau (conductor) and Siemens AG, Erlangen (coil). The test program ran since January 1986 at Oak Ridge Nat. Lab., USA. The Euratom coil passed successfully all "Standard Tests" and "Extended Tests". The whole test program was successfully completed in September 87 with outstanding results for the Euratom LCT coil.

It was agreed by all participants that the results of the experiment should be evaluated and published together. For each chapter one of the participants was the responsible editor who collected the contributions of the others. A

meeting for coordination was held in April 88 at the Paul Scherrer Institut in Villigen, Switzerland. A time schedule and exchange procedures for the completion of the report were concluded. The final edition was sent to the participants end of July 88. The report was published in the meantime. The LCT task was thereby terminated.

Publication:

D.S. Beard et al., Ed., The IEA Large Coil Task, Fusion Eng. and Design 7(1 + 2) 1-232 (1988), Special Issue

Staff:

W. Maurer

A. Ulbricht

F. Wüchner

M 3 Development of High Field Composite Conductors

Recent measurements on the influence of stresses on Nb₃Sn conductors have shown a strong effect of transverse pressure loads on the critical current I_c. As an example, a reduction of I_c of a binary Nb₃Sn wire in a magnetic field of 12T by 30% was found, when a compressive load of 70 MPa was applied.

As the NET TF conductor is designed to use Nb₃Sn filaments under a field strength of up to 12T, an assessment of the compressive stresses acting on the superconductor was felt necessary.

The procedure consisted of deriving the forces on the superconducting core from the forces in the coil which are known and calculating their transfer through the conductor conduit. According to the NET reference design radial stresses of 40 MPa and toroidal compressive stresses of 140 MPa are expected in the TF coil, the tensile hoop stresses being 140 MPa. After a first estimate of the load situation, some improvements were introduced into the design of the NET / KfK conductor concept (Fig. 15). The new conductor

MPa will increase to an average value of ~ 70 MPa due to the stress transmission between adjacent conductors. These 70 MPa will therefore act as a radial compressive stress on the superconducting core. Due to the presence of solder the stress will be distributed to act homogeneously on the Nb₃Sn wires. This is strongly different from other configurations, e.g. the cable in conduit, where the effective compressive stress at the crossover points is much higher. As mentioned above, transverse compressive stresses of the order of 70 MPa at 12 T lead, however, to a decrease of I_c by ~ 30%. In order to maintain a sufficient safety margin for the overall critical current, it is thus necessary to use Nb₃Sn wires with considerably higher critical current densities than originally thought. A detailed study is actually undertaken in our laboratory in order to decide whether the envisaged bronze route process for the production of Nb₃Sn wires should be replaced by more advanced processes yielding higher critical current densities. A detailed stress distribution calculation accompanied an integral electrical test is necessary to determine the effect of local stress enhancement and the corresponding current degradation of the superconducting core.

The present jacket design has been also improved considering the former jacket configuration, which used tack welded spacer sheets. A major manufacturer gave a bid on the fabrication of the side section by a forming process for the necessary long lengths. Figure 16 shows the section in

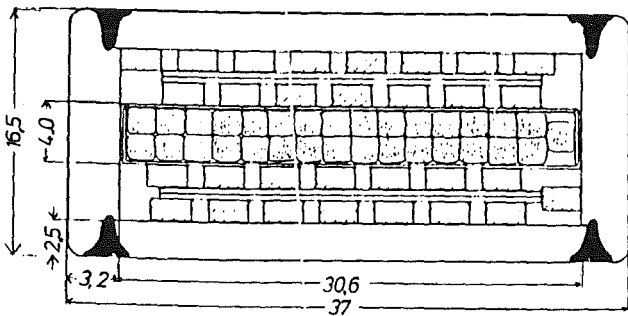


Fig. 15: Cross section of the modified NET/KfK 16 kA/12 T conductor

concept is characterized by considerably thicker steel sheets, 2.5 mm (instead of 1.5 mm) on the flat side and 3.2 mm (instead of 2.5 mm) on the narrow side. The toroidal load of each side section is calculated to be 1150 N per unit (mm) of conductor length. Taking the cover section of 37 mm length as a column, the calculated critical load is ~ 1800 N per unit (mm) of conductor length. Considering the weldments plus the winding pack stiffening effect, buckling may therefore be outruled. The side section with its 3.2 mm thickness is subjected to a deflection under the toroidal compressive stress of + 140 MPa. The maximum deflection assuming a non supported beam of 11.5 mm length is ~ 60 μm. This value will drop considerably by the mechanical support of this beam by the weldments. The deflection of the cover section is accordingly more severe due to the length of 30.6 mm. Considering the radial compressive stress of 40 MPa the deflection yields a value of ~ 1.7 mm. This means that the interior of the jacket will be subjected to considerable compressive stresses. The smaller compressive stress of 40

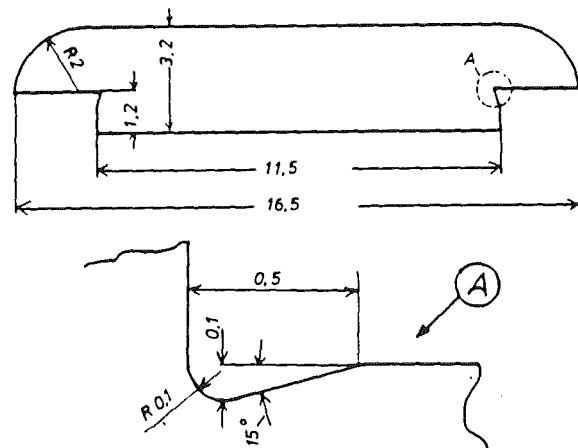


Fig. 16: Side section of the conductor jacket manufactured by continuous forming process. A) according to DIN 509.

detail. The geometrical tolerances and the evaluation of manufacturing risks for long lengths of such a section represents one major milestone before going on to a detailed final jacket design.

Design, fabrication and test of the conductor, as well as the electrical connections plus the terminations can be evaluated with subsized type conductors, actually under industrial fabrication. Also the electrodynamic behaviour (ac losses, stability) can be assessed by the measurements of the subsized conductor. The experience gained can be transferred to the full size conductor at an early stage. Each manufacturing step has to be developed separately until the

production step is under control and suitable methods of quality insurance are the state-of-the-art.

An important point in simulating the operation conditions is the measurement of I_c under axial strain. A 10 kA/100 kN strain rig for operations at 12 T has recently been tested successfully at ITP and is now available for the test of NET conductors.

The Nb₃Sn bundle conductor is still a real alternative conductor configuration for fusion reactor magnets. But a technical application of such a bundle conductor in the LCT coil of Westinghouse showed a reduced performance as compared to the design data. The mechanical properties for a safe handling and the physical properties under force load are not yet known to a sufficient extent. Thus, we continue our investigations on such conductors. After the first conductor tests (see semi annual report, May 1987), we are now improving the strain measuring technique of our one-layer coil test arrangement in the HOMER test facility. We expect more accurate results in the correlation between strain, critical current and premature initiation of normal conductivity if mechanical forces are applied in the background of a magnetic field and simultaneously flowing electrical current. An improved measuring technique will be applied to get informations in the change of the internal resistivity behaviour of Nb₃Sn conductors under mechanical force load which are necessary for calculations of electrical losses.

Staff:

W. Barth	B. Lott
M. Beckenbach	G. Nöther
M. Brünner	A. Nyilas
P. Duelli	H. Orschulko
<u>R. Flükiger</u>	H. Raber
S. Förster	T. Schneider
F. Gauland	W. Specking
W. Goldacker	S. Stumpf
A. Kling	P. Turowski
M. Klemm	

M 4 Superconducting Poloidal Field Coil Development

The aim of task M4 is to develop and test a superconducting poloidal model coil relevant for Tore Supra and NET and to simulate in the test similar load conditions. The model coil of 3 m \varnothing is under design to be operated in the KfK-TOSKA test facility in 1989. Both tasks M4 and M8 are joint efforts of KfK and CEA.

Conductor fabrication

The fabrication of the conductor can be divided in three fabrication steps:

- The fabrication of the cable and its protection tube.
- The fabrication of the conduit sections.
- The fabrication of the complete conductor (assembling of the conductor components).

In all three steps progress was obtained and useful knowledge was gained towards the manufacturing of this cable type. Subcables were fabricated and cabled around the inner tube. 4x150 m round cable were fabricated without any difficulties. The subcables were wrapped with a CuNi foil for two cable lengths. The other lengths had wrapped glass-Kapton-glass tape as insulation on the subcables. Two instrumentation wires were successfully integrated in the cabling process of the subcables for the CuNi version. The Kapton insulated wires were positioned in the outer gap between the subcables. The wires are a backup solution for quench protection if Kapton insulations between subcables and inner respectively outer tube are damaged. A removal of the Kapton insulation in the cable as discussed for the TORE SUPRA cable (M8) would make the integration of such wires in the cable indispensable. The

enclosure of the first length in the protection failed after production length of 25 m. The procedure needs further improvements in the production line and optimization of fabrication parameters. The laser beam welding experiments for the final two weld seams of the conductor conduit were continued (Fig. 17). The welding exercise on a 50 m length empty conduit and 25 m complete conductor were not satisfying. The thermal instability of the beam splitting device forced to give up this way. An attempt of a reduction of the laser beam diameter failed so that no further way for improvements were seen. Two lasers were installed in the fabrication line. After adjustment and optimization of the focussing properties of each laser beam line the quality of the weld seams were still not satisfying and partially not tight. In a tedious series of experiments a surface contamination was found out to have a strong impact on the quality of the weld seams. After carefully cleaning of the U-profiles by grinding 9 m of complete conductor were successfully welded and found to be leak tight.

Basic Investigations

An experiment for the investigations of the complete polo conductor is running. The stability limit is less than that expected from the strand stability investigations. The stability limit is still sufficient for the specified application. Verification tests are running.

A contract was placed to the High Voltage Laboratory of the University of Karlsruhe for electric field calculations of high voltage feedthroughs and a review about partial discharge measurements as a non-destructive method for material investigations.

Construction of the Model Coil

The construction of the model coil is proceeding with detailed design of the components and the preparation of the tooling for the fabrication of the model coil.

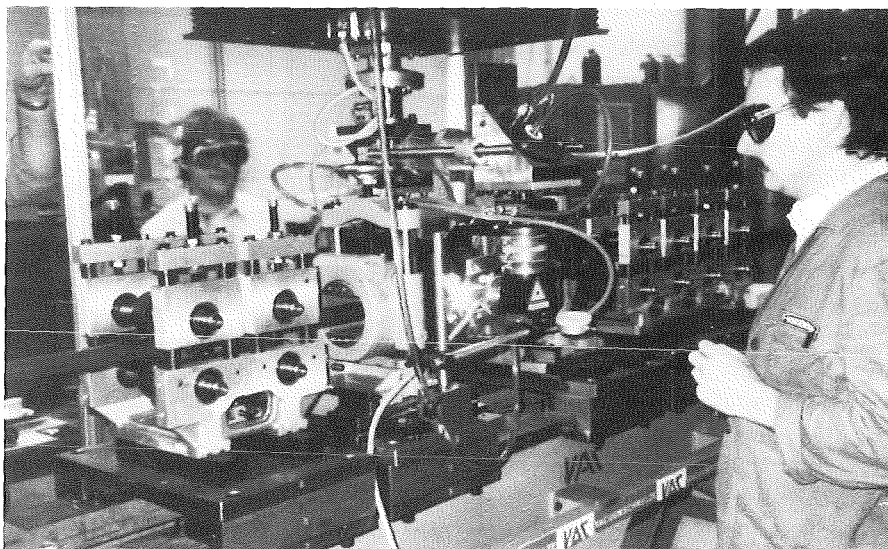


Fig. 17: Laser beam welding facility for the fabrication of the polo conductor (VAC/Heraeus Industrielasert)

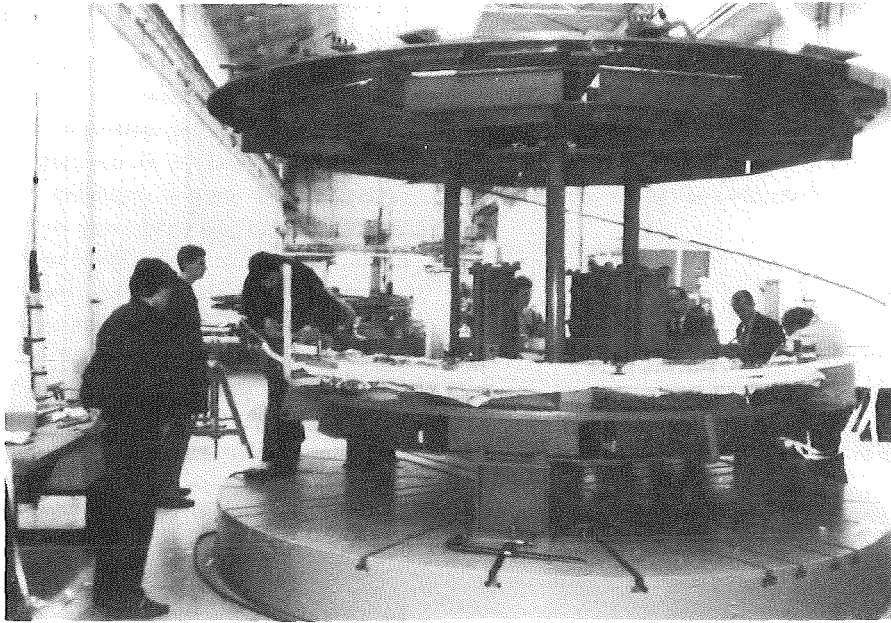


Fig. 18: The winding facility for the polo model coil (Alsthom, Belfort)

50 m conduit were delivered to the coil manufacturer and used for a winding test. The main steps of the beginning of the winding procedure and the use of the tooling were exercised (Fig. 18). Winding table and break table worked without problems. A winding tension of 1500 N was sufficient for bending of the conductor. Corrections have to be done for the insulation thickness. The compression of the layers by the winding tension reduced the insulation thickness more than expected. The bending in the transition area from the upper to the lower pancake was handled without major problems. All parts of the mould for impregnation are on site. They will be assembled for the leak test of the mould.

For all components (conductor terminals, connections, midpoint connection, short circuit ring) detailed designs are ready for the construction of prototypes. The Phase I report which contained the final design of the polo model coil was submitted to KfK by Alsthom .

Basic components like axial and radial insulation breaks were already tested. Two axial insulation breaks, one developed by KfK and one by Alsthom passed successfully all low temperature and pressure cycles with helium leak rates of less than $3.6 \cdot 10^{-8}$ mbarl/s. A radial insulation break developed by KfK was successfully tested in a specially designed facility (Fig. 19). Temperature cycles down to helium temperature, pressure cycles up to 25 bar and a high voltage loading up to 23 kV were performed in this test facility. The helium leak rate after this test series was less than $2 \cdot 10^{-8}$ mbarl/s. The observed beginning of partial discharges started at 4.2 K at considerable higher voltages (Fig. 20). This demonstrated an increase of the dielectric strength at 4.2 K. The insulation break tested was

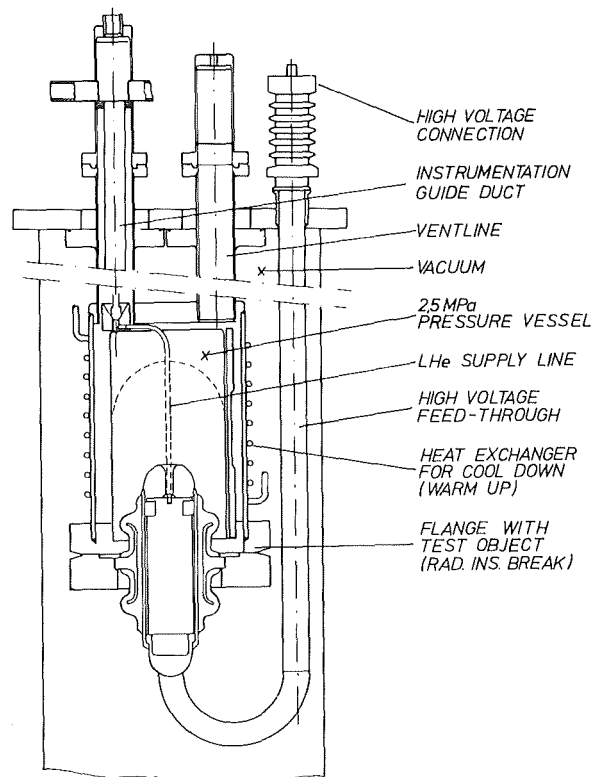


Fig 19: The radial insulation break installed in its test arrangement which is suitable for a loading by pressure, thermal and high voltage cycles.

manufactured in a filament winding technique with resin wetted filaments. Another radial insulation break was manufactured in the same technique but vacuum impreg-

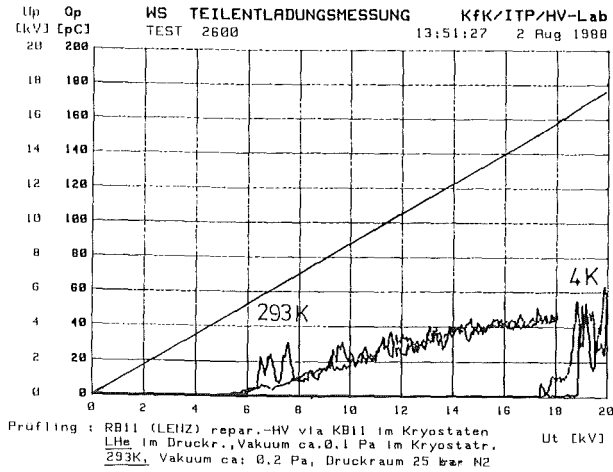


Fig. 20: Starting point for partial discharges at room temperature and at 4.2 K.

nated with resin. During installation work a crack occurred between the inner electrode and reinforced epoxy resin. This crack was also indicated by a lowering of the voltage level of the beginning of the partial discharges. Both results indicated that the dielectrical conditions of electrical components were correlated to the beginning of partial discharges.

The linearity of inductive displacement transducers was investigated at 4 K.

Modification of the TOSKA Facility

The 30 kA power switch system was brought successfully through the preliminary acceptance test. All operation modes (safety discharge, high voltage discharge, high voltage pulse operation, partial coil discharge) were tested with a copper coil up to 10 kA current and 23 kV (Fig. 21).

The piping of the TOSKA vacuum vessel is being prepared for the test of the Polo model coil. The installation of the cryogenic measuring and control technique is in progress. A pretest of all components of the cryogenic system is scheduled before the installation of the Polo model coil. In this test the Polo model coil will be simulated by the loop used for the 2 phase flow investigations.

Considerable effort was put in the design of a vapour cooled lead for 22 kA and 23 kV rated values. For the heat exchanger part a computer code was developed. It was verified by experimentally measured values obtained by a test of a vapour cooled lead developed for TORE SUPRA by CEN Grenoble tested 8 months before. The test results supported the finding of a suitable description for the heat transfer mechanism. It is the intention to use a bypass of supercritical helium flow for the cooling of the cold end of the vapour cooled lead. This is more relevant for forced flow cooled superconducting coils than the use of a helium bath. The optimization of the parameters is in progress.

CIRCUIT DIAGRAM OF THE POLO ELECTRIC POWER NETWORK

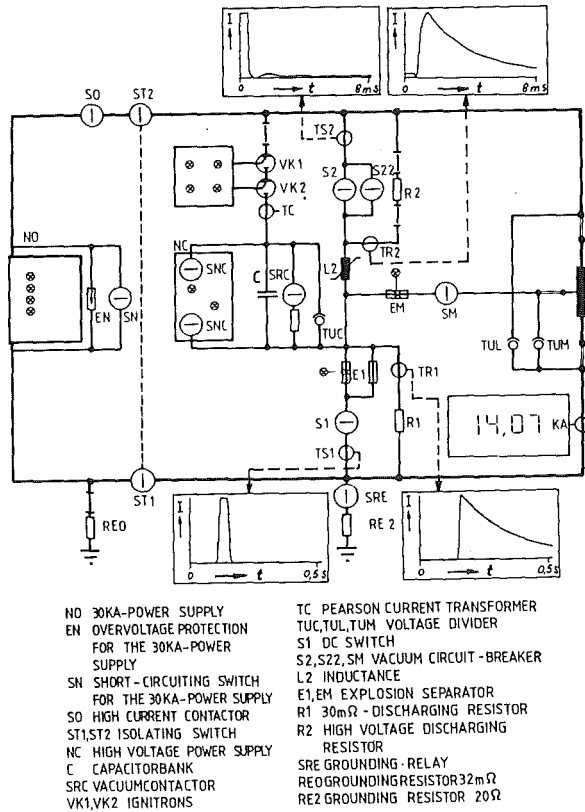


Fig. 21: Circuit diagram of the installed power switch circuit for the test of the Polo model coil.

Publication:

U. Jeske et al: Fabrication of a 15 kA NbTi Cable for the 150 T/s High Ramp Rate POLO Model Coil, 15th SOFT, Sept. 1988, Utrecht

Staff:

- | | |
|-----------------|----------------|
| H. Bayer | L. Schappals |
| I. Donner | G. Schenk |
| P. Duelli | C. Schmidt |
| S. Förster | K. Schweickert |
| P. Gruber | E. Specht |
| T. Hardy | H.-J. Spiegel |
| W. Heep | J. Seibert |
| <u>U. Jeske</u> | F. Süß |
| G. Nöther | M. Süßer |
| A. Nyilas | G. Tadeishi |
| M. Oehmann | A. Ulbricht |
| U. Padligur | D. Weigert |
| R. Rietzschel | F. Wüchner |
| | V. Zwecker |

**M 8 Design and Construction of a
Poloidal Field Coil for TORE SUPRA
as NET-Prototype Coil**

The objective of the task is the development and test of an Equilibrium Field Coil (EF Coil) with parameters relevant for NET. The reliable operation of a superconducting PF-coil shall be demonstrated in a real tokamak environment with the rapid field variations due to start up, plasma position control and disruptions. The development has to confirm the coil construction process proposed for NET on a fairly large scale

For this purpose, the upper ring coil "E_h" of TORE SUPRA will be replaced by a superconducting coil "EHS" Design and

construction will be based on the results of the already running task M 4.

The task of the design and construction of the TORE SUPRA coil was transferred to CEA Cadarache in joint agreement. KfK will assist with its experience in the development and test of the polo model coil. It will contribute to the high voltage components and to conductor related questions.

Staff:

S. Förster

U. Jeske

G. Schenk

C. Schmidt

M 9 Structural Materials Fatigue Characterization at 4 K

For the 4 K mechanical characterization (fracture toughness, fatigue and tensile strength) of the bulk and weld metal a variety of specimens are required. Especially for the latter one the specimen positioning in the weldment need to be carried out in a strict order to receive a maximum of information for the mechanical performance of the joints under test.

Details of the weld procedure

The TIG welding program which had the objective to join the 30 mm thick austenitic stainless steel plates (1.4429, 1.4435 and 1.4306) was performed by SLV-Duisburg. The starting point of this program was the preliminary qualification of the weldments according to their hot cracking susceptibility and their 77 K Charpy V-notch measurements. Current commercially available welding wires were tested during the course of weld metal qualification. Ten different welding wires were supplied by five vendors. Figure 22 shows the weld wire chemistry and the heat number.

Bez.	Herkt.-Hr.	Charge	C	Si	Mn	P	S	Cr	Ni	Mo	N
B 1	1.4316	500697	0,012	0,96	1,09	0,023	0,012	19,70	10,65	-	-
B 2	1.4453	500836	0,022	0,67	7,20	0,014	0,007	18,85	16,78	4,26	0,14
B 3	1.4430	501234	0,02	0,82	1,19	0,022	0,004	18,45	11,88	2,54	-
K 1	1.3954	258431	0,018	0,72	7,79	0,012	0,008	21,5	18,40	3,60	0,21
K 2	1.4455	253539	0,010	0,35	7,09	0,016	0,005	19,70	15,5	2,77	0,19
H 1	1.4455	531801	0,010	0,35	7,08	0,016	0,005	19,70	15,56	2,77	0,199
S 1	1.4465Hn	760633	0,018	0,17	4,36	0,013	0,011	24,70	21,52	2,02	0,13
T 1	1.4440	28784	0,011	0,28	3,31	0,015	0,005	18,55	17,36	4,26	-
T 2	1.4440	28838	0,014	0,28	2,63	0,017	0,003	18,40	17,21	4,20	-
T 3	1.4455	27618	0,016	0,54	7,38	0,018	0,007	20,32	15,21	2,91	0,16

Fig. 22: Welding wire chemistry of the supplied ten different heats. The codes B, K, M, S and T refer to various vendors whereas the figures behind it to different materials.

Only three codes (K2, M1 and S1) showed reasonably impact characteristics at 77 K (Fig. 23).

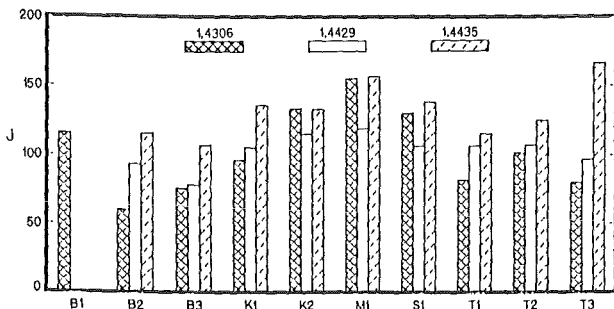


Fig. 23: 77 K-Charpy V-notch results of the tested weldments.

All other welding wires were outruled. Each plate material was welded with the above given three codes, thus supplying three sets of butt joints of ~ 1000 mm length. The

welding parameters were as following: a welding speed of 0.14 m/min at 14 V and 200 A, and a wire diameter of 3.2 mm. Weld wire distance from the weld head was approximately 15 - 18 mm. The already delivered welded plates were mechanically prepared to position the different specimens. The etched weld profiles of each plate could indicate the weld seam center. Standard 5 mm Ø tensile specimens were positioned in the top and bottom weld position, thus giving specimens of pure weld metal (Fig. 24).

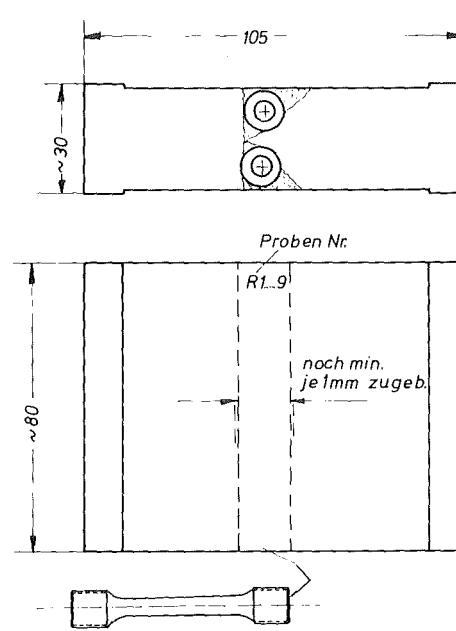


Fig. 24: Location of tensile specimen in the weld zone.

Figure 25 shows the specimen allocation in weld transverse orientation. These specimens will supply additional 4 K data of HAZ tensile performance. For fracture and fatigue measurements compact tension (CT) type of specimens will be machined. In this case the notch position will be placed in the weldments and at the boundary of weld/bulk material (HAZ).

The fatigue CT-specimens have a thickness of 6 mm, whereas the fracture specimens have a thickness of 15 mm. Figure 26 shows the details of the specimen allocation in the welded material. Altogether 72 fatigue and 72 fracture toughness specimens will be machined. Starting of these tests is planned early in 1989.

Cryogenic test facility

The installation of the flow cryostat with integrated pulling rods of 50 KN capacity is completed. The delivered 25 KN servohydraulic unit (MTS) has been already adapted on the load frame. First screening tests at ambient could be successfully carried out under load and displacement control, respectively. Figure 27 shows a photograph of the entire device in its early stage. The adaption of the cryostat to the servohydraulic unit will be completed within the next months.

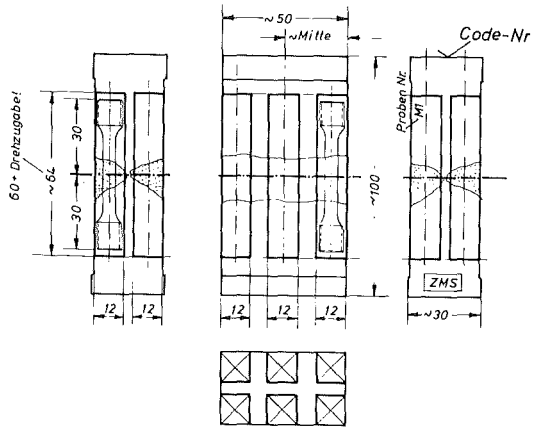


Fig. 25: Location of tensile specimen transverse to welding direction.

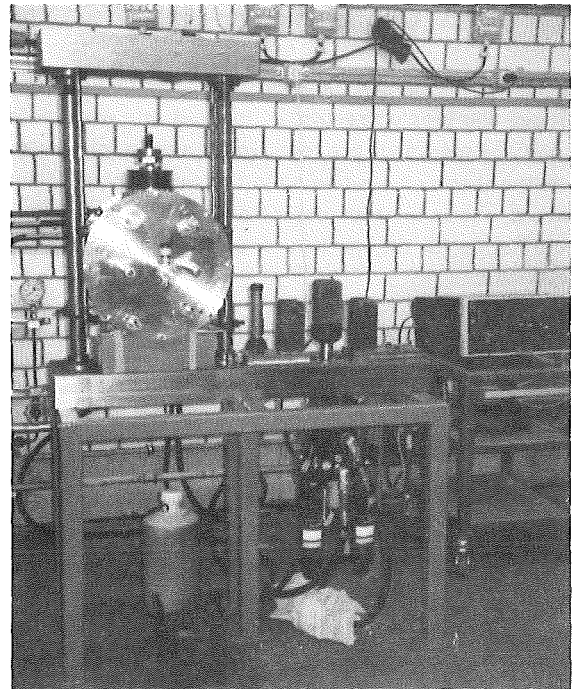


Fig. 27: Flow cryostat positioned in the load frame and the servohydraulic unit with its electronic controller which includes the microprocessor driven wave profile generator.

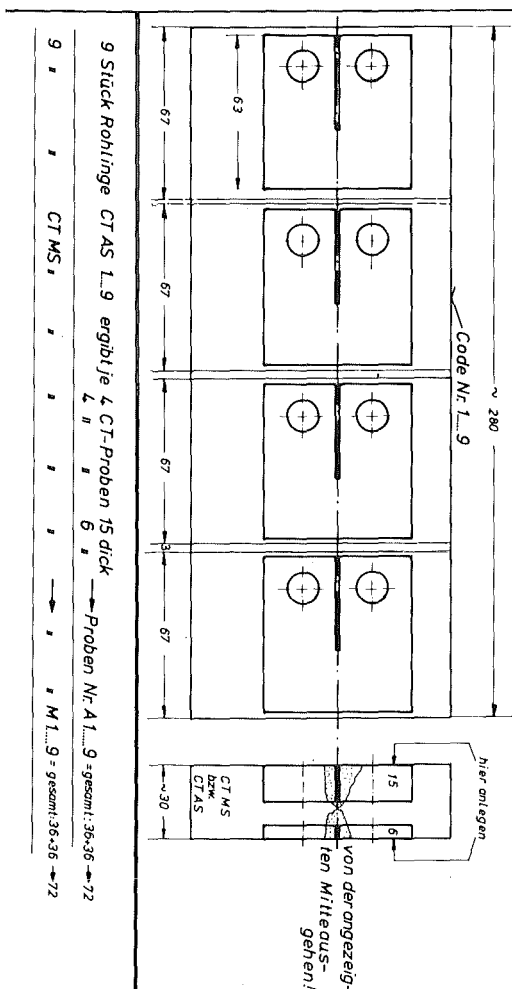


Fig. 26: Fatigue and fracture toughness specimens with the notch allocation in the weld metal and at the oundary of bulk/weld.

Staff:
 S. Fischer
 A. Nyilas
 H.P. Raber

M 12 Low Electrical Conductivity Structures Development

Polymers and polymeric fibre composites are applied in fusion technology as insulation- and structural materials. Electrical insulation has to be provided in magnet coils. Insulating structural materials in the vicinity of pulsed magnets are capable of avoiding eddy currents and thus expensive helium cooling. The selection of polymeric materials in fusion technology is restricted to those with a high resistance to radioactive irradiation. The classes of polyimides (PI) tolerate the highest radiation doses, up to 10^8 Gray, without deterioration of mechanical properties by more than 25%. Polyetherimide (PEI), polyetherketone (PEEK) and aromatic amine epoxies are at a similar level of resistance. The degradation is most serious for mechanical properties and less critical for thermal and electrical parameters.

Fibre glass composites are applied as very high resistivity insulation materials. Carbon fibre composites show some conductivity, but it is lower by a factor of roughly 30 compared to steel at 4.2K. This is sufficient for suppressing eddy currents in structural elements.

Support structures for pulsed magnets should have a high mechanical fatigue endurance limit. This can be achieved by carbon fibre composites. Problems arise from fibre-matrix bonding and fabrication techniques. Many thermoplastic polymers show a low fibre-matrix bond which is reflected in a low interlaminar shear strength. It is a positive feature that composites with PI and PEEK exhibit a very high interlaminar shear strength (see Fig. 28). PEI seems to be less favourable

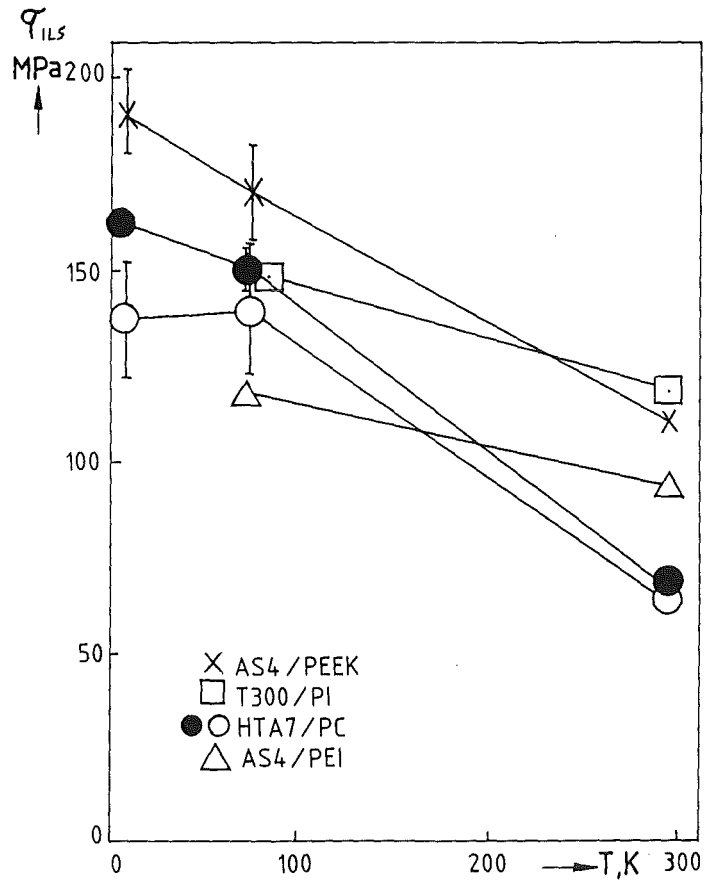


Fig 28: Interlaminar shear strength of thermoplastic carbon fibre composites

It had been expected that the fatigue endurance limit for PEEK-carbon fibre composites were similar to those with an epoxy matrix, namely 85% of the static strength. This was not confirmed in experiments despite the excellent bonding conditions of PEEK. As shown in Fig. 29, PEEK-carbon fibre composites degrade by 50% after 10^7 load cycles. The explanation was furnished by micrographs which exhibited wave shaped fibre arrangement and crack initiation localized to it. Fibre disarrangement arises because of the high viscosity of PEEK during the fabrication stages. It is assumed that improved production techniques will yield a strong increase in the fatigue endurance limit. New

methods, now under test, are hybrid techniques under which thin matrix and fibre filaments are spun to a yarn. This effects a much tighter fibre-matrix connection during the heat and pressure treatment in the production process. A better homogeneity of fibre arrangement will be achieved and possibility is opened up of pressing larger and more complex structural elements without fibre disarrangement.

Staff:
K. Ahlborn
G. Hartwig
S. Knaak

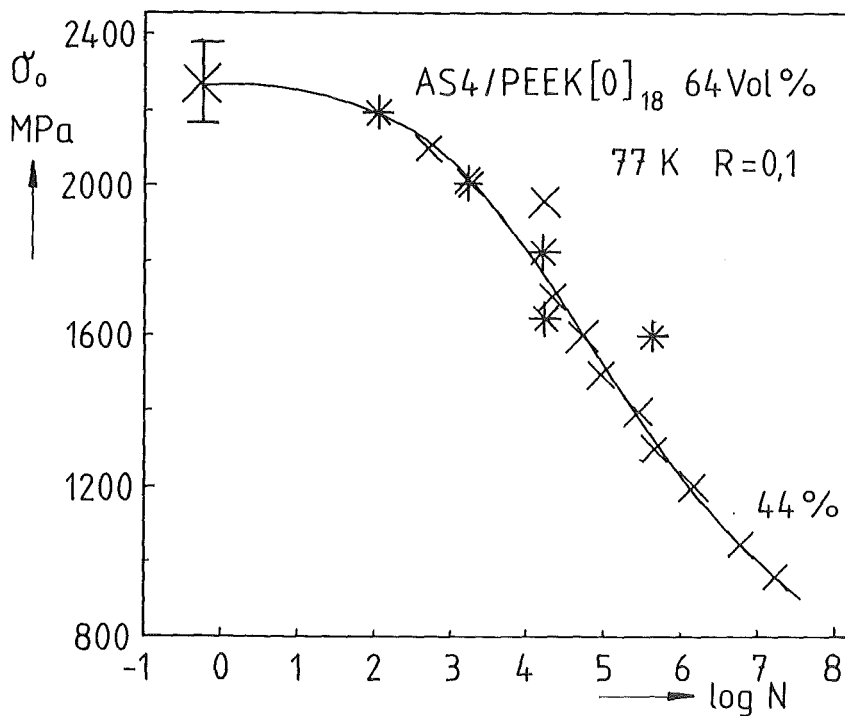


Fig. 29: Fatigue behaviour of an unidirectional carbon fibre-PEEK composite

MAT 1.6 Development and Qualification of MANET 1

In addition to the cyclic loading conditions of the normal operation of tokamaks, some components may be subjected also to off-normal loads whose loading rate can be three or more orders of magnitude higher. Examples of dynamic loadings are disruption loadings, pressure waves, seismic loads and impact loads during handling [1].

The material response to such loadings can be simulated in Charpy V-notch impact tests. One of the most important results of such tests is the ductile-brittle-transition-temperature (DBTT). This temperature is dependent on irradiation conditions and the specimen size. The size of standardized Charpy V-notch specimens (10x10x55 mm) is too large for irradiation in fast flux reactors. Therefore it is necessary to calculate the DBTT of irradiated large specimens from data of irradiated small specimens. Louden et al. [2] have proposed such a calculation:

$$(T/\sigma')_{L,I} - (T/\sigma')_{L,U} = (T/\sigma')_{S,I} - (T/\sigma')_{S,U}$$

T - transition temperature; σ' - maximum normal elastic stress at the notch root; L - large specimens; S - small specimens; I-irradiated; U - unirradiated.

$$\sigma' = K_t \cdot 3 P_m \cdot L (2B(W-A))^2$$

L,B,W and A are the span, thickness, width and notch depth, respectively; K_t is the stress concentration factor; P_m is the maximum load with general yielding. The value of K_t is dependent on some specimen dimensions and on the grain size of the material and can be calculated after Neuber [3]. P_m has to be measured in instrumented impact tests or can be calculated after Lucas et al. [4], [5]:

$$P_m = \sigma_f^* \cdot B(W-A)/6.25$$

with $\sigma_f^* = 2400$ MPa.

In order to verify this hypothesis some experiments have been planned on specimens with different sizes and material conditions.

In the frame of the qualification of the MANET 1 material 1.4914, Chg. 53645, instrumented notch impact bending tests have been carried out with unirradiated Charpy V-notch specimens (10x10x55 mm). The results are shown in Fig. 30, where the Charpy V impact energy and the crystalline area are represented as a function of the test temperature. The transition temperature is 25°C, a normal value for such materials. The microstructure and the fracture surfaces were examined in a Scanning Electron Microscope

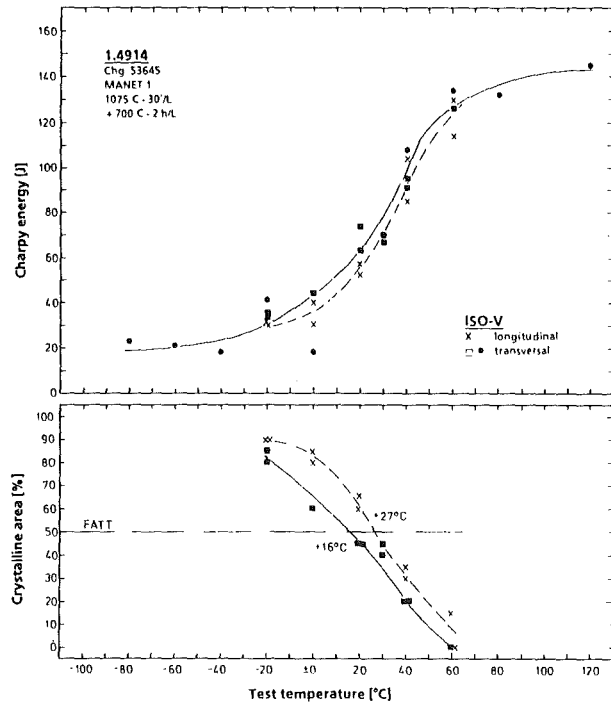


Fig. 30: Charpy V-notch properties

Staff:

- B. Dafferner
- H. Kempe
- E. Materna-Morris
- W. Meyer
- L. Schäfer
- C. Wassilew

References:

1. Anderko, K., Zolti, E. Journ Nucl. Mat. 155-157 (1988)
2. Louden, B.S. et al.: Journ. Nucl. Mat. 155-157 (1988)
3. Neuber, H.: Kerbspannungslehre, Springer (1958)
4. Lucas, G.R., et al.: Fusion Techn. 10 (1986), p. 728
5. Lucas, G.R., et al.: ASTM-STP 888 (1986), p. 305

MAT 1.9 Pre- and Post-Irradiation Fatigue Properties of 1.4914 Martensitic Steel

Thermal cycling of large components is a serious problem for the designer. The structure considered in the present case is the first wall of a fusion reactor. Its surface, in the present design concept, will be subjected to radiation heating from the plasma facing side which may lead to severe thermal stresses. Due to the discontinuous operational mode thermal cycling will generate oscillating temperature gradients. These, depending on the loading conditions, will cause elastic or elasto-plastic reversed deformation giving rise to thermal fatigue which at present is considered as the most detrimental lifetime phenomenon for the structure considered. The investigations of MAT 1.9 are devoted to this problem.

The studies to be reported within MAT 1.9 are:

- Isothermal fatigue on MANET 1 and W.Nr. 1.4909 at 450°C and 550°C
- Extensometry and thermal expansion compensator during thermal cycling experiments
- First results in thermal fatigue of AISI 316L and microstructural observations
- Measurement of static and dynamic temperature distribution on H-GRIM samples from MANET 1 (W.Nr. 1.4914)

1. Isothermal Fatigue

In order to study the influence of strain amplitude and temperature upon the number of cycles to failure N_f , a test program for MANET 1 is on the way. This is conducted on solid GRIM specimens (S-GRIM). The results for the test temperature 550°C are shown in Fig. 31. Because at present no S-GRIM data are available for AISI 316L NET-material, for comparison the results from the austenitic steel type W.Nr.1.4909 (Krupp-heat) are shown in Fig. 31 as well. The chemical composition of this material is very similar to that of AISI 316L NET (Ispra-heat). For $\Delta\epsilon_t \geq 0.6$ the results for both the materials are the same; however for $\Delta\epsilon_t = 0.4$ the N_f -value for MANET1 is by a factor of 3 larger than that for W.Nr. 1.4909. The results for $T = 450^\circ\text{C}$ are shown in Fig. 32. As follows from Fig. 33, in contrast to the steel W Nr. 1.4909, for which higher N_f -values result for $T = 450^\circ\text{C}$, the N_f -data for MANET1 are essentially the same for both temperatures. Continuous cycling tests at 250°C for $\Delta\epsilon_t \geq 0.4\%$ have been finished, those with $\Delta\epsilon_t \leq 0.4\%$ are still running.

Examinations of the influence of the mean strain upon N_f conducted on MANET 1 S-GRIM specimens for the temperature $T = 450^\circ\text{C}$ and 650°C resp have been completed. The results will be reported in the next semi-annual report.

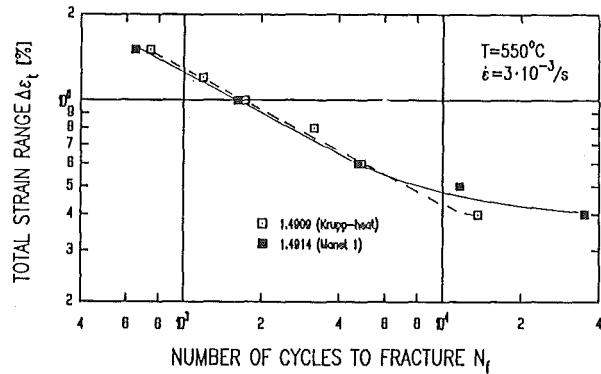


Fig. 31: Total strain range vs. number of cycles to fracture for MANET 1 and W.Nr. 1.4909 (T = 550°C) S-GRIM

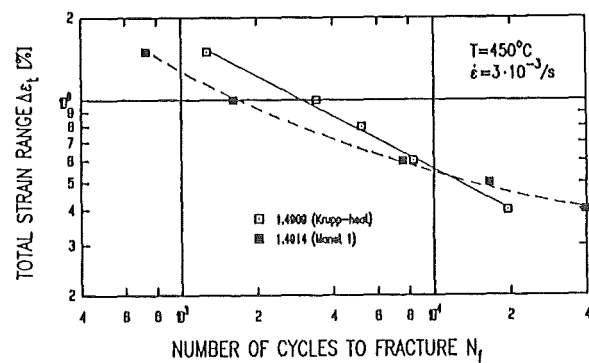


Fig. 32: Total strain range vs. number of cycles to fracture for MANET 1 and W.Nr. 1.4909 (T = 450°C)

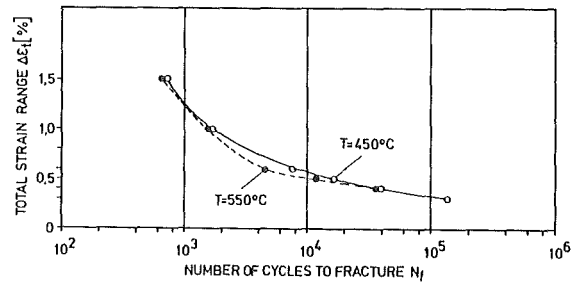


Fig. 33: Total strain range vs. number of cycles to fracture for MANET 1 at 550 and 450°C

2. Temperature cycling experiments

2.1 Extensometry and thermal expansion compensator

As compared to isothermal low-cycle-fatigue-tests, thermo-mechanical cycling experiments are evidently the more complicated ones. This is because in the latter procedure the specimen creates the loads by interaction with its surrounding. These for an imposed temperature field depend on the experimental boundary conditions. The total strain ϵ_{net} - which is the resulting output quantity - has two contributions, namely

$$\epsilon_{net} = \epsilon_{mech} + \epsilon_{thc} \quad (1)$$

where ϵ_{mech} , ϵ_{thc} is the mechanical and thermal strain component, resp. Provided that the time dependent temperature field along the specimen is known, principally ϵ_{thc} can be calculated. Moreover this can be measured in separate experiments. In difference to the measurement of displacement along a reference length, temperature data are local values. Therefore temperature gradients during cycling - which moreover are different in the heating and cooling phase. - lead to a "shift" between the displacement and temperature data giving rise to a hysteresis loop. This effect imposes difficulties in separating the strain contributions involved. The hysteresis can be reduced by decreasing the reference length.

In the present investigation an Instron axial extensometer of a reference length 8 mm was used. This was insulated from the specimen electrically as well as thermally. The attachment to the specimen, as shown in Fig. 34, is done by springs.

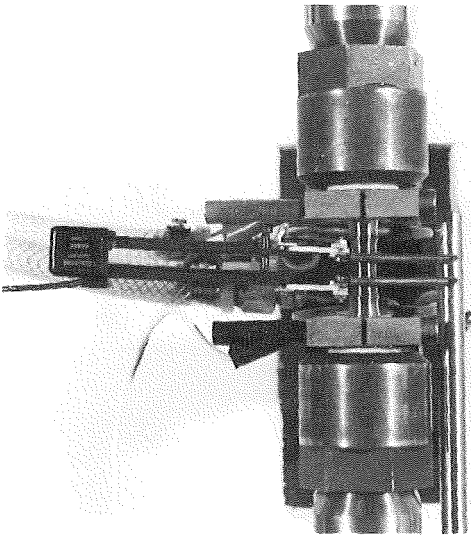


Fig. 34: Application of the extensometer with a gauge length of 8mm on the H-GRIM specimen

The mechanical strain ϵ_{mech} was determined by means of a simple electrical circuit TEC (thermal expansion compensator). This was calibrated under load free conditions, where $\epsilon_{net} = \epsilon_{thc}$. Then the actual ϵ_{thc} -values during cycling are obtained from the current readings of displacement and temperature data by means of the calibrated value ϵ_{thc} . The ϵ_{mech} values follow then from eq. (1).

2.2 First results in thermal fatigue of AISI 316 L

It was the aim of the preliminary experiments to check the measuring system attached to the Instron machine. The test conditions were such to allow comparison with scarce data from literature (AISI 304). The temperature/time loading profile was saw-tooth like with $T_{max} = 550^{\circ}C$, $T_{min} = 200^{\circ}C$ and a frequency of 0.5 cpm ($8.3 \times 10^{-3}/sec$) which was equal

for the heating and cooling phase, resp. The corresponding rate was $5.83^{\circ}C/sec$. The specimen was clamped in the cooling phase at $T = 375^{\circ}C$ and accordingly the first cycle occurred in tension.

The deformation is controlled by the total strain amplitude $\Delta\epsilon_{net}$ and therefore the stress range $\Delta\sigma$ as well as $\Delta\epsilon_{mech}$ vary during the test. For the above loading conditions several data for cyclic steady state behaviour are listed below.

Because the testing device can not control the mechanical strain range $\Delta\epsilon_{mech}$, both the stress range $\Delta\sigma$ and $\Delta\epsilon_{mech}$ change with the number of cycles. The mechanical parameters during the stabilized hysteresis loops were:

$$\begin{aligned} \Delta\epsilon_{mech} &= 0,42 \% \\ \Delta\epsilon_{pl} &= \Delta\epsilon_{mech} - \Delta\epsilon_{el} = 0,1 \% \\ \Delta\sigma &= 576 \text{ MPa} \\ \sigma \text{ at } T_{min} &= 306 \text{ MPa} \\ \sigma \text{ at } T_{max} &= -270 \text{ MPa} \\ N_f &= 8637 \text{ cycles} \end{aligned}$$

In Fig. 35 results from thermo-mechanical cycling experiments conducted on AISI 304 [1], [2] are shown together with the first own result on AISI 316 L in the $\Delta\epsilon_{mech}$ vers. N_f diagram.

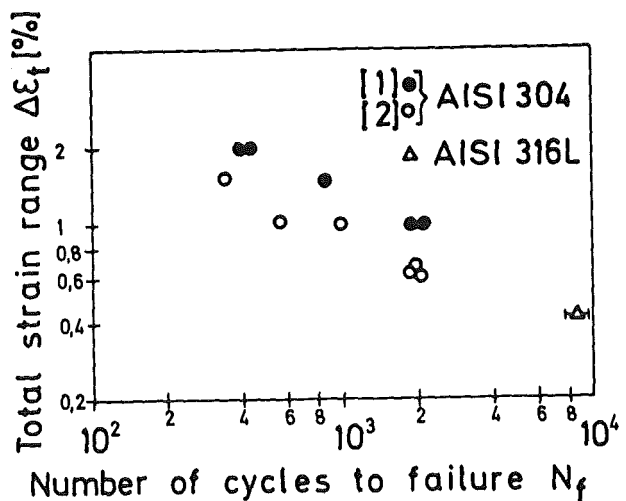


Fig. 35: $\Delta\epsilon_t (\cong \Delta\epsilon_{mech})$ vs. N_f diagram
 [1] Kuwabara, K. and Nitta, A., ASME-MPC Symposium on Creep-Fatigue Interaction, 1976, pp. 161-177
 [2] Taira, S. and Fujimo, M., Trans. ISIJ, Vol 19, 1979, pp.185-190

2.3 Microstructural observations

Electron scanning microscopy was used to examine the cracks developed during thermo-mechanical cycling. Fig. 36 shows a view perpendicular to the fracture surface of the main crack. Typically striation markings are observed. Their spacings correspond to a crack growth rate of stage II of the

growth rate vers. ΔK_c diagram. In average the direction of the striations is perpendicular to specimen's radius and parallel to the crack front

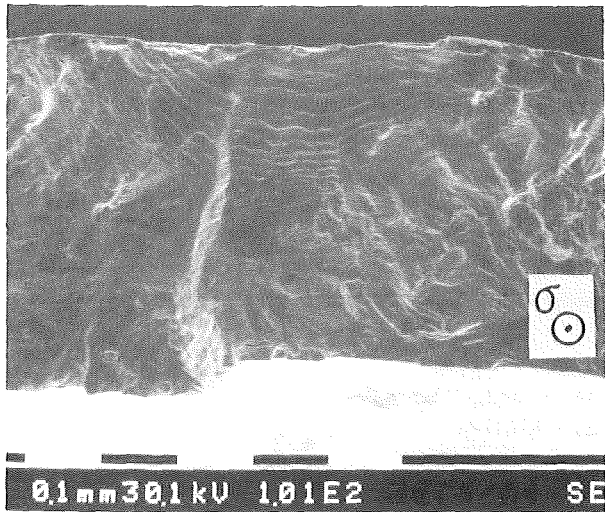


Fig. 36: Typical fracture surface of a thermally cycled H-GRIM specimen under the above mentioned conditions

2.4 Temperature distribution in MANET 1

In order to examine the axial temperature distribution of the specimens in the test rig, H-Grim specimens from MANET 1 (W.Nr. 1.4914) were provided with 7 thin Ni-CrNi thermocouples. Some of them will be heated stationary to get the temperature distribution for temperatures in the range between 500 and 50°C. The other specimens will be heated cyclically at a constant $\Delta T = 300^\circ\text{C}$ at different heating (= cooling) rates between 1 and 10K/s. The results of measurements will be compared with calculations.

Staff:

W. Baumgärtner
M. Bocek
C. Petersen
D. Rodrian
W. Scheibe
R. Schmitt
H. Schneider
W. Schweiger

**MAT 1.11 Post-Irradiation Fracture
Toughness of Type 1.4914
Martensitic Steel**

The superiority of the 12% Cr class of alloys with regard to the helium embrittlement and void swelling was the reason to consider these as an alternative to 316 SS for use as first wall material for NET. The studies carried out in KfK in attempt to improve the performance of the 12% Cr alloy 1.4914 for nuclear applications have led to optimisation of the chemical composition and of the microstructure of the steel. However, first experiments on various development heats of 1.4914 steel irradiated in BR2 at temperatures between 150 and 370°C have shown that the impact properties have been significantly impaired. The influence

of neutron irradiation led to an increase in DBTT and a decrease of the upper shelf energy.

In order to investigate the influence of fast neutron irradiation on the impact behaviour of the optimised MANET-1 heat, the experiment SIENA carried out in HFR Petten had been started in december 1987. The irradiation of the specimens with a dose level equal to ≈ 5 dpa has been completed so that in 1989 first impact experiments probably could be carried out. The irradiation will be continued with replacement of specimens for intermediate dose levels up to an accumulated target dose of approximately 35 dpa.

Staff:

B. Dafferner

E. Materna-Morris

C. Wassilew

MAT 2.2 In-Pile Creep-Fatigue Testing of Type 316 and 1.4914 Steels

Pressurized tubes loaded with variable inner pressure will be irradiated in the central core position of KNK II to study the in-reactor deformation behaviour of the martensitic steel 1.4914 (MANET 1) and the austenitic reference alloy AISI 316 L under stress conditions typical for the First Wall in Tokamak devices. For the first irradiation, denominated LOADCYCLE 1.36-5, eight pressurized capsules made of 1.4914 material are under preparation.

Beside the pressure variation each capsule is provided with an Ohmic heater which allows to hold it at a constant but variable temperature level. Even thermocycling is possible within a given temperature range. Measurement and control of temperature for each capsule is provided by three thermocouples which are welded by resistance weldment at the outside of the pressurized capsules and fixed in addition by welded bonds.

In this reporting period a possible influence of the thermocouple weldments on the integrity and the

mechanical properties of the test capsules was investigated. Several tube specimens partially provided with thermocouple weldings were fabricated, tempered at 700°C/2 h and then creep-tested at 560°C at inner pressure levels between 265 and 445 bar. Fig. 37 shows that no influence of the weldments on the creep rupture properties exists. Also the thermocouples worked perfectly. This leads to the conclusion that the adapted weldment technique of thermocouples formerly developed for austenitic alloys is adequate for martensitic material, too.

In a second series of experiments the influence of thermal cycling performed between 200 and 600°C on the endurance of the bonded thermocouples was tested. The failure test was finished after about 6000 cycles with only one thermocouple failing obviously due to an uncorrect weldment. The tests will be continued with other parameters.

Staff:

K. Ehrlich

H. Lehning

G. Reimann

L. Schmidt

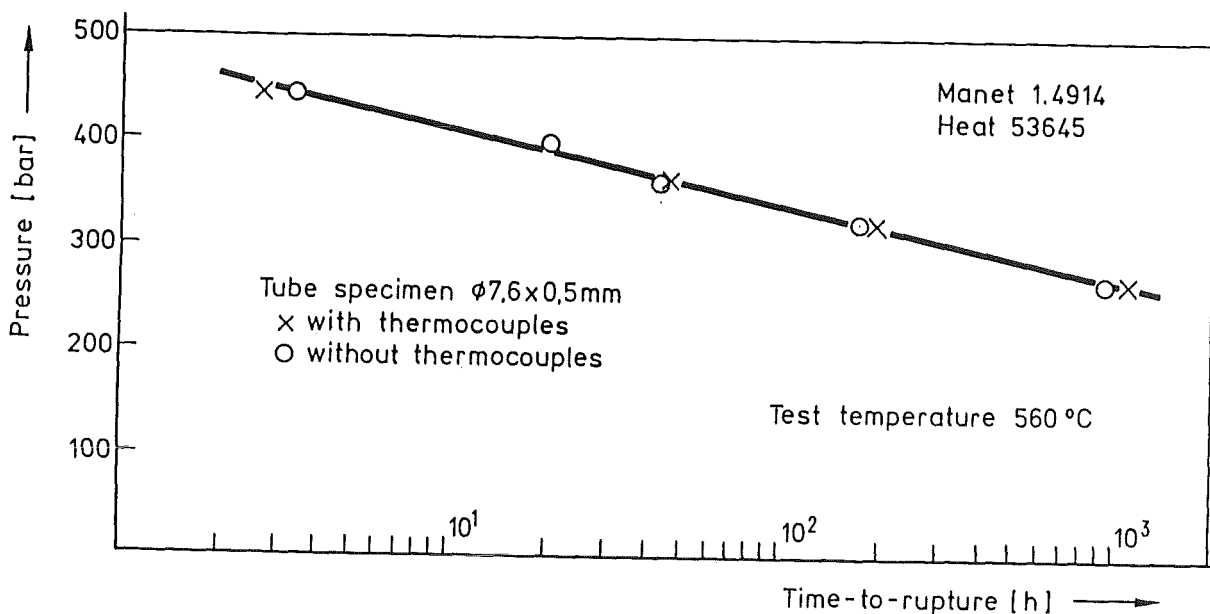


Fig. 37: Time-to-rupture of pressurized tube specimen without and with thermocouples.

MAT 6/MAT 13 Ceramics for First Wall Protection and for RF Windows

SiC qualities of industrial manufacturers are to be tested concerning the durability of tiles to protect the first wall against plasma instabilities and disruptions. Insulator materials (like Al_2O_3 , $MgAl_2O_4$, AlN) are to be selected with regard to their resistance to thermal crack formation by dielectric loss in RF-windows. These windows shall be applied to separate wave guides for ECR heating from the plasma vacuum.

The measurements of thermophysical properties on SiC are finished. Fig. 38 shows the thermal conductivity of different SiC-qualities. "SiC" with the best thermal conductivity over the whole temperature range was a comparatively coarse-grained, dense material which had probably been produced by a special hot-pressing process.

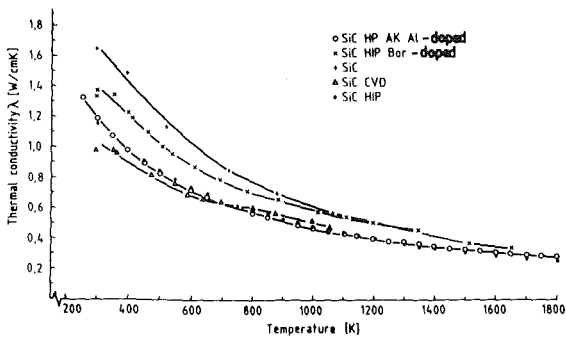


Fig. 38: Thermal conductivity of SiC of different origin.

Measurements on insulator materials were performed in the following way:

1. Specific heat of $MgAl_2O_4$ spinel (Fig. 39)
2. Specific heat of $Al_2O_3 + ZrO_2$ (Fig. 40)
3. Linear thermal expansion of sapphire (Hemex) $c \perp$ rod axis (Fig. 41)
4. Thermal conductivity of $MgAl_2O_4$ spinel (Fig. 42)

In view of irradiated samples a low temperature etching procedure ($T \leq 220 \text{ }^\circ\text{C}$) was developed to allow a future judgement on possible changes in microstructure caused by irradiation effects.

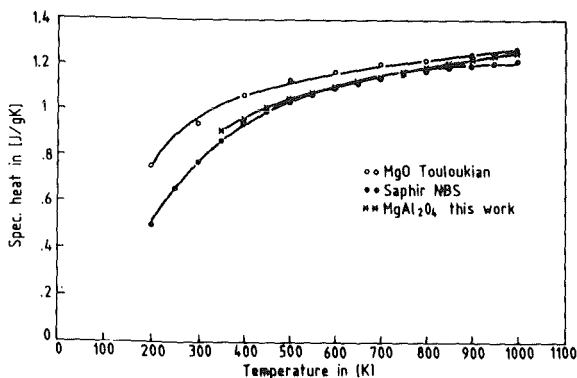


Fig. 39: Specific heat of $MgAl_2O_4$.

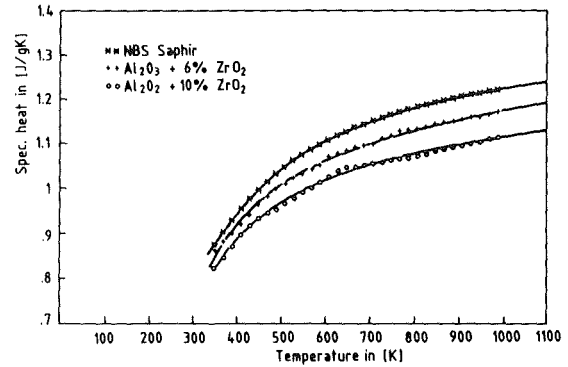


Fig. 40: Specific heat of $Al_2O_3 + ZrO_2$ in dispersion

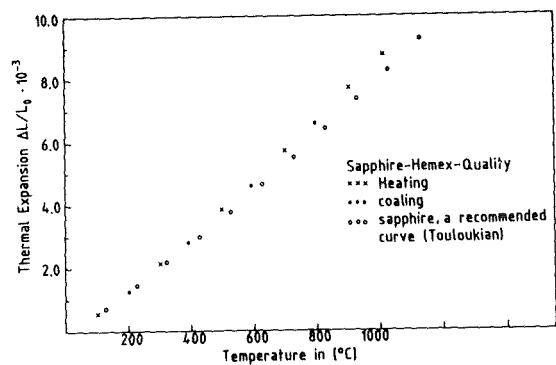


Fig. 41: Thermal expansion of sapphire (Hemex)

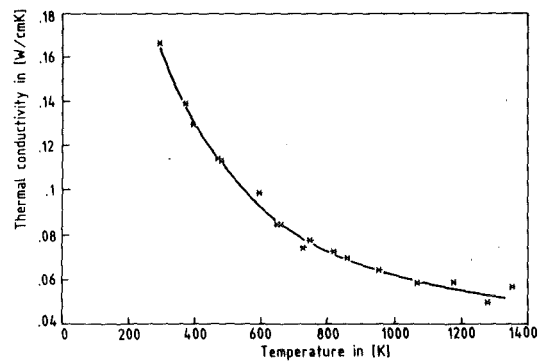


Fig. 42: Thermal conductivity of $MgAl_2O_4$ (polycrystalline)

The investigation of chemical composition, microstructure and mechanical strength of different SiC types was continued. Concerning the influence of the porosity P on Young's modulus and bend strength, a factor of $(1 - P)^3$ can be considered as a first approximation. On the other hand, the dependence of the bend strength on the grain size d appears still uncertain, but it seems to be much weaker than given by a factor of $d^{-0.5}$, as sometimes assumed for ceramic materials.

Hot-pressed SiC which was produced with an addition of 5 % AlN appeared similarly fine-grained ($d \approx 1 \text{ } \mu\text{m}$) as normal HIP-SiC (Fig. 43) and also showed a high bend strength up to about 600 MPa. On the other hand, a rather irregular

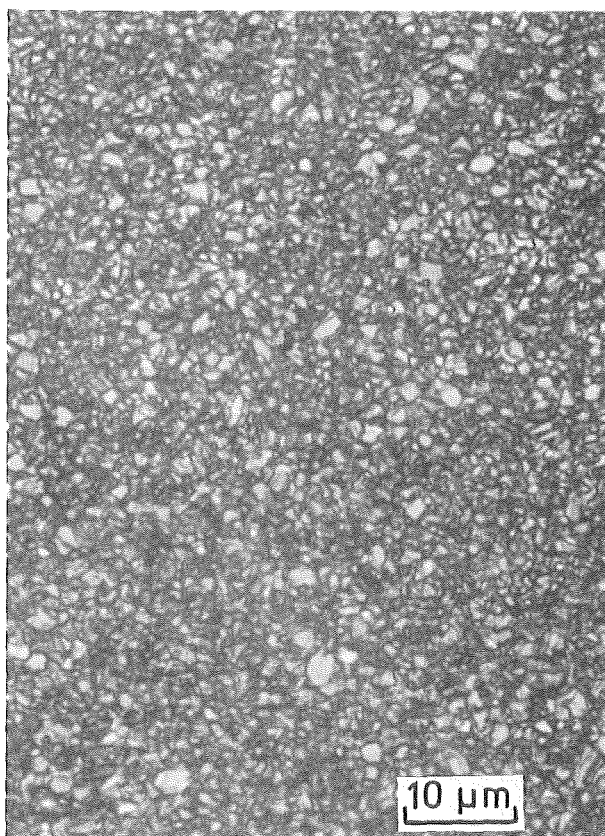


Fig. 43: Microstructure of HIP-SiC with 5 % AlN.

microstructure resulted from the attempt to produce HIP-SiC with 0.7 % boron content (Fig. 44) which was undertaken in order to enhance the helium generation under neutron irradiation. The bend strength of this material was only 218 ± 40 MPa, which is hardly compatible with a general correlation for the influence of porosity and grain size.

In the KfK/KFA/CEA joint irradiation experiment HFR-CERAM D 217/2 (3 dpa, 1500 °C), which is sponsored by KfK, samples of the above-mentioned SiC types will be irradiated together with such of normal HIP-SiC and SSiC qualities, the latter with various porosity and boron contents. The KfK capsule has already been loaded in June 1988, and the irradiation is to start about end of this year.

Based on a multi-phase material conception an experimental test program was started to develop materials with improved mechanical properties in the TiC-SiC-TiB₂ system. For the compositions TiC-SiC 70/30, TiC-SiC 50/50 and SiC-TiC-TiB₂ 50/25/25 some fabrication parameters (hot pressing and cold pressing/sintering) were tested with the first objective to produce highly dense materials. Promising first results were obtained for the TiC/SiC 70/30 composition. The investigations are continued.

Concerning the investigation of various Al₂O₃ grades as candidate materials for RF windows, the inspection of the microstructure and bend strength data in hand suggests that the strength dependence on the grain size is much larger for coarse-grained grades than for fine-grained ones

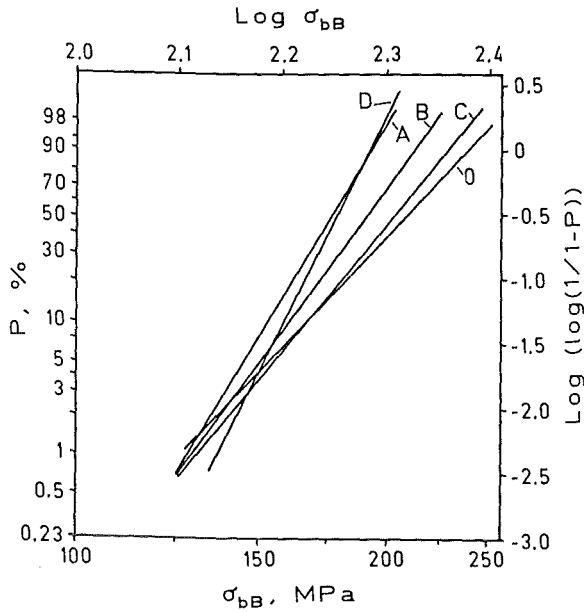


Fig. 44: Microstructure of hot-pressed SiC with 0.7 % B.

For a standard grade of 99.5 % Al₂O₃ (mean grain size 9 μm) the production charge effect on the strength was examined in bending tests. 30 specimens each were cut from four different discs of 115 mm diameter. Fig. 45 (including also a former charge) shows that the higher the mean strength the wider the strength distribution (or the lower the Weibull modulus). Thus the differences in strength will disappear, or the relations will even be inverted, at low failure probability in the range of some % to 0.5 %. Consequently, the charge effect on the mean strength seems to be of minor interest under technical aspects.

The determination of dielectric properties of candidate materials for RF windows was extended by the installation of the measuring facility at 143 - 146 GHz which covers the operational frequencies of the KfK gyrotron development. Consistency of the results was proved by comparison with the established setup at 30 - 38 GHz. Lowest loss tangents amounting to 3×10^{-4} were found in some single crystals of Al₂O₃ ("sapphire") for both frequency intervals. In best polycrystalline materials, this low loss value was only obtained at 30 - 38 GHz, but it is increased to $5 - 7 \times 10^{-4}$ at 143 - 146 GHz.

Step annealing of neutron irradiated sapphire was studied under high vacuum conditions ($p \leq 10^{-4}$ mbar), and the evolution of the dielectric parameters was recorded at 52 MHz, 30 - 38 GHz and 143 - 146 GHz. At 143 - 146 GHz, these experiments are the first dielectric measurements ever realized on irradiated insulator materials. They show a



Staff:
 M. Blumhofer
 W. Dienst
 G. Gausmann
 Ch. Gosgnach
 G. Haase
 R. Heidinger
 V. Karcher
 K.-H. Kurz
 G. Schlickeiser
 B. Schulz
 A. Skokan
 H. Zimmermann

Fig. 45: Weibull plot of the bend strength of AL23 (99.5% Al_2O_3) samples from discs A, B, C, D and from a former production charge O.

recovery by a factor of 1.5 - 2 in the dielectric loss tangent, appearing between 400 and 600 °C for $E \perp c$ and 600 - 800 °C for $E \parallel c$ (Fig. 46). The results at the lower frequencies were compared to the earlier results obtained for annealing in air. No essential difference was found in the GHz range, while the recovery step of permittivity in the MHz range is shifted towards higher temperatures by annealing in air.

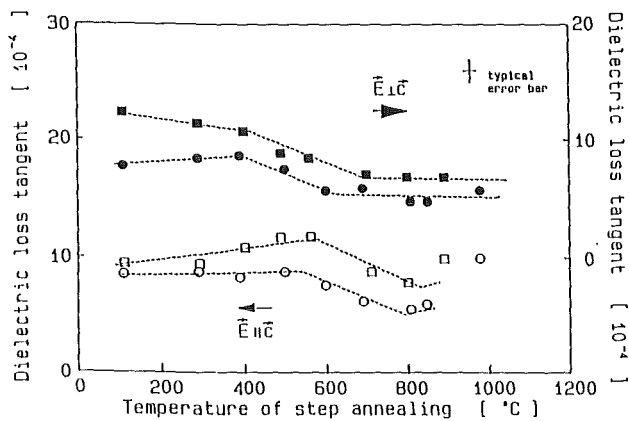


Fig. 46: Evolution of the dielectric loss tangent in sapphire irradiated to 2.6×10^{20} neutrons/cm² ($E > 0.1$ MeV) after step annealing in high vacuum.
 o sample disc with 5 mm height, □ sample disc with 2 mm height

Dielectric measurements of materials in structural parts for Ion Cyclotron Resonance Heating devices were terminated. The dielectric data obtained at 1, 45 and 60 MHz gave evidence that the presently used grade of steatite is extremely variable in its properties and that its replacement by a more controlled grade is promising. On a longer term, it is recommendable to replace it by forsterite or even alumina from the point of view of dielectric properties.

MAT 9.2 Investigation of Fatigue Under Dual-Beam Irradiation

The Dual Beam Facility of KfK was developed as a research tool for materials within the European Technology Programme. The Dual Beam Technique allows the production both of damage and helium in thick specimens by simultaneous irradiation with high energy protons (≤ 40 MeV) and alpha particles (≤ 104 MeV) produced by KfK cyclotrons. One of the objectives is to investigate the influence of helium on the mechanical properties like low cycle fatigue on proposed first wall materials.

1. Development of the Irradiation Facility

The Dual-Beam Facility consists besides the electronics, the process data acquisition system and the He-gas cooling loop mainly of the two beam lines with the diagnostic- and experimental chamber.

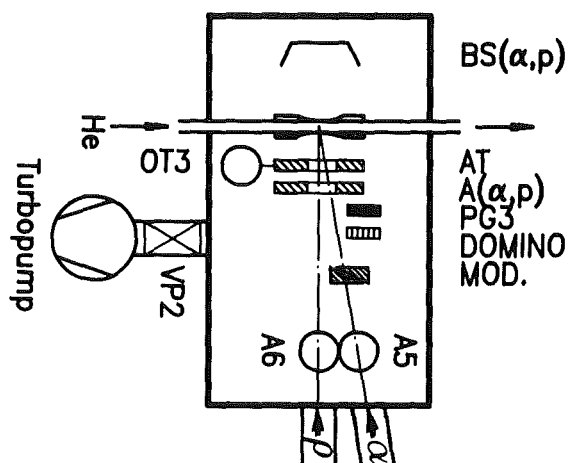


Fig. 47: Schematic drawing of the experimental chamber with collimators (A,AT), degraders (MOD), an optical target (OT), a profile monitor (PG3, DOMINO), a beam stop (BS) and the He-gas cooled LCF-specimen.

To reduce the activity associated with high current irradiations, the experimental chamber, formerly made of stainless steel, was replaced in the reporting period by an aluminium chamber. The first irradiations with comparable beam currents and energies have shown that the activity at the chamber surface is now by more than an order of magnitude smaller. Fig. 47 shows a schematic drawing of the experimental chamber with a rotating, stress-free mounted LCF-specimen at the cross-point of both beams. An open technical problem, which was related to temperature measurement and control, could be solved. Tiny thermocouples welded on the specimen surfaces at different points outside the active deformation length together with sophisticated transmitting systems have been successfully

tested. An independent thermo-optical system for measuring the temperature at the center of the gauge length is working but has still to be optimized to run also at high beam currents beyond 20 μ A.

2. Microstructure of Helium - Implanted 1.4914

Helium has been shown to cause major changes in the response of metals to radiation effects. Since fusion neutrons are producing much more helium than fast reactor neutrons at comparable displacement rates, the studies of helium interactions with displacement effects are of particular relevance to fusion reactor materials research. Besides mechanical experiments under real loading conditions, the knowledge of the microstructure before and after mechanical tests of irradiated specimens is inevitable not only for the understanding of radiation-enhanced diffusion, solute segregation and phase stability but also for reliable lifetime predictions of helium-containing components.

During the reporting period transmission electron microscopy (TEM) was done on specimens which were He-implanted between 220°C and 720°C (Fig. 48). Before the implantation the martensitic steel 1.4914 (heat 51482) was austenitized and tempered at 1075°C/30 and 750°C/2h, respectively. The TEM-micrographs in Fig. 48 show very small defect clusters ('black dots') at low temperatures (a), and a temperature-dependent He-bubble evolution between 300°C and 720°C (b-f). Above about 550°C all bubbles are pinned at dislocations (e), grain and lath boundaries or at the surface of primary $M_{23}C_6$ -precipitates (f). An analysis has shown that under the assumption of a Van der Waals law almost all implanted helium is found within these bubbles.

The helium-induced swelling of 1.4914 specimens remains at all irradiation conditions substantially below the swelling found in simultaneously He-implanted control samples of austenitic steel 316 L. This is consistent with results of other experiments. A comparison of the high He/dpa-ratio in this study with much lower ratios (1/ G.P. Walters et al., HARWELL, AERE R 12620, 1987; 2/ P. Dauben et al., J. Nucl. Mat. 141-143, 723, 1986) but similar helium contents leads to the conclusion that the swelling-rate in 1.4914 is mainly dependent on the amount of helium. Consequently the swelling behaviour is only marginally affected by the defect production rate and the damage level, at least below about 40 dpa.

3. Low Cycle Fatigue during and after Irradiation

To assess a possible helium-effect on the low cycle fatigue behaviour, some LCF-specimens (H-GRIM-geometry) made of MANET 1 were irradiated at 420-450°C up to about 0.5 dpa with either no helium or about 50 appm He. These specimens were successfully LCF - tested in the Hot Cells and are going to be investigated with electron microscopic methods. In addition the irradiation of low cycle fatigue specimens with experimental parameters defined in the NET-matrix have just started. Because tensile tests have shown (previous Semi-annual Report) that the transition from irradiation hardening to softening is around 400-450°C, the comparison between

not irradiated and irradiated specimens should not be affected by the definition of the gauge length of H-GRIM-specimens.

Whereas H-Grim-specimens are suitable for postirradiation LCF-experiments, they have to be replaced in future In-beam LCF-experiments for various reasons. Therefore a new hollow LCF-specimen was developed with a square cross section and a constant wall thickness within the irradiated gauge length. These square specimens have several advantages compared to other tubular specimens in charged particle irradiations and their mechanical stability was successfully tested under different conditions.

Staff:

S. Baumgärtner
G. Bürkle
R. Lindau
A. Möslang
D. Preininger
G. Przykutta

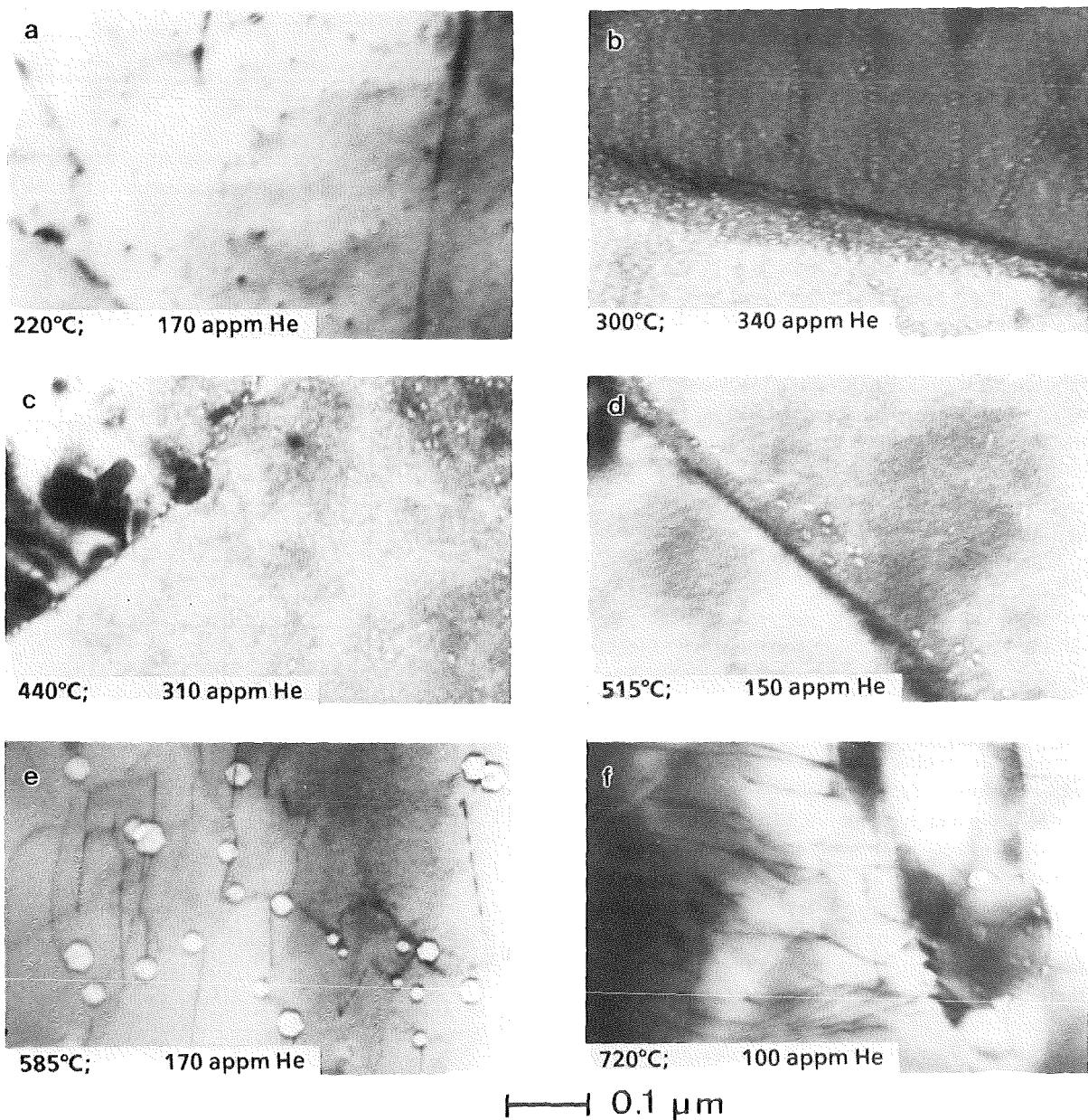


Fig. 48: TEM-micrographs showing the evolution of microstructure in He-implanted and tensile tested ($T_{irr} = T_{test}$) martensitic steel 1.4914. (a) very small defect clusters (black dots); small He-bubbles at dislocations, in the matrix and at lath boundaries (b-d); faceted He-bubbles pinned at dislocations (e) and at M₂₃C₆-precipitates (f).

MAT 18 Development of Low Activation Ferritic-Martensitic Steels

First wall and blanket structures of fusion machines will be made radioactive during operation what renders more difficult maintenance, recycling or waste disposal. To reduce these problems it is necessary to avoid the presence of certain alloying elements (or some isotopes thereof) and to minimize impurity elements exhibiting unfavourable activation properties. A literature survey has shown that in recent years 9-12% ferritic/martensitic steels have been devised in which mainly Mo and Nb have been replaced by additions of W or enhanced levels of V or Mn. The results obtained show that for the modified materials the standard of commercial alloys, like 1.4914 or HT9, has not been fully reached, especially with regard to an adequate balance of tensile and impact properties. Research efforts underway at KfK/JEN to improve this situation have been described in recent semi-annual reports (KfK-reports 4165, 4339 and 4418).

- a) Investigation of Ta-Ce and Ta-Hf bearing chromium steels:

For the two melts, No. C 857 and C 858, continuous transformation diagrams have now been determined (Fig. 49a, b). Compared to MANET 1, there are only minor changes in the transformation kinetics: the pearlite formation is slightly enhanced and the transformation point A_{c1} in heating is somewhat higher (830 vs. 790°C), whereas the martensite formation temperature is practically unchanged.

- b) Effect of varying δ -ferrite contents on the impact properties of martensitic Cr-steels:

Instrumented impact tests were carried out between -80 and +160°C on MANET-base steels with $9 \leq Cr \leq 14$ wt-% varying in δ -ferrite content between 0 and 24%. The results are shown in Fig. 50. Trace amounts of δ -ferrite (0.5%) appear favourably to lower the ductile-brittle transition temperature. Higher δ -ferrite contents, however, clearly increase the transition temperature above room temperature and, furthermore, to decrease the upper shelf energy markedly. SEM investigations revealed that the δ -phase is surrounded by a brittle dendritic carbide phase ($M_{23}C_6$). A preliminary explanation for the observed impact behaviour is as follows: The soft δ -ferrite traces prevent early stress concentrations during the impact event, and thereby the ductile failure mode persists even somewhat below room temperature. With higher δ -(and Cr-) contents two factors lead to the onset of cleavage fracture at increasingly higher temperatures: the more massive carbide precipitation and the increased transition temperature of the δ -phase (which is richer in Cr than the martensitic matrix).

Material: TAHF No C857
 Austenitizing: 1075° 15min
 Grain size: ASTM 7,5-8,5

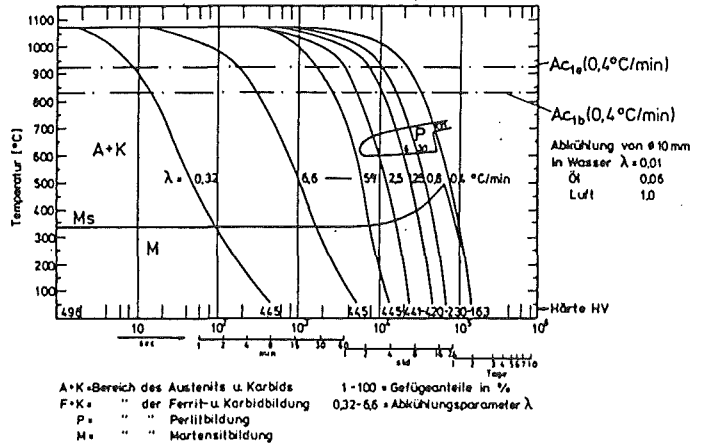


Fig. 49a: Continuous time-temperature-transformation diagram for low activation melt C 857 (Ta + Hf bearing)

Material: CETA No C858
 Austenitizing: 1075° 15min
 Grain size: ASTM 8-8,5

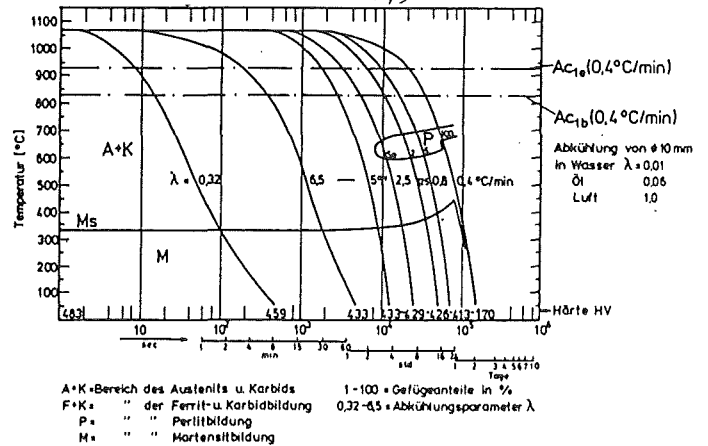


Fig. 49b: Continuous time-temperature-transformation diagram for low activation melt C 858 (Ce + Ta bearing).

Staff:

- K. Anderko
- E. Materna-Morris
- W Meyer
- L. Schäfer
- M. Schirra

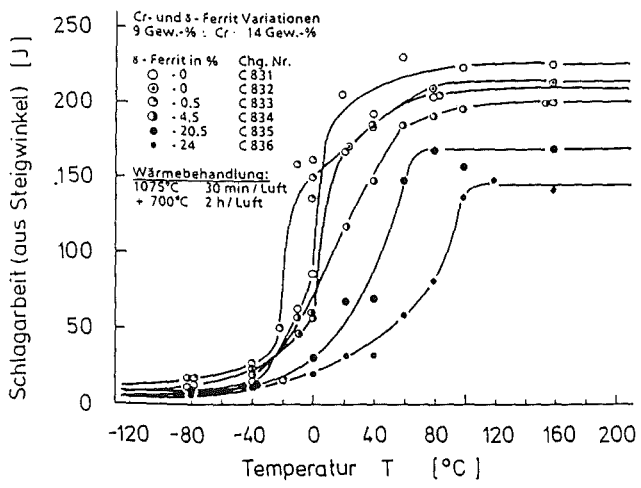


Fig. 50: Impact energy (J) vs. testing temperature of martensitic steel with 0-24% δ -ferrite phase

N 1 Design Study of Plasma Facing Components

First Wall Testing

A test program is planned at KfK for testing first wall (FW) sections in order to:

1. Provide an experimental basis to improve confidence in the prediction of thermal fatigue life by:
 - (a) Validation of computational methods for
 - thermo-mechanical analysis
 - crack initiation by cycle plastic deformations
 - fatigue crack propagationin complicated geometries.
 - (b) Life time determination including
 - observation during life
 - study of failure modes for prototypic FW section under representative thermomechanical conditions.
2. Compare integral behaviour of different FW concepts including protection.

The test specimens will be tested under mechanical boundary conditions and thermal loads as close as possible to those of NET.

Heater Pretest

For FW testing the specimen will be positioned in a vacuum chamber; the specimen will be actively cooled with water and will be heated by thermal radiation in a cyclic manner. A crucial part of the test apparatus will be the radiative heater to be operated in an on/off mode at high heat fluxes and up to very high temperatures. Promising candidate heater materials are different types of graphite. The necessary maximum temperature of 2200°C seems not to be a problem for graphite but experience is missing how long such a heater will stand the steadily changing heat fluxes accompanied by temperature changes of about 1000K within typically one minute in each cycle. At least 5000 cycles are anticipated as a reasonable life time of the heater.

A program is going on to pretest the lifetime of sample heaters under typical conditions. A test apparatus was designed and constructed. Heater tests began in August with a CFC heater. Maximum heat fluxes of 75W/cm² at maximum heater temperature of 1850°C were reached in September. The first heater used since startup of the apparatus has so far experienced about 150 cycles at different power levels without showing any signs of fatigue

(no increased electrical resistance or mechanical desintegration).

A draft design of the main test facility and a detailed design of the main power feed-throughs in the vacuum vessel wall were completed. Procurement of the main test facility will be started as soon as enough confidence in the reliability of the heater concept has been gained with the pretests.

Thermomechanical Analysis

Within a reactor the FW is thermally loaded by a surface heat flux due to radiation and particle impact and by an „internal heat generation due to neutrons. In the test program the effects of neutrons are excluded.

As a consequence, the thermal loading in the tests, cause different temperature fields and stress distributions as compared to the fusion environment. The stress fields have been compared to qualify how representative the test program could be. Of special interest are the stress states near the fixation points of the protection tiles. However, the stresses at these locations will strongly depend on the heat transfer from the fixation to the steel structure.

Staff:

E. Diegele

E. Eggert

G. Hofmann

H. Kreuzinger

G. Schweinfurther

Plasma Facing Components, Divertor

The main design issues for the NET divertor are the high heat flux, the physical and chemical erosion, and the surface damage from plasma disruptions. Current divertor concepts consist of a metallic heat sink structure protected by a heat and erosion resistant surface material. In this duplex structure the major thermomechanical concerns are material compatibility, perfect bonding, temperature limits, and cycling shear stresses due to differential thermal expansion.

A NET contract for a two year testing program was approved with the objective to test the behavior of candidate materials and material combinations, including attachment procedures, under operating temperature and stress cycles. The first out of three stages of the contract involves sample specification, sample procurement, and modification of the test facility. The samples have been specified on the basis of finite element calculations with respect to the most appropriate geometry and edge fixation. A total of 180 monolayer type samples out of 45 different material grades have been ordered by the NET team, two thirds of which are graphite grades or carbon/carbon composites, and one third being refractory material alloys. Regularly, two samples of each kind will undergo the cycle tests.

Facility modifications, which are essentially complete, consist of commissioning of the cooling circuit, installation of the gas supply system, and preparations for the computerized data acquisition. For the temperature monitoring during the cycles several pyrometers have been tested. It turned out that two-color pyrometers are unsuitable because of disturbing signals emitted by the plasma flame. Instead, wide band pyrometers operating in a proper wave length range (> 1.5 micrometers) revealed good results, but need calibration with regard to the material dependent emissivity. The critical path is determined by the sample alternator, including the programmable drive unit, which are ready for fabrication and procurement, respectively.

Besides the current testing program a proposal for a 300 kW divertor test facility was drafted for thermomechanical and thermohydraulic performance and endurance tests with prototypical divertor plate sections. These technology oriented medium scale tests are considered as a necessary step beyond the small scale testing effort.

In divertor design studies the design heat flux is a key parameter which has to account for various uncertainties. Of major importance are the design, fabrication, and assembly related geometrical imperfections, which have been assessed for the NET divertor in terms of load peaking factors. Values of the order of 2 to 3 were obtained and are attributed to the extremely grazing incident angle of the particles. Several design rules were derived from the results [1].

Publication:

[1] K. Kleefeldt:

Load Peaking at the NET Divertor due to Design related geometrical Imperfections,

To be published at the 15th SOFT, Utrecht, September 19-23, 1988

Staff:

G. Class

K. Kleefeldt

K. Schramm

E. Stratmanns

E. Wolf

N 2 Shield Design Studies

Work on the NET shielding blankets will be completed with the design of a water cooled outboard shielding blanket for the Extended Plasma Version. As in the previously described variants of the NET normal version, the shielding module is a box made of steel sheets with a high water fraction. The new feature is that the first wall equipped with poloidal cooling tubes and graphite tiles will be integrated into the structure of the blanket box. This also requires to attach copper sheets to the lateral box walls for passive plasma stabilization.

The temperature and stress distributions in the blanket box equatorial cross-section exposed to the maximum load were calculated using the ABAQUS computer code. The data indicated in the preceding report (KfK 4418) were used in designing the first wall. The coolant pressure was assumed to be 10 bar. Figure 51 shows half the cross-section of the box with the calculated von Mises equivalent stresses and the primary and secondary stresses superimposed. The maximum value is 308 N/mm². It occurs in a restricted zone at a temperature around 100 °C. The rest of stress values in the entire box cross-section are lower.

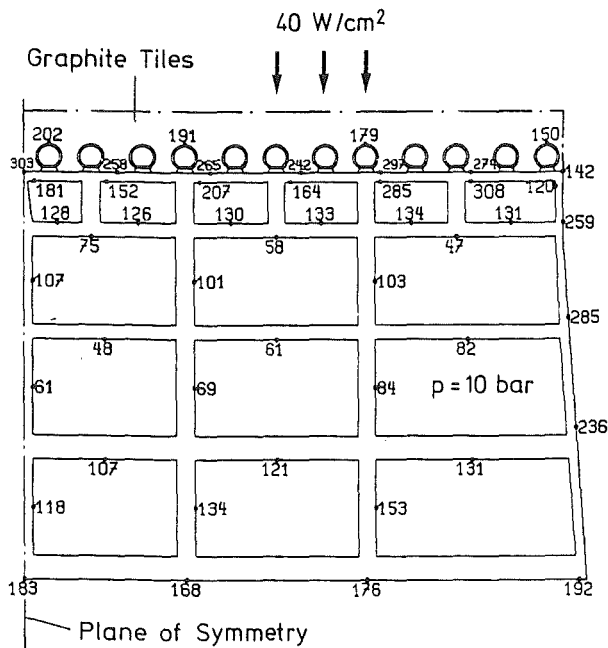


Fig. 51: Outboard Shield Blanket von Mises Equivalent Stresses [MPa]

Figure 52 shows the deformation of the box cross-section 50 times enlarged. It is surprising to see that the deformations of the lateral walls are relatively large. They are caused by the relatively high mean temperatures of these walls, generated by the copper attached to the external faces. The copper layer must be very carefully dimensioned

A further stress analysis of the blanket module was performed for the isothermal condition during baking out. At an assumed coolant pressure of 20 bar and a temperature of

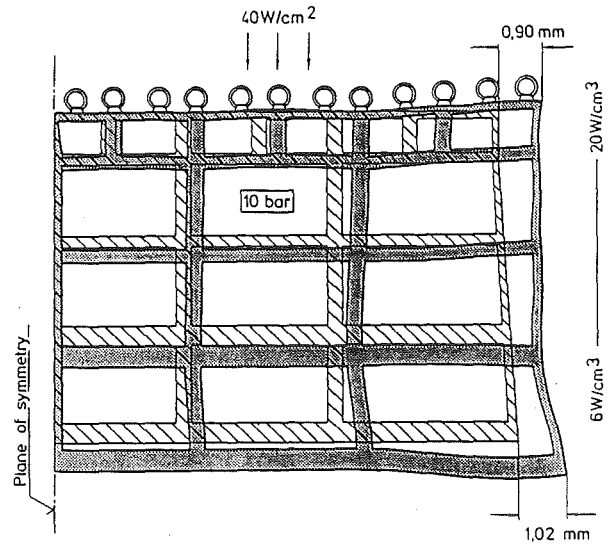


Fig. 52: Outboard Shield Blanket Displacements (Mag. Factor = 50)

200°C a maximum von Mises equivalent stress of 115 N/mm² was derived from the primary membrane and bending stresses; this is well below the admissible limit of about 150 N/mm².

Staff:

- E. Bojarsky
- U. Fischer
- P. Norajitra
- H. Reiser
- L. Schmidt

N3 Development of Procedures and Tools for Structural Design Evaluation

Objective of the work is to accumulate knowledge on computational tools to get more reliable lifetime predictions for high heat flux components.

During the previous period investigations were dedicated to

- inelastic stress analysis
- crack growth analysis
- lifetime predictions for ceramic windows

Inelastic stress analysis

A comparison between different plasticity models has been performed. The models selected have been a simple plasticity model with cyclic isotropic or kinematic hardening, the ORNL plasticity and the Robinson plasticity model. They have been applied to a thermally shocked plate.

Crack growth analysis

Some first wall designs under discussion use multilayer constructions.

Therefore a three layer composite has been investigated to compare its stress intensity factors with that of a homogeneous material. The crack has been modelled as a straight-through-crack. The stress intensity factors for 2-D plane strain have been calculated for tension and for bending loads. On pure tension for example the deviation from the stress intensity factor in the homogeneous material is about 6% as the crack has penetrated 90% of the base material.

Lifetime predictions for ceramic windows in fusion reactors

The KfK gyrotron with a cylindrical wave guide works in the TE₀₃-mode and therefore a power distribution as shown in Fig. 53 results.

The ceramic window separating the reactor vacuum and the vacuum of the gyrotron is heated up due to dielectric losses. The temperature gradients in the window cause thermal stresses and especially in case of ceramic windows the tensile stresses are of high importance for lifetime predictions. These stresses are the basis for lifetime evaluations for different candidate materials. The stationary heat conduction equation was solved analytically. Figure 54 shows the temperature distribution after reaching the stationary state in a normalized representation. Different cooling conditions are included by the varying Biot-number B.

Due to the strong inhomogeneous temperature distribution thermal stresses are generated. Here especially radial and tangential stresses are of interest because a thin disc is

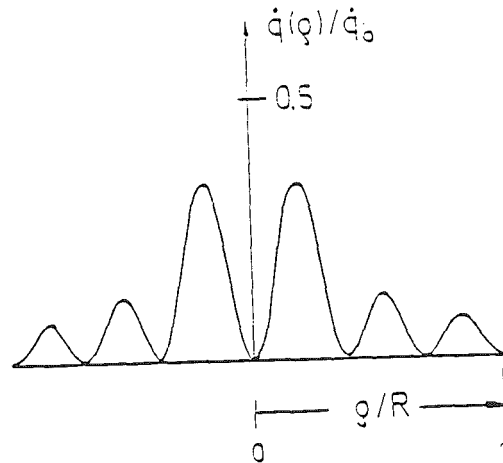


Fig. 53: Radial heat source distribution

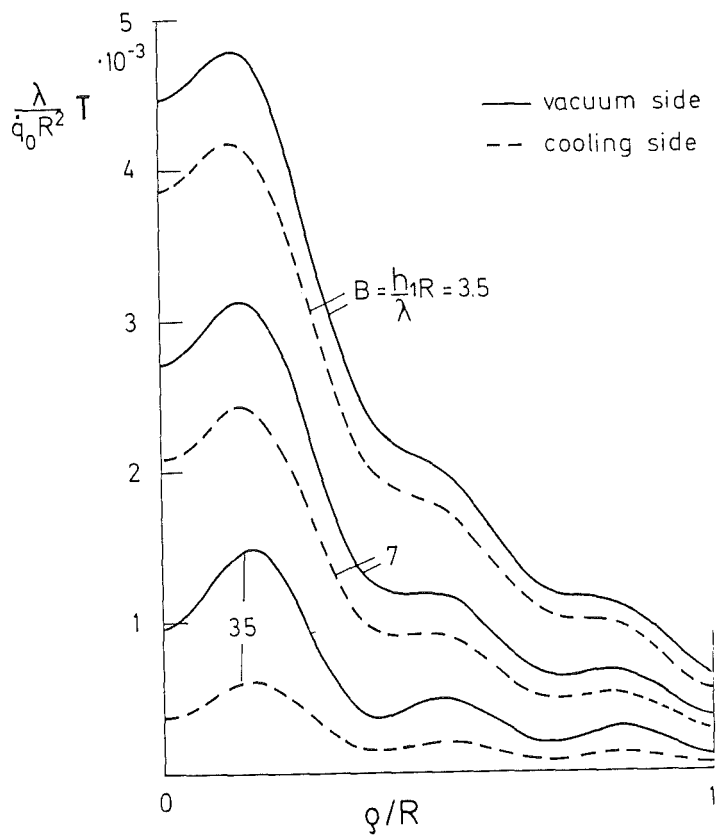


Fig. 54

characterized by $\sigma_z = 0$. The related stresses are plotted in Fig. 55. The radial stress component is a compressive stress throughout the whole disc. The tangential stress is compressive in the center but it reaches high tensile stresses in the outer disc parts. These tensile stresses are responsible for the failure of the ceramic window.

A first failure possibility is given when the thermal stresses reach the tensile strength. Since there is a large scatter in strength of ceramic materials and there is a difference in size of strength test specimens and component a statistical evaluation [1] is necessary.

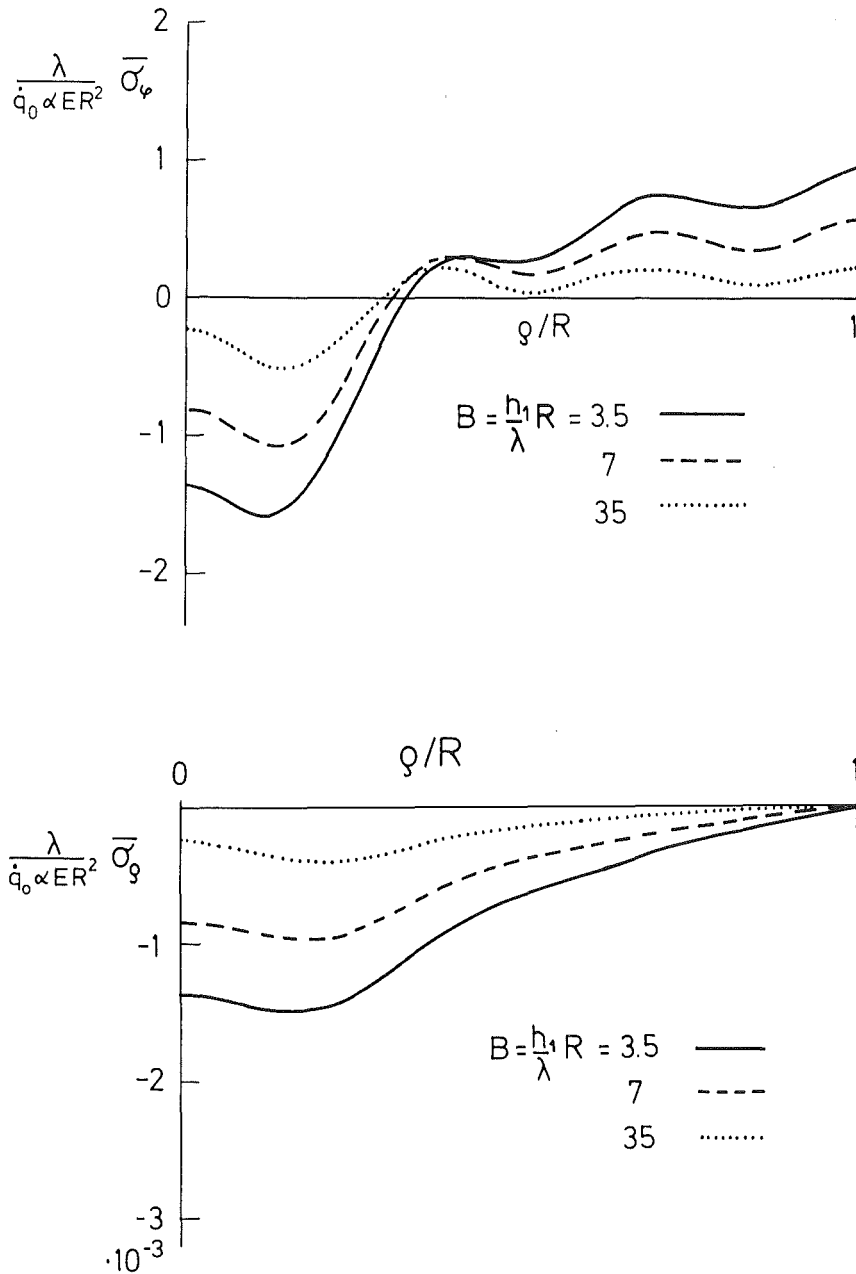


Fig. 55

Even if the strength is not exceeded the stresses in the ceramic window may cause failure by subcritical extension of small flaws or cracks after some time of operation. The crack growth properties have to be measured for all candidate materials.

For determination of subcritical crack growth data a procedure based on lifetime measurements was developed which allows to measure crack growth rates less than 10^{-12} m/s [2].

First measurements were performed on Al_2O_3 (Vitox) and AlN at $60^\circ C$ in fluor-carbon FC43 as the environment. The results are represented in Fig. 56 as v-K-curves, where K is

the stress intensity factor. An important superiority of AlN compared with alumina is evident.

References:

- [1] D. Munz, ICFRM-3, to be published in conference volume.
- [2] T. Fett, D. Munz, Comm. Amer. Ceram. Soc. 68 (1985), C213-215.

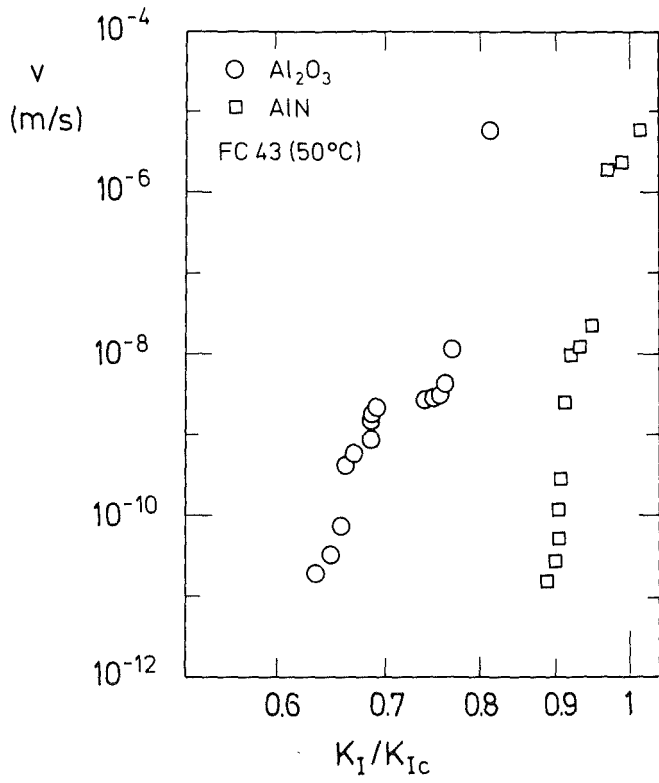


Fig. 56: v-K-curves for Al_2O_3 and AlN

Staff:

E. Diegele

T. Fett

D. Munz

N 5 Development of Theory and Tools for Evaluation of Magnetic Field Effects on Liquid Breeder Blankets

In order to investigate key features for the development of a self-cooled liquid metal test blanket for the Next European Torus an extensive experimental program MEKKA (Magnetohydrodynamik Experiment in Natrium-Kalium Karlsruhe) has been initiated at KfK presented in previous semi-annual reports.

In a first step experiments with straight ducts of circular or rectangular cross section and with ducts having expansions and contractions are conducted using a normal conducting 2 Tesla dipole magnet and eutectic sodium-potassium as liquid metal.

The Flow Channel Inserts

To reduce the MHD pressure drop in the present selfcooled liquid metal blanket design novel flow channel inserts (FCI), as proposed in [1], are employed. With these FCI the load carrying walls and the electric current carrying walls are separated which allows designing the cooling channel structure according to the mechanical needs.

The flow channel insert consists of a thin current carrying inner wall which is insulated by an oxidic layer from the outer wall (Fig. 57). The outer wall has a higher wall thickness in order to stiffen the FCI and to support the inner layer. A slot which may be located at any position at the circumference provides the pressure equalization between the duct and the liquid metal filled gap around the insert.

A proof of principle test should show a reduction of the MHD pressure drop according to the reduction of the wall conduction ratio by introducing the flow channel insert. Beyond this test all questions arising from 3-dimensional MHD flow in FCI's like circumferential pressure differences or collapsing forces acting on the thin inner FCI wall have to be investigated.

Flow channel inserts are developed in cooperation with the industry (MBB). The outer steel sheet of the FCI is coated by a plasma sprayed layer of $Al_2O_3 + TiO_2$ and by a surface layer of Ni or Cu. The inner steel sheet of the FCI is bonded to the metallic surface layer by a diffusion welding process. It is expected to complete the development of fabrication methods mainly in 1988. Testing of the FCI will start in 1989.

The Experimental Program

The Straight Round Duct without and with Flow Channel Insert

The first experiment in MEKKA is devoted to proof that using Flow Channel Inserts (FCI) reduces the MHD pressure drop.

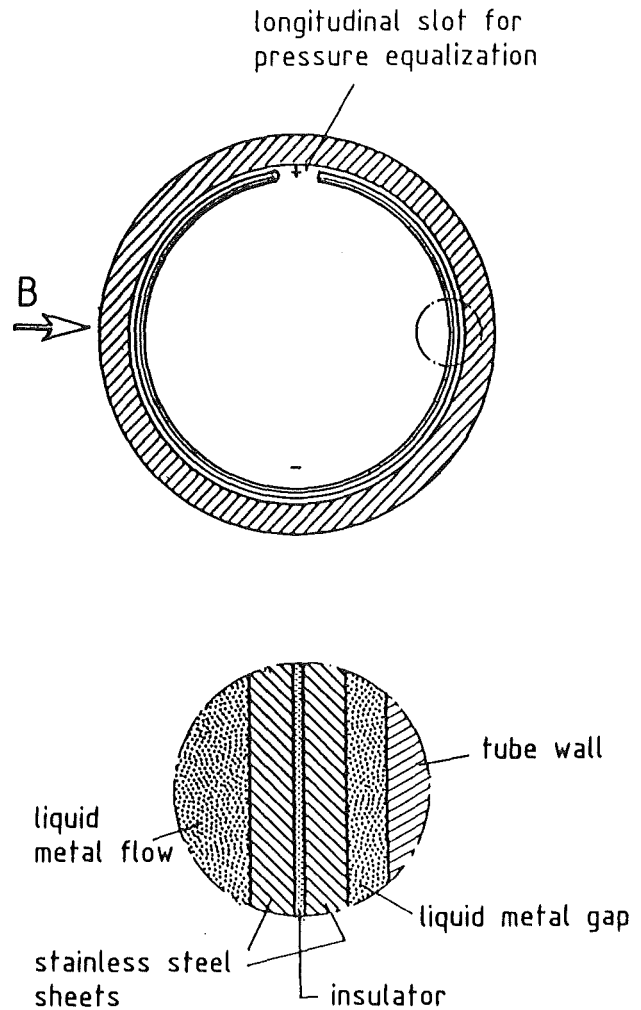


Fig. 57: Principle of a flow channel insert

A straight circular duct with an inner diameter of 130 mm and a wall thickness of 5 mm corresponding to a wall conduction ratio of $C = 0.036$ and a total length of about 6 m is used. Ten axially and 8 circumferentially distributed pressure taps allow for axial and circumferential pressure difference measurements. A flange to attach a traversing mechanism is foreseen to measure velocity profiles at the position of the circumferential pressure taps. A flow straightener at the inlet of the circular ducts consisting of two perforated plates followed by a honeycomb grid flattens the profile at the entrance.

The Flow Channel Insert will be introduced through a flange opening at the downstream end of the test section. The longitudinal slot is aligned with the axial pressure taps on the side to enable axial pressure drop measurements. A simplified version of an FCI is used for this first MHD proof of principle experiment. The 0.5 mm thick inner wall is electrically insulated against the outer wall of the FCI by a 0.5 mm thick ceramic paper.

By introducing the FCI the wall conduction ratio is reduced from 0.036 to 0.0039.

The results of the first pressure drop measurements of the thick walled duct are shown in Fig. 58, where the dimensionless pressure drop is plotted as a function of the interaction parameter N (upper values) together with the analytical prediction $dP/dx = C/(C + 1) = 0.035$.

The pressure drop measurements were repeated with the FCI moved upstream into the magnet. The results are also plotted in Fig. 58 (lower value) together with the analytical prediction for the thin walled (0.5 mm) FCI ($dP/dx = 0.0039$).

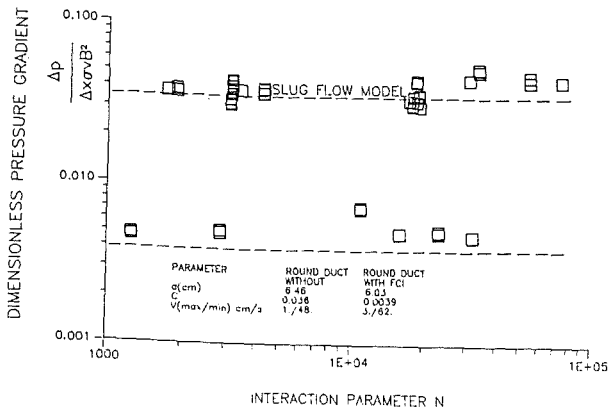


Fig. 58: MHD experiments on round duct

The results show the predicted reduction of the pressure drop by a factor of about 9.

The Joint Argonne National Laboratory (ANL)/Kernforschungszentrum Karlsruhe (KfK) Experiment on Flow Tailoring

As shown in previous reports [2,3] the thermal hydraulic performance of a selfcooled liquid metal blanket may be improved by "MHD flow control".

To show the feasibility of such a "MHD flow control" a joint ANL/KfK test was performed. Testing was carried out at ANL's ALEX facility with a test section fabricated at KfK. The test section consists of a series of expansions, contractions and uniform cross section segments. The design of the test section, the MHD analysis carried out by a 3-D computer code and first experimental and theoretical results were presented in [4].

Fig. 59 shows as an example the measured and theoretically predicted velocity distribution of the liquid metal in the middle of an expansion of the test section with rectangular cross section.

Development of a Velocity Measuring System

The measuring system is based on the "temperature propagation time" method. It sets temperature pulses into the fluid and evaluates from pulse propagation the fluid velocity. The development and testing of the system has

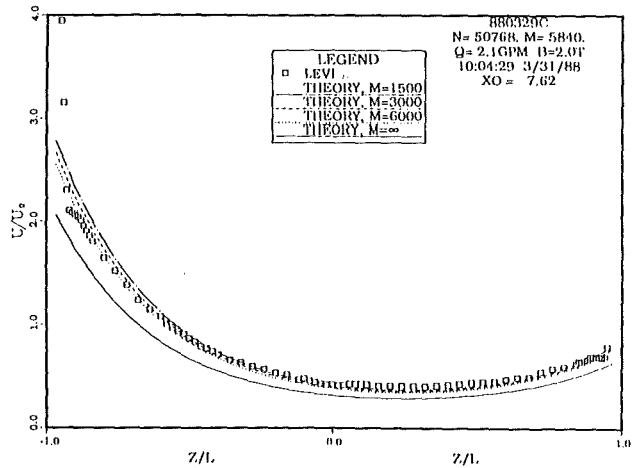


Fig. 59: Transverse velocity profile at middle of expansions

been continued. New measuring heads were constructed. The pulse markers (0.5 mm o.d.) and the thermocouples (0.25 mm o.d.) are stretched by extension wires and a membrane. Pictures of this measuring head are shown in Fig. 60, both a view from the side and one from the top.

The signal amplifiers have been optimized resulting in a 3dB-transmission range of 0.4 to 50 Hz, and an amplification of 10^5 . This dynamic response exceeds the range required for signal transmission. The noise (rms) at the output of the amplifiers could be reduced to a value of 1.5 % of full scale, corresponding to a temperature noise of 0.003 K only.

The evaluation methods were further improved. Fig. 61 shows flow velocity u as function of flow direction α (the measuring head was turned about its axis in a pipe with sodium flow); at the $\alpha = 0$ position the fluid flows from the pulse marker to the sensors. The measurements (dots) indicate that by measurement of propagation time the absolute amount of velocity, $|u|$, can be evaluated but not its direction, α . This is in agreement with the analytical calculations. The velocity vector (directional velocity in sensor direction) shown in the figure as a circle corresponds at the $\alpha = 0$ position with the measured absolute value of the velocity $|u|$.

Staff:

- K. Arheidt
- G. Arnold
- L. Barleon
- V. Casal
- R. Kirchner
- H. Kreuzinger
- H. Kußmaul
- K.J. Mack
- K. Rust
- A. Sterl
- K. Thomaske

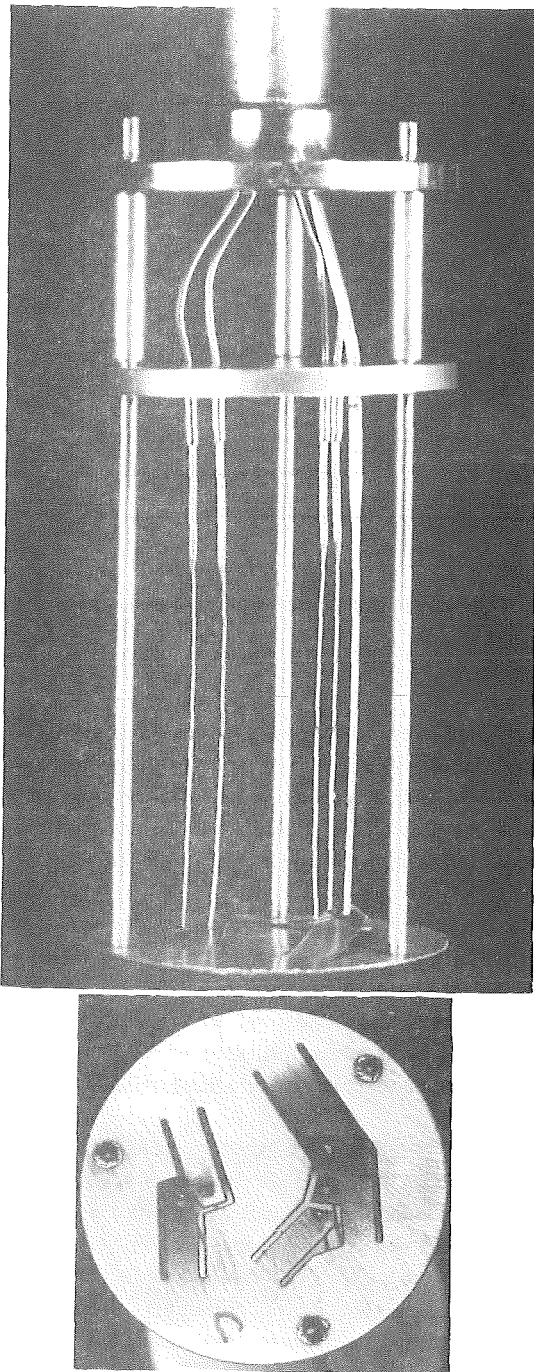


Fig. 60: Measuring head

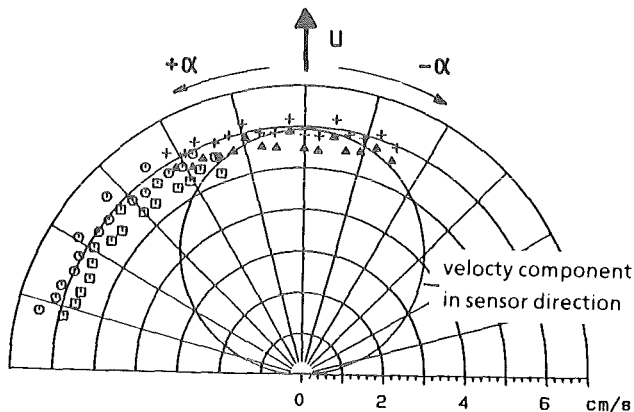


Fig. 61: Velocity (u) as function of flow direction α

Publications:

- [1] Malang, S., Casal, V., Arheidt, K., Fischer, U., Link, W and Rust, K., 'Liquid-Metal Cooled Blanket Concept for NET', Proceedings of the 14th Symposium on Fusion Technology, Vol. 2, 1273, Avignon, France, September 7-12, 1986.
- [2] Nuclear Fusion Project, Semi-Annual Report of the Association KfK/EURATOM, April 1986 - September 1986, KfK 4165/EUR 10534 e.
- [3] Nuclear Fusion Project, Semi-Annual Report of the Association KfK/EURATOM, October 1987 - March 1988, KfK4418/EUR10541e
- [4] Picologlou, B.F., Reed, C.B., Hua, T.Q., Walker, J.S., Barleon, L. and Kreuzinger, H., 'MHD Flow Tailoring in First Wall Coolant Channels of Self-cooled Blankets', Proc. of the ISFNT Meeting, April 10-19, 1988, Tokyo.
- [5] V. Casal, G. Arnold, W. Hame, R. Kirchner, H. Kußmaul, H. Miller: Verfahren zur Messung örtlicher Geschwindigkeiten nach dem Prinzip der Temperatur-Puls-Propagationsmethode, KfK 4369, März 1988.
- [6] V. Casal, G. Arnold, R. Kirchner, H. Kußmaul, H. Miller, W. Hame: Velocity Meter for Local Measurements in Liquid Metals; R.K. Shah, E.N. Ganic, K.T. Yang. Experimental Heat Transfer, Fluid Mechanics, and Thermodynamics 1988, Proc. of the first world conference on experimental heat transfer, fluid mechanics and thermodynamics, Dubrovnik, Sept. 4-9, 1988, Elsevier, New York, Amsterdam, London.
- [7] V. Casal, G. Arnold, R. Kirchner, H. Kußmaul, H. Miller, W. Hame: Velocity meter for local measurement in liquid metal. LIMET 88, Oct. 17-21, 1988.

**N 6 Studies of Pebble Beds of Ceramic
Compounds**

The results of the studies of pebble beds are included in the report on B 1 Blanket Design Studies chapter Helium-Cooled Ceramic Breeder Blanket.

RM 1 Background Studies on Remote Maintenance

Within the framework of this project, development work is carried out on remotely operated connections to be used in NET. This remote connecting technique includes connections of all pipes, electric cables, vacuum lines, and also remote cutting and welding.

In the period under review the following main activities were carried out:

1. Investigation of Remotely Operated Pipe Connectors

For the NET Remote Handling Manual the current state of the art was determined. Data sheets were compiled for all types relevant to NET. Handling tests were carried out with the prototype pipe connectors existing at KfK. Figure 62 shows as an example the ND 250 JET vacuum flange during remote handling test in the FEMO test rig at KfK.

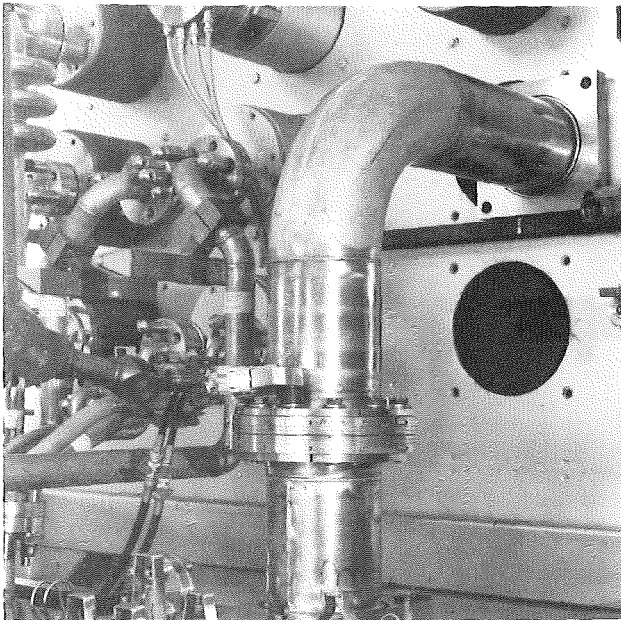


Fig. 62: Remote handling test of a JET-type vacuum flange

The studies conducted in the FLATEST test rig of the corrosion resistance of soft-iron gaskets were continued. The results indicate that soft iron is a suitable material as far as corrosion is concerned.

2. BERT Integral Test Facility

The BERT test facility serves for testing connecting techniques for a prototype blanket module of NET. The remote handling of pipe connectors and also cutting and leaktight joining of individual blanket segments as well as of the complete module within the connector box is to be tested. In the period under review the steel structure and the crane facility were manufactured and installed and the pipe connecting elements were made. Figure 63 shows the BERT test facility.

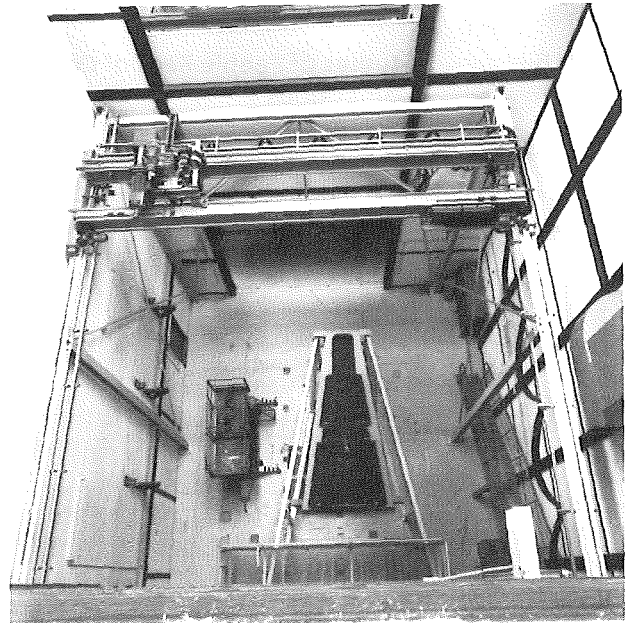


Fig. 63: Top view of the BERT test facility

3. Development of a Remotely Operated Welding System

Within the framework of this project, KfK develops the NET-related remotely operated welding equipment for pipes of larger nominal widths and a universal lip cutting and welding unit.

Current work is being carried out especially in the following fields:

- a) Construction and commissioning of a universal test unit for the parallel operation of various cutting and welding heads.
- b) Development of a lip cutting and welding unit for the top of the blanket module
- c) Development of an orbital welding head for pipes of 100-200 mm nominal diameter.

In the period under review the rest rig was completed, the computer control system commissioned, fabrication of the lip welding and cutting unit continued, and the design of the pipe welding unit completed. Figure 64 shows the control panel as part of the computer control system for the test rig under construction.

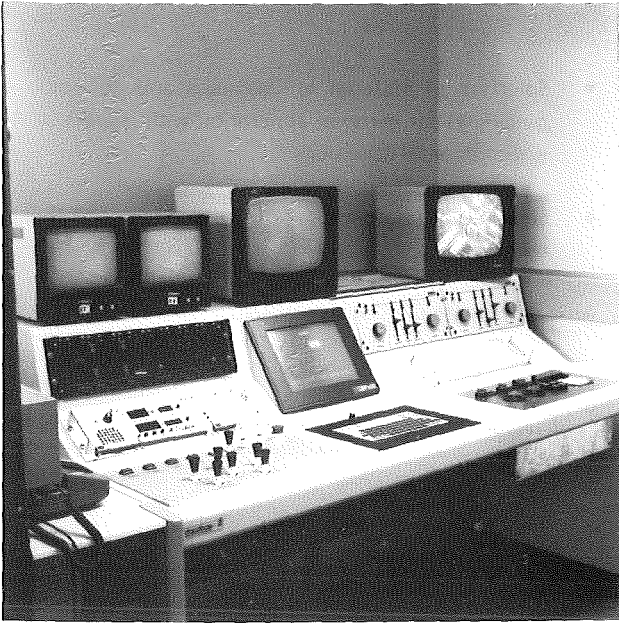


Fig. 64: Control panel of the test facility for remote welding

After completion of the basic development, especially the definition of the welding parameters, future work will be concentrated on the development of application orientated systems and equipment.

Staff:

L. Gumb

U. Kirchenbauer

A. Schäf

M. Selig

M. Trettin

R. Ullrich

RM 2 Mechanical Component Assembly

In order to provide designers and contractors with information KfK cooperates with the NET team in the preparation of a Remote Handling Manual (RHM). It contains a set of General Rules and Design Standards, adapted by NET for components and units of the NET device which require remote handling, and settles guidelines for handling equipment design.

Within the frame of the RM2 contract the work was continued with:

- Definition of the international standards which have to be taken into account at the design of the device and equipment.

- Selection of material for fasteners and definition of guidelines for material application with respect to the environmental conditions.
- Selection of fastener types for general remote handling techniques.

An intermediate report was finished.

Staff:

B. Haferkamp

A. Suppan

RM 3 Handling Equipment for In-Vessel Components

The investigation of an In-Vessel Handling Unit (IVHU) for inspection, repair and replacement of NET in-vessel components was continued. CEA, CEN/SCK, ENEA, JET, SPAR and KfK cooperate in the development of such equipment. It consists of

- a contained transfer unit (CTU),
- a transport unit based on an articulated boom or an in-vessel vehicle movable on telescopically inserted rails,
- various work units with end-effectors attachable to the transporter,
- the control system.

Out of the 9 sub-items of the RM3 technology programme the following tasks were carried out.

SUB-TASK 1: Development of a conceptual design

In-Vessel Handling Unit (boom concept)

In agreement with the NET Team and based on the decision of the RM3 workshop in April 1988, KfK has taken charge to develop an in-vessel handling unit (IVHU) up to a prototype based on the system of an articulated boom.

The overall structure of the IVHU is described in the last semi-annual report and in [1] and [2]. The IVHU is composed of the transport unit and three optionally attachable work units. The boom which consists of 11 links is linked with the trolley of the transporter by means of a combined yaw and roll joint. The latter one is used to compensate angular deflection caused by torques with respect to entering the maintenance ports. The front link of the boom is equipped with a combined pitch and roll joint to align the end-frame (Figure 65) in vertical direction for the attachment of work units. Additional compensation of the boom will be performed by means of telescopic masts integrated in the work units.

The boom links have box cross sections and are linked by yaw joints shown in Figure 66. The axes of the joints are split. Upper and lower joints are composed of three hinges each, connected by axes and spherical roller bearings. The joints are designed to be remotely replaceable from the top and the bottom, respectively. Two drive units in series are actuating one link. In case of a failure each unit can move the link at reduced speed and range. The drive units are shown in Figure 67. Each unit is composed of a planetary roller spindle, a spur gear which can be coupled and decoupled by an electric magnet, a harmonic drive and a DC-brushless motor. The units are installed in casings and are connected on the one side with the link box and on the other end with a swiveling lever sliding on the upper joint axis by means of bearings.

Structural Analysis

The design of the IVHU such that the stresses and strains are within allowed limits turned out to be a difficult problem. Since most of the load is due to the dead weight, simple increasing of the wall thicknesses was not a reasonable way to reduce stresses and deformations. Rather the whole design had to be optimized. This required not only detailed FEM calculations, but also an understanding of the mechanical problem in order to find suitable design solutions. For instance, basic considerations show that a boxtype design is more appropriate than a lattice work (the main loading turns out to be due to torque and not due to bending). For the hinge construction geometry changes could be proposed (Figure 68 which reduce local stress peaks (rounding of etches was not possible). It is quite impressive that the ends of the link boxes had to be closed by front plates thicker than the walls of the boxes. This is necessary to avoid parallelogram-type of deformations. It may be concluded that the realization of the IVHU as an articulated boom (without any additional support) should be possible. However, stresses and deformations are close to the allowed values and therefore have to be checked carefully.

EDITH - Experimental Device for In-Torus Handling

In agreement with the NET Team KfK has taken charge to construct EDITH (Figure 69) in 1989. The specification of this experimental device for in-torus handling is finished and a call for tender was launched. EDITH is supposed to become the test facility for the development of in-torus remote maintenance techniques of fusion devices. It consists of

- the support structure,
- the articulated boom consisting of three through four links. The boom is connected with the support structure. The end-frame for the attachment of work units is linked with the front link of the boom by means of a combined pitch and roll joint,
- a work unit dummy with integrated lifting device to simulate the taking over of heavy loads.

In a later stage EDITH can be extended to a complete prototype of an in-vessel handling unit for NET which will serve for the investigation of maintenance tasks and procedures in a mock-up, the first assembly of the NET device and the training of personnel.

SUB-TASK 2: Overall Geometry Measurement

For the remote maintenance of fusion machines a surveying system will be needed for measuring the geometry of

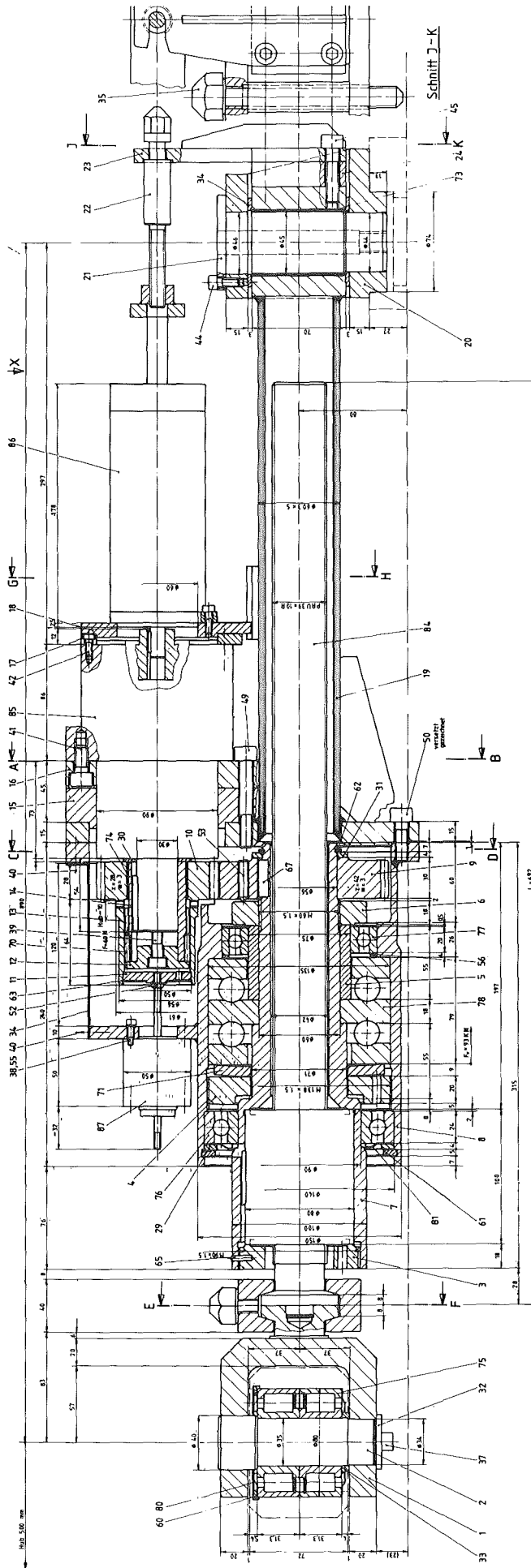


Fig. 67: IVHU drive unit

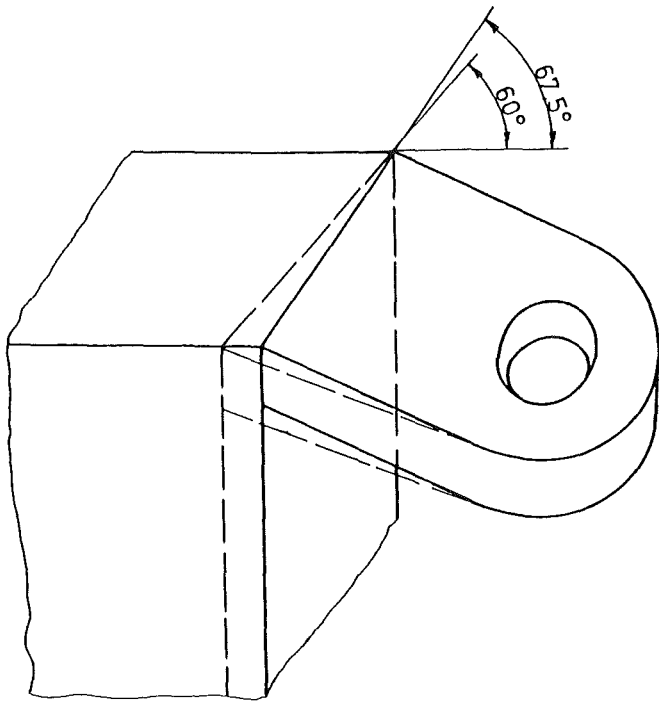


Fig. 68: Proposed geometry changes

components outside (ex-vessel) as well as inside the vacuum-vessel (in-vessel).

Ex-vessel surveying

The remote-controlled and CAD-supported surveying system GMS (Geometry Measurement System), developed by KfK, is equipped with two digital theodolites, a laser- and a camera-theodolite, completely controlled by a computer [3]. To show the feasibility of the GMS-draft a prototype system, equipped with a single camera-theodolite (Figure 70) is built up presently. The software needed for the data transfer CAD→GMS and the software for the control of the surveying process is already implemented and successfully tested. During the whole surveying process the operator is guided interactively by the GMS-software.

After first surveying tests with an aluminium model, the GMS-prototype was already used twice for concrete surveying tasks:

- surveying the positions of thread feeders which are used for dynamic surveyings of the movements of the TFTR-Maintenance-Manipulator
- surveying the joint positions of EMIR (Extended Multi Joint Robot)

Up to now the operator has to find the target points only by knowing the nominal point coordinates. For marking the positions of the target points a computergraphic will be selectively superimposed the TV-picture. This graphical support for the operator will be realized using an IBM-AT

fitted out with a special image processing board; the required hardware is ordered and the software still has to be developed.

In-vessel surveying

In order not to break the vacuum, periscopes have to be used for the in-vessel surveying. Based on the experiences with the ex-vessel surveying a first design concept for a theodolite periscope has been outlined [3]; for building up detailed designs definite informations about the in-vessel surveying processes are needed.

SUB-TASK 3: Boom Position Monitoring

The supervisory control system (SCS) concept [5] was detailed with respect to an implementation on mainly three classes of computers:

- a remote handling workstation (RHWS),
- a remote handling section controller (RHSC)
- the local equipment/device controllers (LEC).

The functions of the SCS were attached to the computers of the control system. Special attention was paid to two interfaces: (1) the model transfer interface between the CAD system and the RHWS, and (2) interface between the RHWS and the RHSC. The integration into a supervisory control system poses special demands on the motion control (RHSC), not usual in conventional controls for telemanipulation or robotics. These requirements result from the close interaction between the supervisory control level and the motion control. The central feature in this context is the possibility of interrupting and influencing running programs as a consequence of supervision.

The following features are necessary:

- abortion of a program at once or after the actual instruction,
- interruption, performance of manual or other programmed work, and resumption after an admissibility check by a special monitor,
- continuous manual corrections of a program (overwrite) or discrete offset processing

Other requirements are: single command execution, attaching of special options to MOVE commands (force reflection, geometric restrictions, jigs etc.), backtracking. In each working state of the motion controller user program

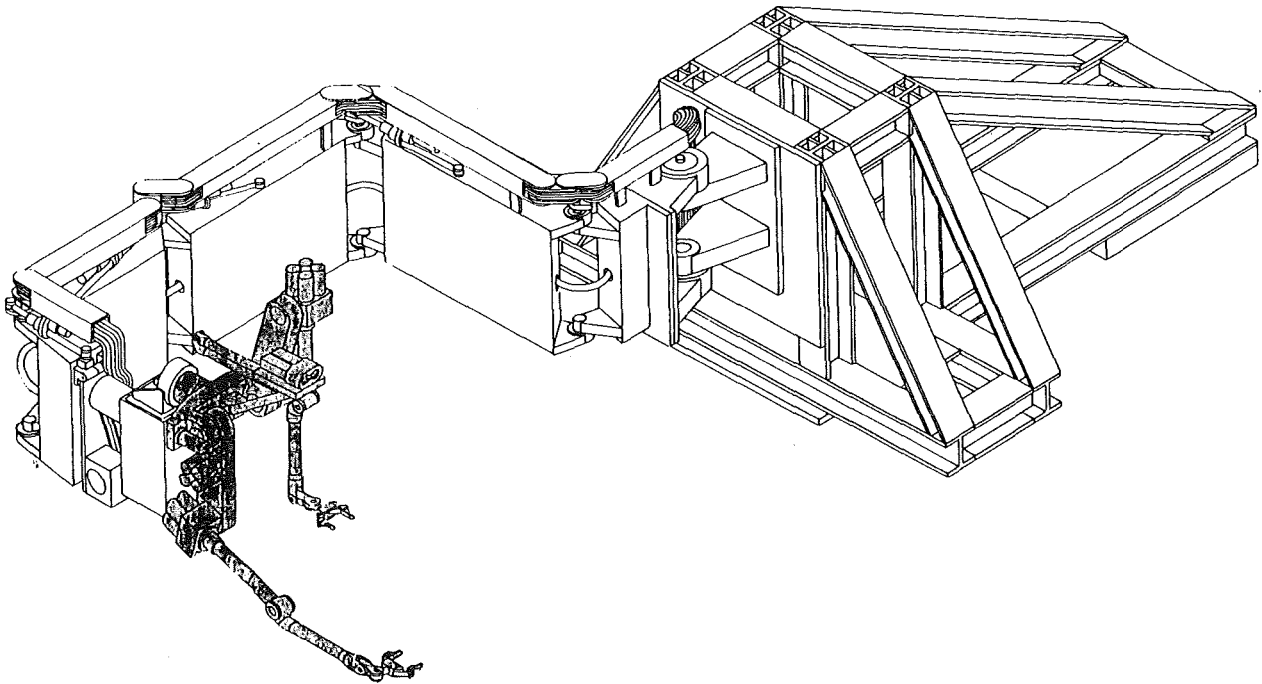


Fig. 69: EDITH

and operating system parameters must be readable (interrogation commands) and writable for displaying the state of the controller and for adapting the behavior of the controller to a special task phase (e.g. new payloads).

The supervisory tasks of the operator are mainly supported by a spatial simulator, implemented as a subsystem on the RHWS. The basic simulator will be run with different user shells, suited to the various phases of supervisory work. Our actual implementation work is concentrated at this spatial simulator named KISMET (Kinematic Simulation, Monitoring, and programming Environment for Telemanipulation). Figure 71 shows the architecture of the kernel. Special features of KISMET are:

- hierarchical data structure for variable degrees of detail,
- flexible kinematic model (trees, loops),
- programming support by work-frames,
- enhanced collision detection.

KISMET can be adapted to various applications as JET ex-vessel work and NET sections by simply exchanging the databases for the work environment and the manipulators and, eventually, a few specific modules for interfaces. KISMET is now implemented in a test version. Investigations in subtask automation and supervision are underway in the related CATROB [4] project. The CATROB working scene was used for first KISMET tests (Figure 72).

For design purposes of machines and procedures the ROBOT software package has been developed for use inside the Applicon CAD-system Bravo 3. Its main objectives are:

- to define kinematic loops inside the CAD-system and, hence, to allow kinematic design studies in an early stage of a manipulator design
- to prepare the geometrical and kinematical model data (of the manipulator modes as well as of the environmental models) in such a way that they can easily be transferred to a real-time graphical workstation. An example is shown in Figure 72.

This software has been used to model the KfK-NET boom, and then to simulate the boom configuration at various work positions. In these configurations, the relative angles of the boom links have been measured using standard tools of the CAD-system. The measured angles were input to design calculations for the boom, which, in turn, yielded in the need for some minor design (and model) modifications (Figure 73).

The investigation of the NET/EDITH boom dynamics with APPLICON-MECHANISM (ADAMS) was started with modelling the worm gear. The model considers backlash, friction, and the non-backdrivable behaviour of the gear. Furthermore a flexible link and the whole EDITH kinematic and geometry was modelled, the integration of the various dynamic sub-models goes on.

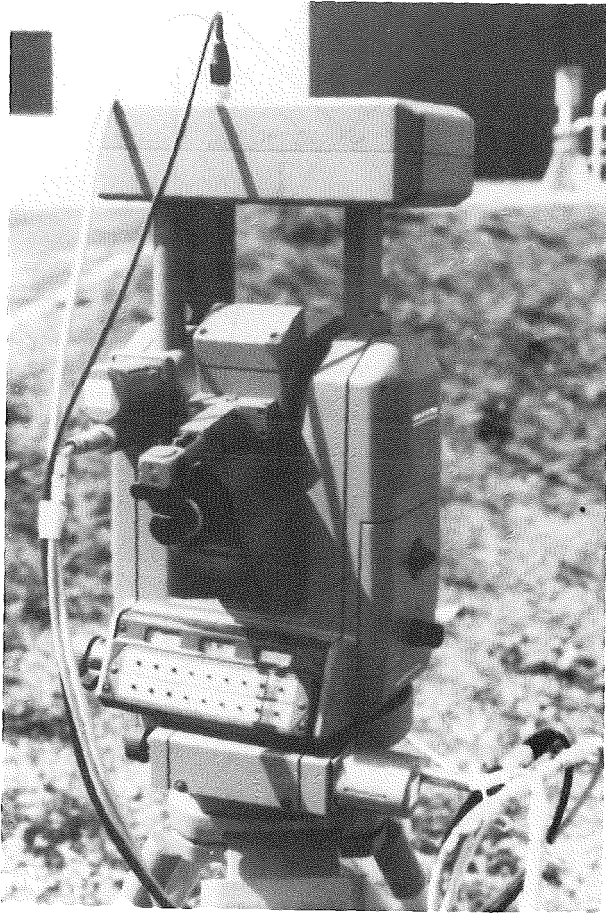


Fig. 70: Computer-controlled camera-theodolite

SUB-TASK 8 + 9: Environmental Conditions

Based on reported sensor surveys for the NET boom instrumentation a group of five commercially available sensors was selected for further investigations and hardening tests: resolvers, inclinometers, ultrasonic proximity sensors, switches, and whiskers. Besides sensor specific test procedures a time schedule and test requirements were worked out also for radiation sensitive components of the in-vessel handling unit [6].

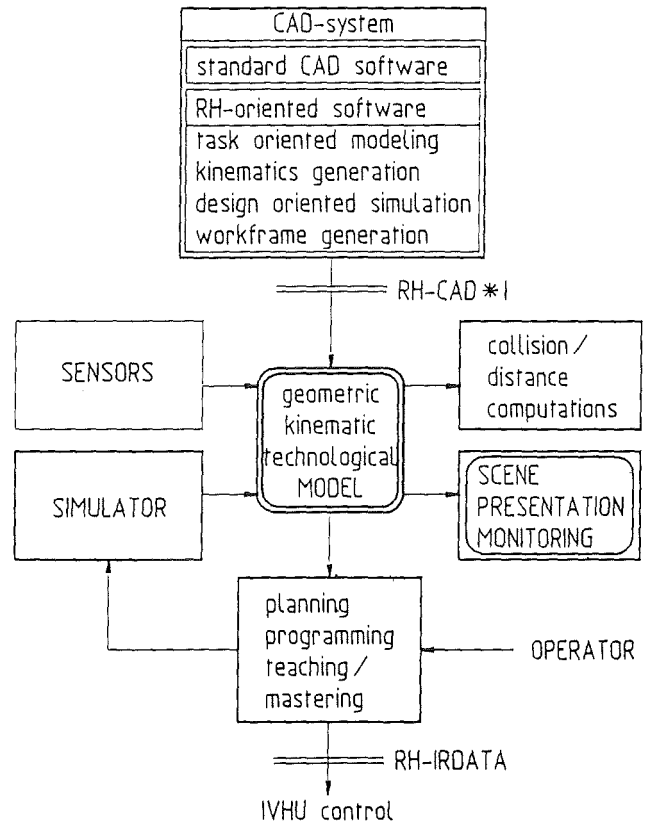


Fig. 71: KISMET kernel architecture

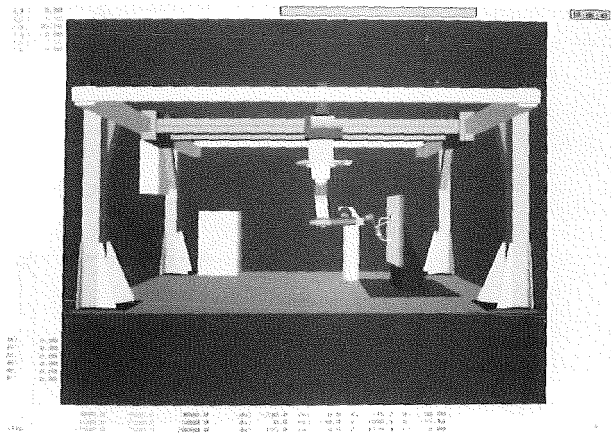


Fig. 72: KISMET display of CATROB experimental setup

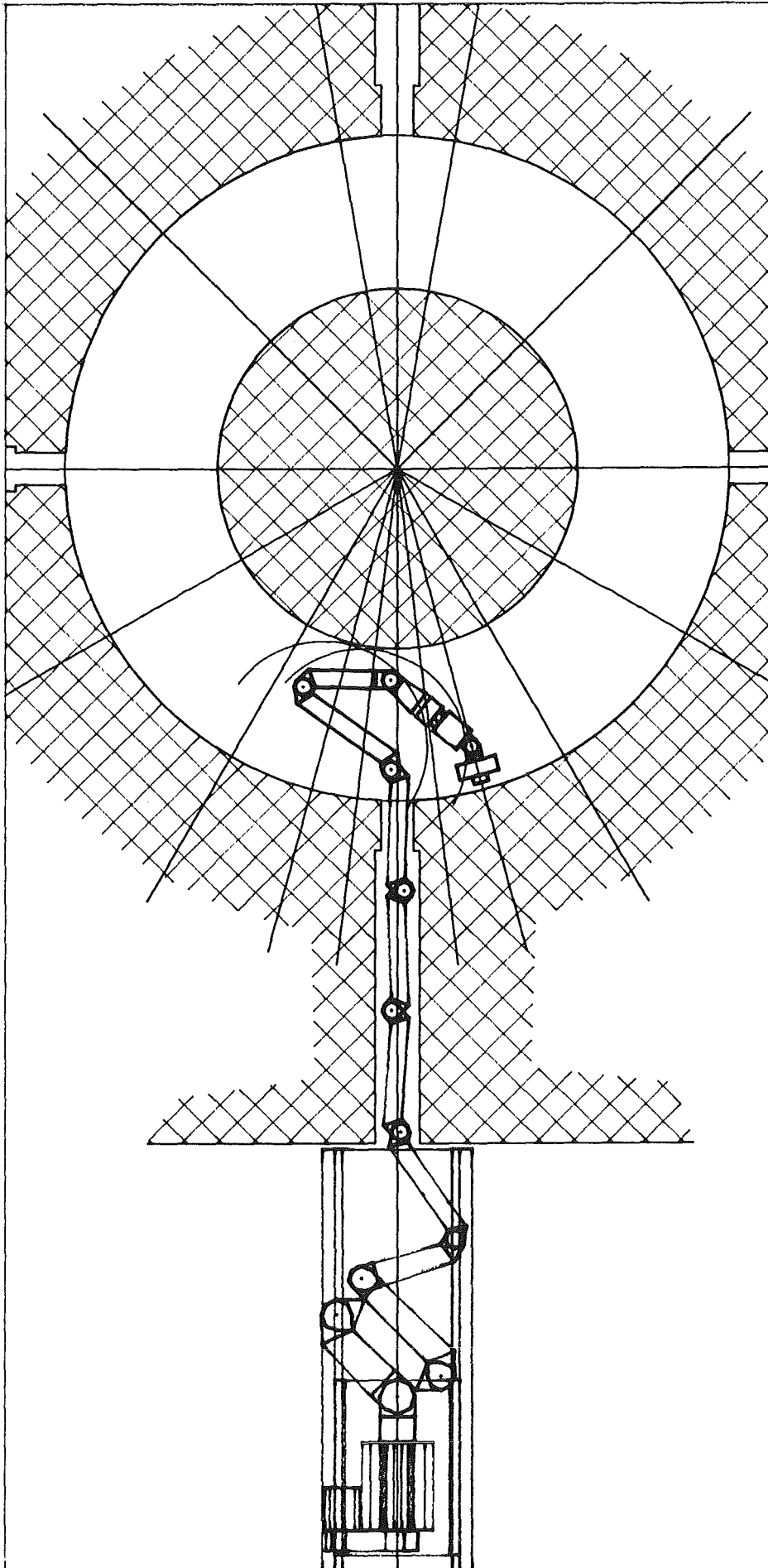


Fig. 73: Investigation of work positions

Staff:

H. Breitwieser

E. Holler

J. Hübener

H. Knüppel

B. Köhler

G.W. Köhler

I. Kornelson

R. Krieg

U. Kühnapfel

K. Leinemann

W. Link

A. Ludwig

J. Reim

W. Pleschounig

H.A. Rohrbacher

E.G. Schlechtendahl

A. Suppan

Fr. E. Wehner

References:

- [1] Suppan, A., Hübener, J.: Investigations of In-Vessel Handling Concepts for NET, IAEA Technical Committee Meeting on Robotics and Remote Maintenance Concepts for Fusion Machines, Karlsruhe, 22.-24.2. 1988
- [2] Suppan, A., Hübener, J.: In-Vessel Handling Unit Concept for NET, 15th SOFT, 19.-23. September 1988, Utrecht
- [3] Köhler, B.: GMS - a high-precision Geometry Measurement System for large fusion reactor components, IAEA Technical Committee Meeting on Robotics and Remote Maintenance Concepts for Fusion Machines, Karlsruhe, 22.-24.2. 1988
- [4] Benner, J., Leinemann, K., Stratmanns, E., Till W., Walz, C.: Automation of Remote Maintenance for Fusion Machines. 15th SOFT, 19.-23. September 1988, Utrecht
- [5] Leinemann, K., Kühnapfel, U., Ludwig, A.: CAD-Model Based Remote Handling Control System for NET and JET. 15th SOFT, 19.-23. September 1988, Utrecht
- [6] Suppan, A. (ed.): KfK proposal for Component testing. Unpublished Report of KfK, June 21st, 1988.

S + E 4.1.2 Safety Aspects of the Cryosystem

Under this task safety aspects of the cryostat of NET are investigated. The cryostat surrounds the toroidal plasma vessel and all superconducting coils as well. It has to maintain high vacuum conditions. The cryostat vessel considered here is a thin shell structure under outer pressure loading. To guarantee the integrity of this vessel its complicated buckling behaviour has to be studied for normal and accident conditions.

In order to facilitate this investigation a simplified strategy [1] to calculate the buckling loads has been developed. To assess the calculational results buckling experiments are performed as well. Fig. 74 shows a comparison of experimental [2] and calculational results for a cylindrical shell (diameter 255 mm, height 350 mm, wall thickness 0,4 mm) with geometric imperfections due to fabrication (max. radial deviation 0.2 mm). Due to the imperfections of the

cylinder geometry the deformations show a typical limit point behaviour with some deformations in the buckling mode before the critical pressure load is reached.

The comparison of Fig. 74a and 74b demonstrates that the mode and its circumferential position are calculated very well by the simplified strategy. The deviation of the calculated failure pressure from the measured one is within a reasonable band width of 20 %. An important result is that not the maximum imperfection but only the buckling mode fraction of the imperfection controls the behaviour. In the above example the latter is about 5 % of the wall thickness whereas the maximal imperfection is about 50 %.

The experimental investigations of cylindrical shells under outer pressure load have been continued. Fig. 75 shows the ideal, the initial imperfect and the buckled surface of a cylinder with two quadratic cutouts. This cutouts are intended to simulate the effect of the cryostat ports on the buckling behaviour. During the experiment the cutouts have been sealed by a soft vulcanized sheet of rubber supported by an inner mandrel. The buckled surface shows, that the cutouts lead to local concentrations of the buckles. This experimental investigations are going on.

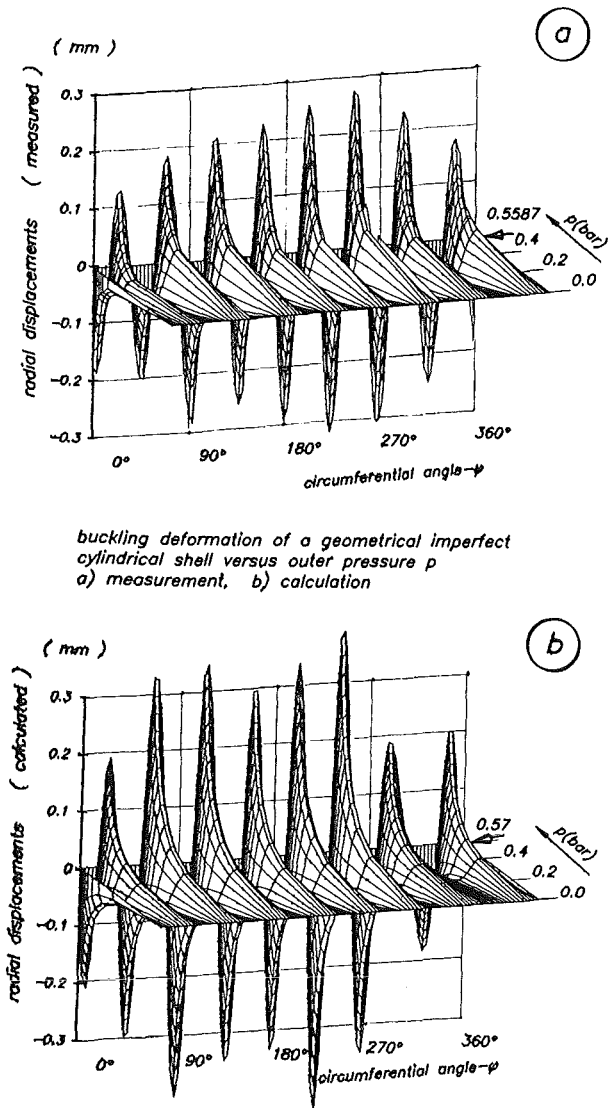


Fig. 74: Buckling deformation of a geometrical imperfect cylindrical shell versus outer pressure p
a) measurement b) calculation

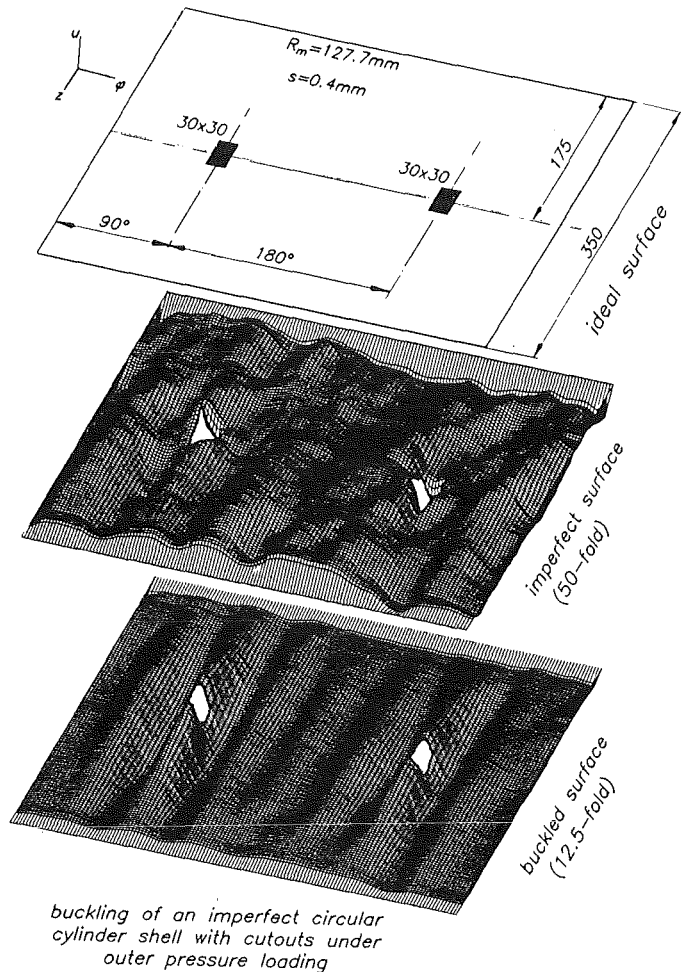
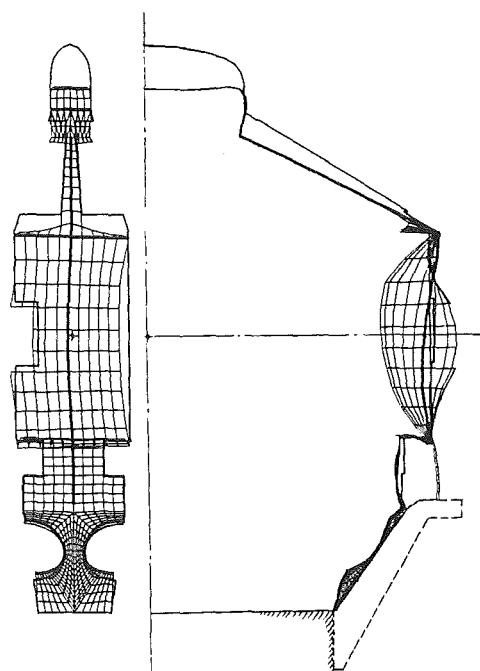


Fig. 75: Buckling of an imperfect circular cylinder shell with cutouts under outer pressure loading

First results of the NET cryostat buckling behaviour have been produced using the simplified strategy. Fig. 76 shows the buckling form of a cryostat section (1/16) of the NET-2-2a cryostat reference design. The windows in the cylindrical part of the vessel proved to have some importance on the buckling behaviour. Further calculations will be done using increased sections in order to find out whether lower circumferential deformation modes may cause a lower buckling pressure.

Staff:

B. Dolensky
R. Krieg
T. Malmberg
S. Raff
E. Wolf



*buckling shape of a cryostat segment
NET-2-2a (displacement scale 500)*

Fig. 76: Buckling shape of a cryostat segment (NET-2-2a)
(displacement scale 500)

References:

- [1] S. Raff, B. Dolensky, R. Krieg 'A simplified procedure for elastic buckling analysis'.
Transactions of the 9th SMIRT, Vol. B, p. 569-574,
Balkema Rotterdam, Boston 1987
- [2] Nuclear Fusion Project, Semi-Annual Report of the
Association KfK/EURATOM, October 1987 - March 1988,
p. 61

S + E 4.1.3 Safety Aspects of Superconducting Magnets

During operation of superconducting magnet systems disturbances are conceivable which could finally result in the destruction of a magnet. The energy discharged thereby into an electric arc may lead to damage of the surroundings of the magnet. Cause and course of the disturbances, their detection and identification as well as their possibly destructive consequences are to be investigated using the superconducting torus arrangement TESPE-S. Through development of codes and their verification on the TESPE-S experiment an attempt will be made to transform the results to other larger magnet systems.

The investigations of arcs supplied by the magnets' energy were continued concentrating on the interaction between arc and magnet and especially also on arcing under spatial restrictions like in magnet windings.

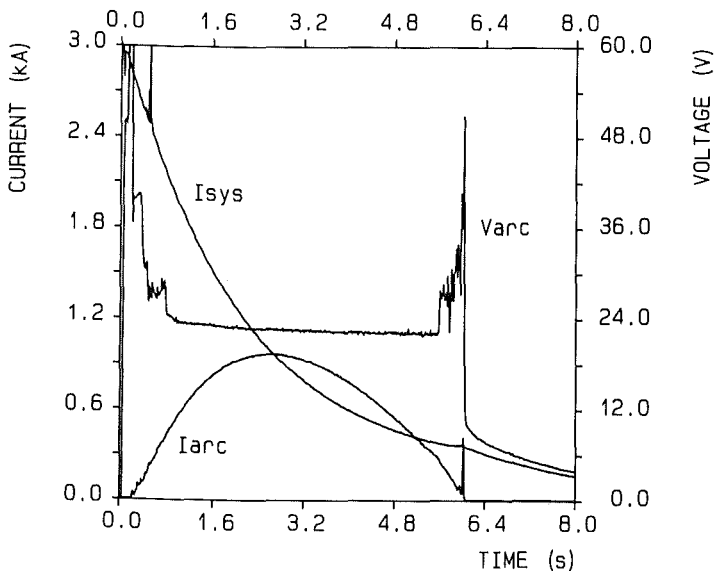


Fig. 77: Curves of system current I_{sys} , arc current I_{arc} and arc voltage V_{arc} for an arc across one coil initiated by high voltage pulse.

Initiating an arc across one coil (out of six TESPE coils) during a regular fast discharge results in arc characteristics like shown in Fig. 77 (see also Fig. 71 of previous report). The arc was burning here in a large chamber at low pressure (40 mbar). For these conditions the voltage is about constant and typical in the range of 22 V. The behaviour of the arc current can be explained by occurrence of a superposition of two processes: On the one hand the arc acts as a short-circuit and the system couples energy into the arcing coil up to a maximum determined by the magnets' coupling coefficient and the resistance of the "short", on the other hand the arc continuously consumes energy leading to a decrease of the arc current. The behaviour of the system current reflects simultaneous energy deposition in the discharge dump resistor and in the arcing coil.

Arcing across the total magnet system gives characteristics with different shape. Here is no inductive coupling, but the arc burns in parallel to the dump resistor; the current distribution and therefore the discharge time constant is determined by the arc voltage. In the example of Fig. 78 an arc is burning within a confining chamber across the system. The observable higher voltage level is due to increase of pressure. Maximum pressures obtained up to now are near 30 bar corresponding to a maximum voltage of 200 V. Few additional experiments are being prepared with chambers simulating forced flow windings still closer.

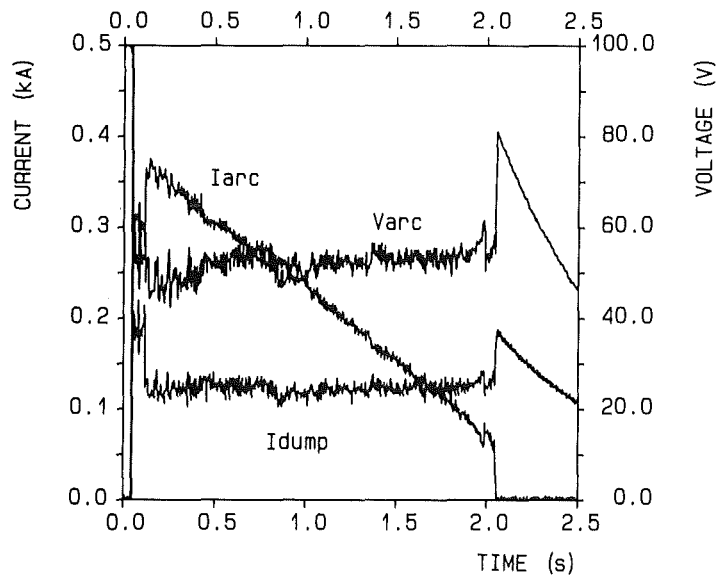


Fig. 78: Currents and voltage for an arc across the total magnet system in parallel to the dump resistor.

Measures for extinguishment of arcs are effective, if the voltage supplied to the arc can be managed to be reduced below the burning voltage, e.g. by short-circuiting the arc. In contrast, a deliberate stop of system discharge does not extinguish the arc which continues distracting energy from the magnets.

For calculations of the behaviour of a magnet system with an arc the program MSCAP was successfully applied, if the arc voltage characteristic was taken from experiments. As it seems impossible to calculate the arc voltage itself, typical experimental data will have to be taken also for future assessments.

The non-destructive magnet safety experiments within the TESPE-S program are about being finished. A final evaluation phase is going on. The former planned magnet destruction experiments were re-considered; as a result further planning concentrates on forced flow test windings, because the experience gained up to now showed that arcing in helium transparent windings will pose problems of interpretation of obtainable results due to the observed mobility of arcs. Program tasks are under consideration together with the NET Team.

Further it is planned to include experimental and theoretical magnet safety investigations in future magnet test arrangements of the institute (POLO, TOSKA-UP).

In addition to the safety experiments, the reliability analyses of magnet system components were continued. The reliability analysis of the switch down mechanism for the EURATOM-LCT superconducting magnet in case of a quench was terminated. A more detailed analysis of the failure data confirmed the preliminary assumptions. The result is an overall unavailability per demand of $3 \cdot 10^{-2}$ for the switch down function. This is based on a failure rate of the logic controller of $1 \cdot 10^{-5}$ /h by consideration of the Common Mode failure influence. The part of the logic-controller on the overall unavailability is 97,5%. An elimination of the Common Mode influence would lower the results only by the factor of 3.

In view of the demand for a larger reliability of safety related prevention measures for larger facilities it is felt necessary to introduce additional measures. This seems feasible and practicable by use of more redundancy and diversity. An additional hardware system, solely for the switch down function in redundancy, would tolerate the unavailability of the logic controller, which then could be used mainly for operating and control tasks.

Reference:

K.P. Jüngst, H. Kronhardt, M. Oehmann, J.S. Herring: 'Arcing Experiments of Magnet Safety Investigations.', 15th Symposium on Fusion Technology (SOFT), Utrecht, 19-23 September 1988

Staff:

P. Duelli
J.S. Herring
K.P. Jüngst
H. Kiesel
H. Kronhardt
G. Obermaier
M. Oehmann
H. Schnauder
J. Seibert
E. Süß
A. Wickenhäuser
H. Yanagi

S + E 5.4 Overall Plant Accident Scenarios for NET

Besides the system related safety studies performed under the topics S + E 4 this work concentrates on the interactions of the different systems and the integral behaviour of the plant.

The procedure is that for the main systems severe accidents are postulated. Then the consequences are studied roughly. The question in these studies is, whether the initiating failure will cause also consequences in other systems.

Under the heading of identification of accident sequences based on engineering judgement in the period reported

here two additional reference accident sequences were identified:

- severe failure in detritiation system
- LOCA outside vacuum vessel.

In the next step for the RAS's identified so far clear initial and boundary conditions will be proposed. For the failure at the TF coils this is: growing normal conducting zone and complete failure of the external discharge system. For the leak into the vacuum vessel it is 2F-LOCA of a divertor tube.

These proposals will then be discussed with the designers.

Staff:

R. Meyder

S + E 5.5 Development of Safety Guidelines for the Design of NET

The task being performed in the framework of a special working group aims at ensuring advice to NET on safety and environmental guidelines. The group members belong to the following associations: CEA/IPSN, ECN-Petten, JRC-Ispra, KfK-Karlsruhe, Riso National Laboratory, The NET Team and UKAEA/SRD.

In summer 1988 three working documents in the frame of Safety Related Recommendations for the Design of NET were elaborated and edited by the group. These are

Part 1: Radiological Safety Related Recommendations, and two Special Issues, one on External Hazards and the other one on Fires.

Furthermore, a first draft of a special issue on Protection against Magnetic and Radiofrequency Electromagnetic Fields was compiled by KfK.

For the time being discussions are going on how to proceed with the future work of the group, especially concerning specific safety related recommendations for the design of the different systems.

Staff:

W. Kramer

**S + E 7 Generic Environmental Impact
Assessment for a Fusion Facility**

The assessment of the radiological consequences of tritium accidentally released to the atmosphere requires the dynamic modelling of the behaviour of the various chemical forms during dispersion and deposition, in the food-chains and finally in the human body. After the implementation of the compartment model COMA and its application to foodchain modelling in example calculations for leafy vegetables during the preceding period of work, emphasis has been laid on the modification of the trajectory model MUSEMET to allow for the chemical transformation HT→HTO during dispersion, the deposition of HT and HTO, and the reemission of HTO after deposition on ground and plant surfaces. The dispersion of HTO after reemission is modelled by a multi-source approximation. First results

show a significant contribution of the inhalation pathway to the collective dose even in the case of HT releases.

In a next step, the atmospheric dispersion model for tritium will be coupled to the foodchain model by a special soil/plant-atmosphere interface. After its completion, the whole environmental tritium model will be implemented as a submodule into the program system UFOMOD for assessing the radiological consequences of nuclear accidents.

Staff:

J. Ehrhardt

W. Raskob (DTI)

T 6 Industrial Development of Large Components for Plasma Exhaust Pumping

On behalf of the Commission of the European Communities (CEC) a working group of CEA and KfK staff members are elaborating the specifications and are conducting development work for large vacuum components for NET. Two alternative solutions for plasma exhaust gas pumping are being pursued in parallel: mechanical pumps and cryopumps. The large components required (high vacuum pumps, forepumps, and valves) are not commercially available at present. It is planned to develop them within T6.

Turbomolecular Pumps

The feasibility study for a 50.000 l/s turbomolecular pump satisfying the requirements laid down in our technical specification has been completed. The final report has been prepared.

Evidence has been provided in the study that with a single flow pump, which includes 17 compression stages, a helium pumping speed of 50.000 l/s can be attained. All requirements specified for NET operation have been fulfilled, except for the helium throughput for pumping out during the dwell time. A maximum throughput of 165 mbar/l/s was specified for helium at 4×10^{-3} mbar intake pressure. In the worst case, a throughput of 115 mbar/l/s has been achieved at 4×10^{-3} mbar intake pressure and 3×10^{-1} mbar outlet pressure. This "worst case" value is based on data measured with previously built pumps of smaller sizes and it has been derived with a recently developed computational method of extrapolation. It has been proposed to verify the computed results by experiments on true scale with a reduced number of compression stages. Also at the reduced throughput the envisaged pumping out times have been attained for a given dwell time (20 s).

The sole reason for the relatively high number of compression stages (17) required is that the requested

compression ratio for H_2 of 5×10^6 must be attained. All the rest of requirements can be satisfied with a reduced number of stages as well. An alternative pump concept relying on 12 compression stages has been proposed by which a compression ratio of 5×10^4 is attained. With this type of pump the requested total base pressure in the torus of 10^{-8} mbar, which is required only in the cleanup mode, can be achieved in two ways:

- by connecting an additional small turbomolecular pump (~ 2000 l/s);
- by use of a forepump with the intake pressure reduced from 10^{-2} to 10^{-4} mbar. There are good prospects that oil free forepumps of the moving spiral type are able to attain the requested inlet pressure.

Gate Valves

Starting from a search into the literature published on and patents granted for the technical solutions available for sealings and drives of all-metal valves and relying on experience gathered by the VAT company, a technical concept has been elaborated for the NET vacuum gate valve. The VATRING system with double sealing rings on a bottom plate was selected for sealing. The valve seats on both sides are pressed to the bottom plate via pneumatically operated bellows drives. The bottom plate is moved by a pendulum drive. For 2 bar differential pressure at the valve the bottom plate must resist an axial force of $\sim 4 \times 10^5$ N. The strength of the critical components of the gate valve was examined and optimized using the finite element method.

Prototype Testing

Work on preparing the technical specification for the prototype testing facility was continued.

Staff:

M. Lieberknecht

A. Mack

D. Perinić

T 7 Optimization of Cryogenic Vacuum Pumping of Helium

The objective of experimental investigations into helium and plasma exhaust cryopumping consists in comparing and assessing in a test series performed on a reduced scale the multitude of possible technical alternatives of helium cryopumping with the aim to achieve design data and operation requirements for the compound cryopumps to be used in the torus vacuum system of a fusion machine.

The best suited technical solutions will be optimized under simulated NET operating conditions. The result of the investigations will be a specification of the active cryopumping surface for the NET plasma exhaust.

Characterization of Adsorbers

It is planned to record at 4.2 K helium adsorption isotherms of selected adsorption samples and evaluate them in order to be able to characterize the sorbent materials for helium cryosorption. Since, as far as we know, this type of measurement has not been performed until now, we have charged the Technical University of Erlangen to carry out at the porosimeter available there comparative measurements of the nitrogen and helium isotherms of a sample provided, with the objective to examine whether the measurements at 4.2 K are feasible.

A pore size analyzer supplied by Omicron Technology Corporation was available for the measurements. With this equipment adsorption isotherms can be measured on a routine basis with nitrogen as the testing gas at $T = 77\text{ K}$. Several modifications had to be made in order to be able to record a helium adsorption isotherm. Besides, the specific material data of the respective adsorbant-adsorbate combinations were incorporated in the evaluation algorithm used to be able to evaluate the measured data of the helium isotherms.

The specific surface was calculated using the BET theory /1/ and the micropore distribution was calculated according to Horvath-Kawazoe /2/.

The adsorption isotherms shown in Fig. 79 were obtained for the amounts investigated of molecular sieves ($m = 0.0689\text{ g}$ at $T = 77\text{ K}$; $m = 0.089\text{ g}$ at $T = 4.2\text{ K}$). Both measurements yielded a type I isotherm. This means that the sorbent material at low relative pressure adsorbs the amount of gas metered in until saturation occurs. According to the theory proposed by Dubinin the submicropores and micropores, respectively, are spontaneously filled at these low relative pressures. As can be clearly seen, the micropores are filled both more intensively and more quickly during the measurement with helium. For example, a volume of $120\text{ ml}_{\text{NTP}}/\text{g}$ of nitrogen was adsorbed on the sample before saturation, whereas the corresponding amount of helium was $160\text{ ml}_{\text{NTP}}/\text{g}$. This result suggests that a rather high number of submicropores previously inaccessible to N_2 particles can now be filled with the helium atoms.

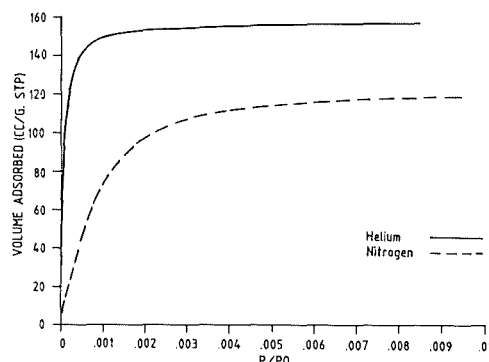


Fig. 79: Detail from the Adsorption Isotherms

The specific surface calculated with the BET theory in both measurements attains a value higher by 10 % in the experiment involving nitrogen (N_2 : $574\text{ m}^2/\text{g}$; He: $516\text{ m}^2/\text{g}$ for $10^{-4} < p[\text{mbar}] < 10^{-2}$).

Reasons for the deviations of the results obtained under the BET theory from the overall result of the investigations might be that different regression limits have been used in the determination of the monomolecular adsorbate layer and that, possibly, errors have been made in weighing.

The micropore distribution calculated according to the theory of Horvath and Kawazoe has been represented in Fig. 80. In the measurement with helium a shift can be observed of the maximum of distribution towards smaller pore sizes and an increase in volume can be detected for the magnitude of small pores. This means that more helium as the adsorbate fills the smaller pores than would be achievable with nitrogen. This result is confirmed by the evaluation relying on the t-plot theory according to De Boer. For the micropore volumes the values $V_{\text{micro, He}} = 0.232\text{ ml/g}$ and $V_{\text{micro, N}} = 0.174\text{ ml/g}$ were calculated.

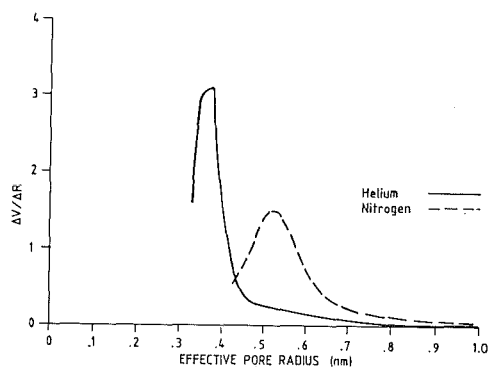


Fig 80: Pore size distribution (Derivative of adsorbed volume versus pore radius)

A measuring equipment of the same type was procured for KfK. Acceptance testing of the equipment has been under way since July 1988.

Measurements of the Croyrsorption Capacity for Helium

The calibration measurements at the HELENE facility have been completed. The measurements are very well reproducible. With the immersion device without adsorber sample a maximum pressure deviation of ± 0.04 mbar was measured after degassing in vacuum at 300 °C, cooling down to 4.2 K, helium flooding to 500 mbar, pressure reduction to 10^{-2} mbar, followed by heating up to 300 K in three experiments. A molecular sieve sample (50 mm in diameter on a copper substrate with approximately 2.8 g of adsorber material in two experiments adsorbed 149 and 154 mbar/g helium, respectively. Converted to the surface of the metal plate of $D = 48$ mm inside diameter, this gives an adsorption capacity for helium of 23.2 and 23.9 mbar/cm², respectively.

TITAN Testing Facility

The TITAN testing facility is still under construction.

References:

- /1/ Brunauer, S., Emmett, P.H., Teller, E.:
Adsorption of Gases in Multimolecular Layers;
J. Am. Chem. Soc. 60, 309, (1938)
- /2/ Horváth, G., Kawazoe, K.:
A Method for the Calculation of the Effective Pore Size
Distribution in Molecular Sieve Carbons;
J. Chem. Eng. Jap. 16, No. 6, 470 (1983)

Staff:

H. Haas

J. Hanauer

W. Höhn

B. Kammerer

U. Kirchhof

H. Lukitsch

A. Mack

D. Perinić

D. Zimmerlin

T 10 A Plasma Exhaust Purification by Means of Cryosorption on Molecular Sieves or Alternative Adsorbents

The fuel cycle of a fusion reactor requires simple processes for the removal of impurities from gaseous streams such as the plasma exhaust gas, the solid blanket coolant, the blanket purge gas, etc. One such process is cryoadsorption on molecular sieves or activated charcoal. To evaluate this alternative information is needed on the adsorption of mixtures of typical fusion fuel cycle impurities like hydrocarbons, ammonia, carbon dioxide, carbon monoxide and water from a helium or a hydrogen carrier gas. One aspect of particular concern is the cosorption of hydrogen with other impurities.

For this investigation a UHV tight, tritium compatible cryostat has been planned and commissioned (see Fig. 81).

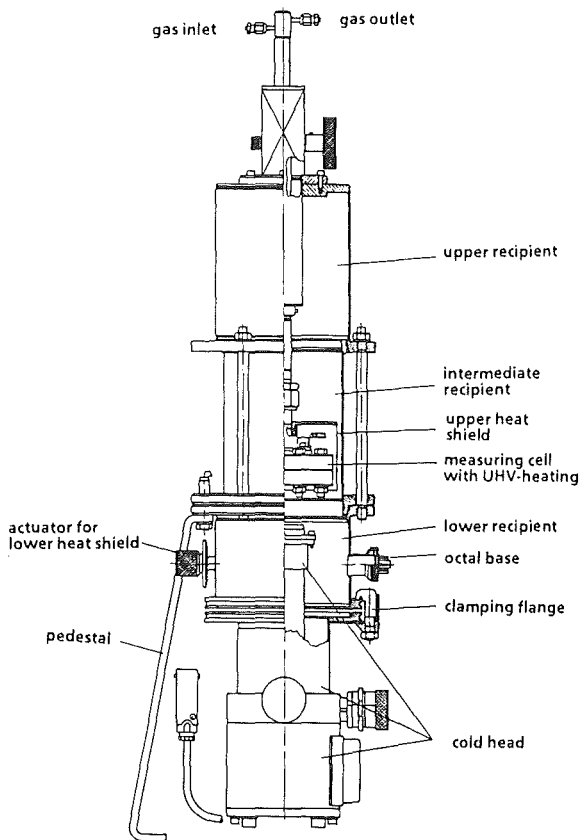


Fig. 81: Cryostat for adsorption studies

Numerous modifications required to adapt the cryostat for the operation in an existing and now decontaminated glove box have delayed the delivery, which is now expected for Nov. 88.

Meanwhile work on the development of gas chromatographic analytics of hydrogen isotopes with a liquid nitrogen cooled GC column, placed outside the HP 5880 gas chromatograph, has continued. The carrier gas Ne

needs to be carefully purified to avoid plugging of the GC column, which is made of iron oxide on alumina. Presently a good separation of hydrogen isotopes is accomplished in about 50 min. Another very sensitive technique for the determination of HT and HTO consists of a series of bubblers containing ethylene glycol placed before and after a copper oxide catalyst bed. Tritium collected in the bubblers is analysed by standard liquid scintillation counting. In addition, total tritium in the gas phase can be measured with a calibrated small volume ionization chamber.

Adsorption/desorption of water on molecular sieve 5A was studied in a flow system employing either helium containing 5000-7000 ppm H₂O or very dry helium. The water content of the carrier gas was regulated with a cold trap. The amount of adsorbed water was obtained from breakthrough curves. Satisfactory agreement between the estimated water adsorption and that determined from desorption curves or from thermogravimetry was obtained. For complete removal of adsorbed water the molecular sieve was slowly heated up to 450°C. As verified by X-ray diffraction and measurements of the specific BET surface area no destruction of the crystalline framework took place under these conditions.

Type A zeolites have an aluminosilicate framework composed of sodalite or β units stacked in a cubic array, thus forming a large cavity, the α cage, between every 8 sodalite units. Therefore type A zeolites may act as a double sieve: the channel system of the large cavities interconnected in all three dimensions, and a second sieve effect given by the passage from the large cavities into the small β cages through six membered rings of 0.25 nm free aperture. Only small molecules such as H₂O and NH₃ can penetrate into the small sodalite units. When a completely dried type A zeolite is exposed to a humid atmosphere the small β cavities are loaded first. First experimental results with tritiated water suggest that tritium exchange between the α cavities and the β cavities takes place predominantly at temperatures about 200°C in competition with water desorption.

Staff:

- K. Günther
- H.E. Noppel
- R.D. Penzhorn
- M. Tank

T 10 C Plasma Exhaust Gas Purification by Use of Hot Getter Materials

Objectives

Main objective is the investigation of the applicability of getter materials for gas purification processes in tritium technology. Getters can be used to recover chemically bound hydrogen isotopes by decomposition of hydrocarbons and water and to remove impurities like N_2 , CO , and CO_2 from a helium carrier gas. An important application of getter reactions can be seen, therefore, in the removal of residual impurities from process effluent gases and in the tritium recovery from tritiated gas species.

The main program steps are:

- A. Inactive tests on various getter metals and alloys (e.g. Zr-Al, Zr-Fe-V) to investigate sorption speeds, retention capacities, and cracking capabilities of impurities as a function of temperature, flow rate, and presorption.
- B. Active tests with tritium and tritiated compounds to study the influence of β -radioactivity on the kinetics of the gettering and cracking processes.

Current Progress

After first operational tests with the PEGASUS facility, several technical changes were carried out to improve the overall leak tightness, the pumping efficiency, and the pressure control of separate sections of the facility. As a result, a leak rate of less than 10^{-7} mbar·l/s has been attained for the manifold and of less than 10^{-6} mbar·l/s for the gas loop. A tightness in these ranges is required in order

- a) to reduce the impurity concentration to a level in the 1 ppm range by passing the gas several times through the getters (recirculation mode). Depending on the experimental parameters a few hours may be required to reach the desired purity. During that time no additional impurities should be introduced by leakages because these would not only increase the getter consumption and retard the purification process but would also limit the achievable purity level of the test gas.
- b) In the phase B tests with trace amounts of tritium a good tightness is needed for safety reasons.

The facility has been further completed by a gas chromatographic workstation which is operated with a BASELINE 810 System of Dynamics Solution (Millipore) for acquisition, calibration, evaluation, and storage of GC data. Preparations for phase B tests were continued by installation of two uranium beds, and a additional gas collection tank, and a heat removal system for the glove box atmosphere

Parallel to these technical efforts, some basic studies have been carried out on the cracking of ammonia and methane by nickel and titanium. The results of these screening tests, which were also used as preliminary tests for the loop design and for the analytics, can be summarized as follows:

- a) The cracking of ammonia by nickel is a first order reaction with a rate constant of $k = 8.8 \cdot 10^{-5} \text{ s}^{-1} \text{ m}^{-2}$ at 590°C . Under the conditions described in Fig. 82 the cracking was complete within less than 100 min.

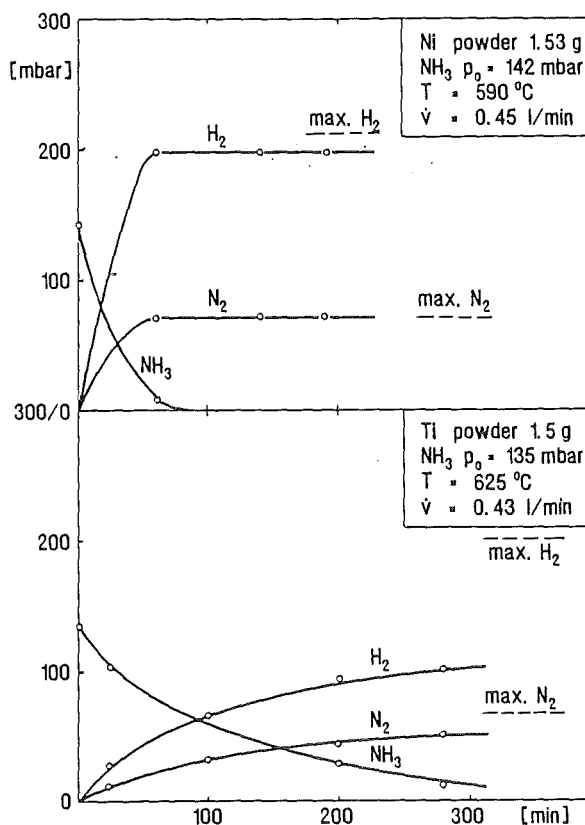


Fig. 82: Decomposition of NH_3 by Nickel and Titanium

- c) Titanium powder was much less reactive than nickel powder. A significant fraction of the ammonia reacted with titanium to form an overlayer of the composition $TiNi_{0.6}$; in addition, about 50% of the hydrogen produced via cracking yielded titanium hydride.
- d) Methane could not be cracked quantitatively by titanium powder at temperatures $\leq 925^\circ\text{C}$. A post-test X-ray diffraction spectrum of the Ti powder revealed the presence of TiC which might have been responsible for the incomplete cracking.

Plans for the Near Future

- Continue operational tests of three SAES and one HWT getter bed by determining H_2 absorption/desorption characteristics.

- Start measurements on the gettering and cracking properties of these getters with CH₄.
- Investigate the heterogeneous decomposition of water.
- Continue installation of devices for tritium tracer experiments.

Staff:

H. Albrecht

T. Kastner

U. Kuhnes

K. Schuster

T 10 E Absorption of DT on Heated Metal Beds other than Uranium

One new promising candidate material for the interim storage of tritium gas is ZrCo alloy. The average hydride composition attained at room temperature with 0.1 MPa H₂ was found to be ZrCoH₃.

Loading and deloading isotherms of hydrogen and deuterium in ZrCo were measured in the temperature range 200-300°C employing standard volumetric techniques (see Fig. 83). The deloading curves show the hysteresis characteristic to the ZrCo/hydrogen system (see Fig. 84). At 300°C the mean hysteresis factor in the plateau region (0.8 > x > 1.5, ZrCoH_x) was found to be 0.62 and 0.74 for H₂ and D₂ respectively.

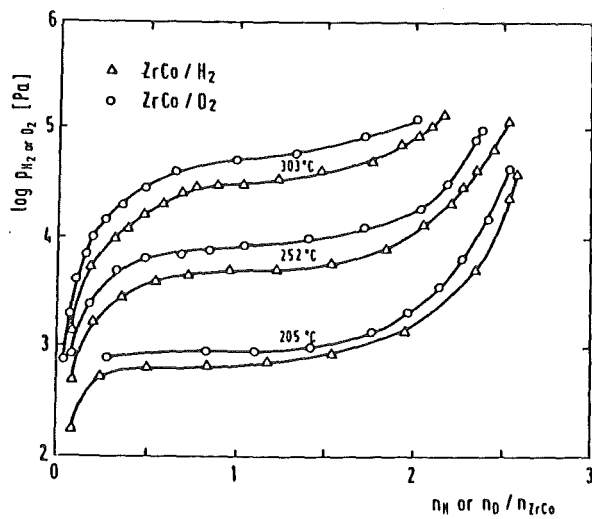


Fig. 83: Pressure composition isotherms for H₂ and D₂ absorption by ZrCo alloy powder

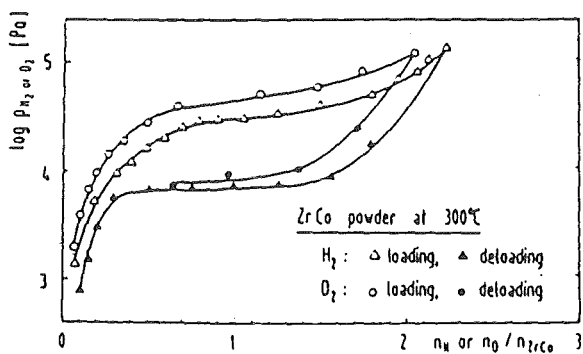


Fig. 84: Hysteresis of the ZrCo/H₂ and ZrCo/D₂ systems at 300°C

The temperature dependance of the equilibrium pressure of a given gas/metal ratio in the plateau region is described by the well known equation

$$\log P_{H_2}(\text{or } D_2) = -A/T + B$$

which can be compared with the integrated van't Hoff equation

$$\log P/\text{bar} = H/RT - S/R$$

in which H and S are the apparent molar enthalpy and entropy for H₂ (or D₂) absorption in the plateau region and R the gas constant.. The mean values of the van't Hoff parameters A and B as well as the corresponding thermodynamic data calculated from the plateau results given in Fig. 83 are listed in Table 6.

gas	A (1)	B (1)	-ΔH(2) kJ/mol	-ΔS(2) kJ/mol
H ₂	4689 ± 34	12.73 ± 0.20	89.8 ± 0.7	148.0 ± 2.3
D ₂	5012 ± 121	13.53 ± 0.34	95.9 ± 2.3	163.0 ± 7.0

Table 6: Van't Hoff parameters and thermodynamic functions for the absorption of H₂ or D₂ by ZrCo alloy in the plateau region 0.8 ≤ x ≤ 2.0.
(1) According the eqn. (1) with P in Pa and T in K.
(2) Expressed per mol H₂ or D₂.

At least 99.95 % of the hydrogen present in ZrCoH₃ can be recovered by pumping on the hydride at 450°C. Irreversible trapping of hydrogen was quantified with tritium labelled gas. For this purpose a ZrCo sample loaded with tritiated hydrogen up to saturation was deloaded at 450°C and then dissolved in hydrochloric acid. The permanently trapped hydrogen was estimated by liquid scintillation counting. The results indicate that under these conditions less than 10⁻³ mol H/mol ZrCo remain trapped in the getter.

To study the effect of nitridation and carburization on the gettering properties of ZrCo activated samples were exposed to N₂ and to CH₄ for various periods of time. The hydrogen absorption isotherms at 200, 250 and 300°C of the nitridized and carburized samples were then compared with those of the original ZrCo (see Table 7). From the results it is apparent that neither partial nitridation nor carburization have a pronounced effect on the values of the thermodynamic properties. This suggests that the binding of hydrogen to ZrCo is essentially not altered by the contaminants N and C.

Staff:

- M. Devillers
- R.D. Penzhorn
- M. Sirch
- E. Willin

Sample	A (1)	B (1)	-ΔH(2) kJ/mol	-ΔS(2) kJ/mol K
ZrCo (JAERI)(3)	4751	12.74	91.0	148
ZrCo (SAES)	4636	12.49	88.8	143
ZrCo /3/	4408	12.04	84.4	135
ZrCoC _{0.06} (JAERI) (3) /4/	4330	12.05	82.9	135
ZrCoN _{0.06} (SAES)	4464	12.26	85.5	139
ZrCoN _{0.23} (SAES)	4422	12.32	84.7	140

Table 7: Van't Hoff parameters and thermodynamic functions for the absorption of H₂ by pure ZrCo alloy and alloy exposed to nitrogen (550°C) or methane (304°C).

(1), (2) same as in Table ..., (3) Sample kindly supplied by S Konishi, Tokai-mura, JAERI

T 10 H Catalyst Development for the Exhaust Purification Process

For the plasma exhaust reprocessing of NET during the different operation periods burn and dwell, bakeout, etc. a process concept is proposed, which combines catalytic decomposition of tritiated impurities with hydrogen isotope separation/purification by palladium silver permeators. Removal of the main deuterium/tritium stream occurs by an array of Pd/Ag tubes. Tritium/deuterium chemically bonded in species such as hydrocarbons, ammonia and water is liberated via catalytic reactions on a nickel catalyst as well as on a zinc-stabilized copper chromite catalyst and recovered with the help of a second permeator.

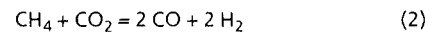
While in the past the experimental effort concentrated on the study of single component reactions, in this work gas mixtures simulating the plasma exhaust gas composition were examined. In particular, the decomposition of methane on a nickel catalyst was investigated in the presence of carbon dioxide (typically at the same initial partial pressure as methane) and water. The gaseous mixture was circulated over the catalyst held at approx. 530°C while continuously removing the produced hydrogen with three commercial Pd/Ag permeators arranged in series. The flow rates were set to about 10 l/min to achieve conditions of an ideal batch reactor, which facilitates the acquisition and interpretation of the results. Gas analysis was performed by gas chromatography and volumetric techniques. In addition, two hygrometers (0-400 and 100-10000 ppm) were integrated in the loop to enable continuous detection of water partial pressures during the course of the experiments.

The most important conclusions can be summarized as follows:

- i) The presence of high partial pressures of carbon dioxide has no effect on the thermodynamic equilibrium of the methane cracking reaction and, within the experimental error, does not influence the rate of the methane decomposition. Preliminary experiments with methane/carbon monoxide mixtures show that carbon monoxide also behaves indifferent with respect to the cracking of methane. Thus, the catalytic recovery of bonded hydrogen isotopes from hydrocarbons requires no preadjustment of the chemical composition of the gas to be processed.
- ii) In a former investigation it was shown that carbon deposited on the nickel catalyst from the decomposition of hydrocarbons can be gasified by reaction with hydrogen (yielding methane), thus allowing a regeneration of the catalyst. Numerous experiments carried out both in a closed loop and in a flow apparatus have demonstrated that the gasification of the carbon deposit can also be accomplished via the Boudouard reaction

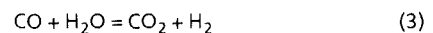


by passing carbon dioxide over the "exhausted" catalyst. This regeneration method has important advantages over the gasification with hydrogen, i.e. the product of the reaction contains no hydrogen (tritium) and can therefore be stacked via the waste detritiation system. Interestingly, when methane is cracked in the presence of carbon dioxide the Boudouard equilibrium simultaneously participates in the reaction mechanism. It follows that the life time of the catalyst is prolonged as the ratio of the carbon dioxide/methane concentration is increased. The overall reaction is then described by



and is truly catalytic.

- iii) If in addition to carbon dioxide and methane water is present in the gaseous mixture, CO produced in reaction (2) is partly consumed by the water gas shift reaction



which also takes place on the nickel catalyst. Even though from thermodynamic considerations it can be shown that the temperature at which methane is decomposed does not favour reaction (3), water can be completely decomposed provided hydrogen is continuously removed with a Pd/Ag permeator. As a result all of the bonded and non bonded hydrogen (tritium) can be extracted from the loop.

Previous studies on the influence of impurities on the permeation rate of hydrogen through a commercial Pd/Ag permeator were continued employing ammonia and methane at partial pressures generally much higher than expected in the plasma exhaust. The results, which have been compiled in Table 8, show that at least within short periods of time the permeation rates above 300°C are not significantly affected by the presence of the above mentioned impurities.

Staff:

K. Günther
M. Glugla
R.D. Penzhorn
R. Rodriguez
M. Tank

temperature	hydrogen concentration mol/l x 10 ²	impurity*	impurity concentration mol/l x 10 ³	permeation rate mol·cm/cm ² min kPa ^{1/2} x 10 ⁷
373	1.01	H ₂ O (2)	0.99	3.13
373	1.01	NH ₃	1.21	1.57
423	1.01	H ₂ O	0.99	2.92
423	1.01	NH ₃	1.21	2.52
473	1.01	- (3)	-	2.49
473	1.01	H ₂ O	0.20	2.54
473	1.01	H ₂ O	0.50	2.53
473	1.01	H ₂ O	0.99	2.52
473	1.01	CO	1.02	1.02
473	1.01	CO/H ₂ O	1.02/0.99	0.68
473	1.01	NH ₃	1.21	2.44
473	1.01	C ₂ H ₆	1.21	2.30
473	1.01	CO/H ₂ O/NH ₃	1.21/1.50/1.21	0.60
473	1.01	H ₂ O/CH ₄ /NH ₃	0.99/1.21/1.21	2.36
523	1.01	H ₂ O	0.99	2.46
523	1.01	CO	1.02	1.90
523	1.01	CO/H ₂ O	1.02/0.99	2.30
573	1.01	- (3)	-	2.51
573	1.01	H ₂ O	0.20	2.45
573	1.01	H ₂ O	0.50	1.64
573	1.01	H ₂ O	0.99	2.51
573	1.01	CO	1.02	2.53
573	1.01	CO/H ₂ O	1.02/0.99	2.41
573	1.01	NH ₃	1.21	2.45
573	1.01	C ₂ H ₆	1.21	2.46
623	1.01	CO	1.02	2.46
623	1.01	H ₂ O	0.99	2.49
673	1.01	- (2)	-	2.65
673	1.01	H ₂ O	0.20	2.78
673	1.01	H ₂ O	0.50	2.66
673	1.01	H ₂ O	0.99	2.68
673	1.01	CO	1.02	2.63
673	1.01	CO/H ₂ O	1.02/0.99	2.61
673	1.01	CO ₂	8.18	2.58
673	1.01	NH ₃	1.21	2.48
673	1.01	C ₂ H ₆	1.21	2.68
723	0.82	- (3)	-	3.29±0.16
723	0.82	CO (2)	0.82	3.05±0.19
723	0.82	CO (2)	4.09	2.89±0.02
723	0.82	CO (5)	8.18	2.85±0.14

* the number of averaged experiments is given in parenthesis.

Table 8: Influence of the impurities CO, CO₂, H₂O, NH₃, C₂H₆ on the rate of permeation of hydrogen through a palladium/silver permeator of 289 cm² surface area at various temperatures

Development of ECRH Power Sources

The KfK 150 GHz gyrotron with a 10 mm diameter resonator has been operated in an extended test programme. Pulsed operation of this tube, mainly with 0.5 msec pulse length, was reproducibly achieved and a parameter optimization has been carried out.

The experimental set-up has been improved compared to the previous measurements. The integral tube has been heated for the first time to 280°C in an inert gas furnace to improve the beam vacuum. The positive result after this procedure was, that due to the better vacuum the formation of the whole system necessary for beam operation took less time. The original imperfect superconducting magnet system was replaced by a new superconducting magnet system which reliably reached the designed field profile and absolute value of the magnetic field. The new cryogenic system could be operated without any difficulties and with significantly lower losses.

In addition, the rf-diagnostics were improved. Especially, a very accurate frequency measurement with a high resolution frequency counter allowed to measure the frequencies with a resolution of several MHz, i.e. 10^{-5} .

The rf-power in the TE032-mode as a function of beam current has been measured reproducibly for different magnetic field values and optimized modulation voltage. As an example, typical results are summarized in Fig. 85. A

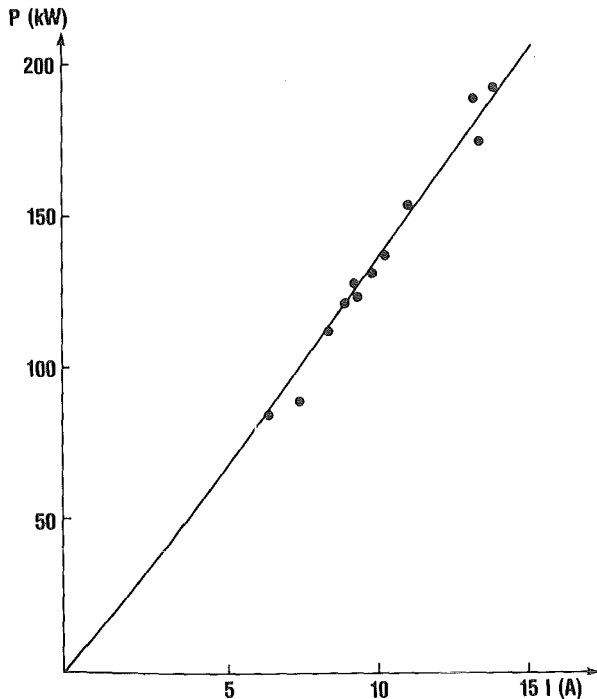


Fig.85: Rf-power as a function of beam current in the TE032-mode.
 $B = 5.88 \text{ T}$, $U_b = 76.5 \text{ kV}$, $U_{mod} = 22 \text{ kV}$,
 $\alpha = 1.0$

maximum output rf-power of 200 kW at 14 A beam current seems to be the present limit with the 10 mm resonator. This corresponds to previous measurements. The efficiency was again in the range of 20%.

The rf-power as a function to the magnetic field is given in Fig. 2 together with the results of self-consistent calculations for two different values of α . The agreement between theory and experiment is satisfactory. The influence of α is evident from Fig. 86 and, also, the narrow range of the magnetic field for the T032-mode excitation in the 10 mm resonator.

For optimization of the oscillation two superconducting beam steering magnets have been used and different start-up conditions have been tested. Mode competition even at low beam current was an additional difficulty. Recent calculations indicate an explanation for this behaviour of the resonator. Experimentally it was found that the oscillation regions of the TE031- and TE032-mode overlapped completely.

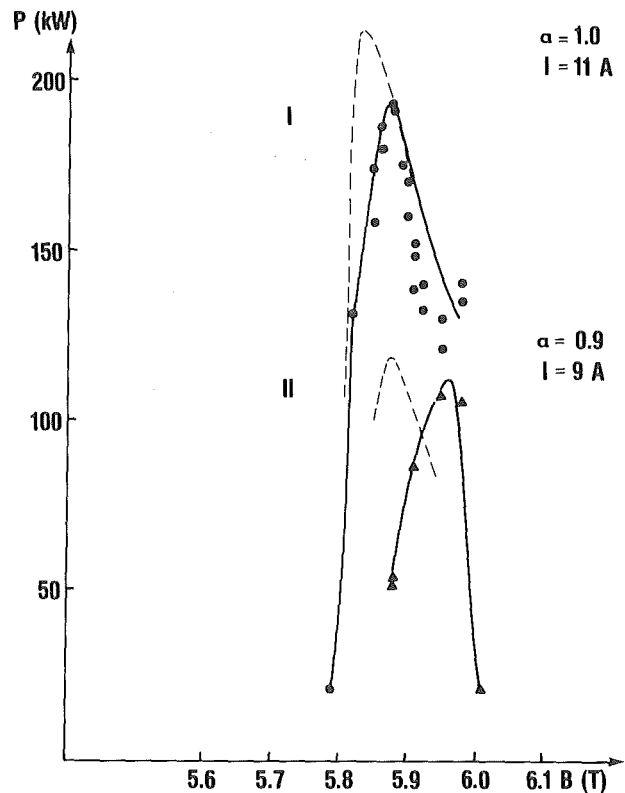


Fig. 86: Rf-power as a function of magnetic field for $I = 13 \text{ A}$, $\alpha = 1.0$ (I) and $I = 8.4 \text{ A}$, $\alpha = 0.8-0.9$ (II) in the TE032-mode

At a very low current ($< 1 \text{ A}$) the TE031-mode started first, but at a slightly higher current (2-3A) the TE032-mode dominated the gyrotron oscillation completely. The maximum rf-power was measured in the TE032-mode, also.

After baking and realignment of the tube, the frequencies of the TE23- and TE52-mode were found to be 147.68 GHz

and 155.78 GHz, higher than the calculated frequencies, whereas the frequencies of the TE031- and TE032-mode were measured to be 149.74 GHz and 150.67 GHz respectively. This is in both cases 0.4 GHz lower than the calculated frequencies.

After disassembly of the experimental setup a possible reason for this discrepancy turned out to be a change in resonator geometry. The electron beam had partially melted the wall in the region of the entrance taper in such a way, that some copper particles of ~ 0.1 mm size stucked to the resonator wall and may have caused the deterring.

In the meantime construction of the new 140 GHz modular gyrotron with a redesigned electron gun and a tunable window has been completed. The tube has been assembled and heat treated at 460°C in the furnace. The experimental programme will start shortly.

The industrially fabricated prototype gyrotron for 100 ns pulse length is under construction including a new improved electron gun and tunable window. For this prototype, a separate superconducting magnet system is in fabrication.

Staff:

W. Baumgärtner	A. Hornung
E. Borie	B. Jödicke
H. Budig	M. Kuntze
G. Dammertz	R. Lehm
O. Dumbrais	N. Münch
U. Feißt	H. Oppermann
T. Geist	B. Piosczyk
P. Grundel	G. Redeman
R. Hietschold	R. Vincon
<u>G. Hochschild</u>	H. Wenzelburger

NET Study Contracts

Availability of the LCT Plant

Representative test results were described in the joint summary report of the Large Coil Task edited by participants of the LCT described in M 1.

The evaluation of the availability of the LCT plant is content of chapter 4 of this report [1].

[1] P.N. Haubenreich et al.

The IEA Large Coil Task, Development of Superconducting Toroidal Field Magnets for Fusion Power.

Fusion Engineering and Design 7, 1988, Special Issue

Staff:

A. Ulbricht

P.N. Haubenreich, ORNL

Investigation of the Vacuum and Exhaust Performance of NET

The work concentrates at present on the development of the DWELLMAP-Code intended to simulate the vacuum performance during dwell time. In conformity with the envisaged strategy aimed at making increasing use of personal computers (to ease the cooperation and the program transfer to the NET team), the whole process from burn to dwell time was subdivided into the following five subsequent partial processes and implemented on the personal computer:

Burn time:

to calculate the build up of the fuel gas content in the wall materials and to provide valid start conditions.

Stretch out time:

to simulate the effects of the decreasing plasma density during the shut down period.

Confinement loss time:

to simulate the short transition period when the confinement breaks down and the plasma ions become mixed with the halo content.

Mixing time (supplement to the confinement loss time):

to smooth down any residual inhomogeneity within the plasma chamber.

Dwell time:

to simulate the evacuation process of the whole plasma chamber.

The partial processes are investigated independently, any follow up module reads its main input from a data transfer file written by the preceding module.

To ease the understanding and the handling of the code system, a stepwise approach was selected, starting with a simple zero-version of the program (neglecting any plasma-wall interaction) and proceeding towards increasing complexity. At present, a version which includes the plasma wall interaction in a first approach is available. However, with graphite as wall material, the subroutines describing the "pump and dump" behaviour of the plasma viewing surfaces must be further improved.

Staff:

R.A. Müller

Study about the NET TF Pancake Test

The design and optimization of the TWIN configuration is in progress. The arrangement consists of a NET TF model coil and one LCT coil (Fig. 87). To achieve the required field

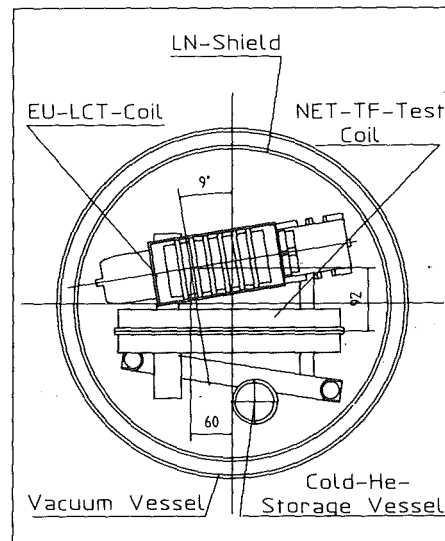


Fig. 87: The TWIN test configuration consisting of the Euratom LCT coil and the TF conductor model coil.

strength of 11 T in a reasonable volume of the model coil operation of the LCT coil at a field strength of 10-11 T is needed. It was already investigated that the stress levels in the EURATOM LCT coil will be acceptable if a suitable support structure would be provided. In a second step the electrical and thermohydraulic behaviour was investigated for operation up to 20 kA. According to the test results of the EURATOM LCT coil and the extrapolation to 1.8 K the coil can reach the expected field level. The current leads of the EURATOM LCT coils are capable to carry not only the higher current but also the higher forces. Under the assumption of a realistic length of a normal region (~ 3 m) according to the test results of the Euratom LCT coil quench

Table : Comparison of the operation parameter of the Cluster and TWIN

	Units	CLUSTER C6		TWIN	
		NET-TF Model Coils (KfK/SULTAN)	EU-Coil	NET-TF Model	EU-Coil
Minimum bending radius for TF Model coil	[m]	1.0	not important	1.0	not important
Temperature (Inlet)	[K]	3.5/3.5	3.5	3.5	1.8
Conductor current	[kA]	22	13	22	18
Total coil current	[MA]	4.488/4.84	7.644	9.856	10.584
Magnetic field at reference point of winding pack	[T]	12.1/12.0	8.3	11.69	10.33
Force in x-direction (centering force)	[MN]	-68.7	37.5	-18.5	18.5
Force in y-direction (out-of-plane force)	[MN]	1.5	-86.6	115.2	-115.2
Stored self energy	[MJ]	34/38	134	138	253
Total stored energy	[MJ]	51	2	50	7
Rotation angle to x-direction	[degree]	0/0	14	0	9

Table 9: Comparison of the operation parameter of the Cluster and TWIN configurations

pressures remain moderate. The safety discharge of the coil can be handled with a discharge voltage of 2,5 kV. However, the TF model coil will be exposed to considerably higher out-of-plane forces (Tab. 9) than in the cluster configuration analyzed previously. This needs a detailed mechanical finite element analysis of the coils which was initiated.

- Staff:
 A. Grünhagen
 W. Herz
 K. Jentzsch
 W. Maurer
 A. Ulbricht
 A. Vogt
G. Zahn

Evaluation of Crack Growth Delay in Multilayers Sheets

Objectives of the Contract

For the first wall multilayer structures are a subject of discussion. Two metallic plates or tubes are bonded together by a soft intermediate layer. This soft layer possibly could arrest or at least delay a growing crack, such that a through-the-wall crack, providing a leak, is avoided. The multilayer structure thus could have the effect of a double containment.

As metallic material the austenitic steel 316 L was used. For the intermediate layer copper was selected because of its thermal expansion coefficient. The three-layer-component consists of a 2mm thick plate of copper, which is sandwiched by two plates of steel, which both have a thickness of 7mm. The sheets were welded together by explosive bonding.

Experimental Results for Explosive Bonded Structure

Specimens of a plate type were machined from multilayer sheets and tested in four-point-bending tests.

Semi-elliptical starter notches were introduced and fatigue crack growth was investigated for different load amplitudes and loading modes. Thus near the interface between steel and copper crack propagation rates of 10^{-6} mm to 10^{-5} mm per load cycle were produced

In all tested specimens the crack propagated as a semi-elliptical surface crack through the stainless steel plate until the copper layer was reached. After reaching the soft layer the crack branched and extended in the copper perpendicular to its direction in the steel part.

- Staff:
 G. Balzer
E. Diegele
 T. Fett
 S. Müller

CAD Data Exchange between NET and KfK

The design of NET is to a large degree done by means of computer aided design (CAD) systems. Since NET and KfK use dissimilar CAD systems a neutral CAD data exchange interface IGES (Initial Graphics Exchange Specification) is used for exchange of NET drawing data. Both the NET CAD system MEDUSA and the KfK CAD system BRAVO3 have IGES pre- and postprocessors which write and read the IGES file. However, the IGES specification is rather ambiguous and the IGES processors are not bug-free. It is the objective of the contract to improve the data exchange via IGES between NET and KfK.

The analysis of the IGES processors of the MEDUSA system has been finished. A user-interface for the MEDUSA IGES preprocessor has been developed that sets the processor parameters to achieve optimal transfer when the name of the receiving system is given as input.

To analyze the IGES processors of the APPLICON BRAVO3 system a number of testparts has been created similar to the testmatrix for MEDUSA. The transfer of drawing data from BRAVO3 preprocessor and translating this IGES file into a MEDUSA sheet file via the MEDUSA postprocessor. The resulting drawing in the MEDUSA system is compared with the original in BRAVO3. This leads also to a set of recommendations for users of the BRAVO3 system, which entities should be avoided to achieve optimal transfer.

To take care of those entities causing problems in the transfer which cannot be avoided by recommendation and appropriate setting of processor parameters a software package has been developed that allows to modify the IGES file. This software package, called MODIGS is completely system independent. It reads an IGES file, allows to alter parameters of individual entities or sets of entities and to remove entities from the file. The output of the system is a modified IGES file.

Staff:

U. Gengenbach

S. Haas

A. Ludwig

CAD Data Exchange for ITER

This work was undertaken upon request by the NET-Team as a consequence of the increasingly close cooperation between US and European fusion reactor design teams in the ITER project. In the US fusion community, the CADD54X CAD system is used while the NET Team uses the Medusa CAD system. The task of this contract was to provide for communication of CAD data between these groups. The work was completed in August 1988. A final report (Primärbericht 03.01.01P58A) has been delivered to the NET Team as well as the communication software.

Work under this contract comprised the following main activities:

- 1) identification of the essential communication needs and appropriate file formats: two-dimensional design drawings are predominant; the IGES file format was chosen as a basis.
- 2) Investigation of Medusa and its IGES processors: Most of the relevant information was already available from the work done for the CAD data exchange between KfK and the NET Team
- 3) Investigation of CADD54X and its IGES processors.
- 4) Identification of the common entity sets and the entities which cause communication problems: Two test matrices (one for each direction) were established and analysed.

5) Recommendations for minimization of communication problems.

6) Development of utility software for mailing CAD files via public package switching networks.

Staff:

W. Reichert

S. Haas

U. Gengenbach

NET Blanket Handling Device

Within the frame of the NET contract 282/87-10FU D NET, NET Blanket Handling Device, KfK has continued the investigation of handling concepts for blanket segments which will result in a preliminary specification and pre-design of the required equipment. The final report is in preparation.

The Requirement Definition Document which was transmitted to the NET Team as an intermediate report was completed with respect to

- the changed geometrical conditions of the blanket segments,
- the specification of the geometrical environment in the area of blanket segment attachment for handling,
- the consideration of a changed shielding concept in the area of blanket handling.

Based on the valuation of available handling concepts proposed by CEA and own alternative solutions a reference handling concept was investigated and the handling device pre-designed (Figure 88 and Figure 89).

The handling device has a support structure with a crane bridge which is guided at four rods and vertically movable on the crane bridge in the two horizontal directions by means of electric motors. It is equipped with an electrically actuated rotation joint at which the lever system is mounted via a pitch joint to compensate excentric loads. The system is operated by an electric actuator. The 6 degrees of freedom of the complete system fulfil all requirements for blanket withdrawal and insertion sequences. The handling device is enclosed in a contained transfer unit which is mounted on the rotatable support and shielding structure. Transport flasks for the contamination-free transfer of the blanket segments are attachable to the contained transfer unit.

In order to reduce the required height of the handling device two alternative options to the reference concept were investigated. Their conceptual design, as well as the results of investigations concerning the attachment of the

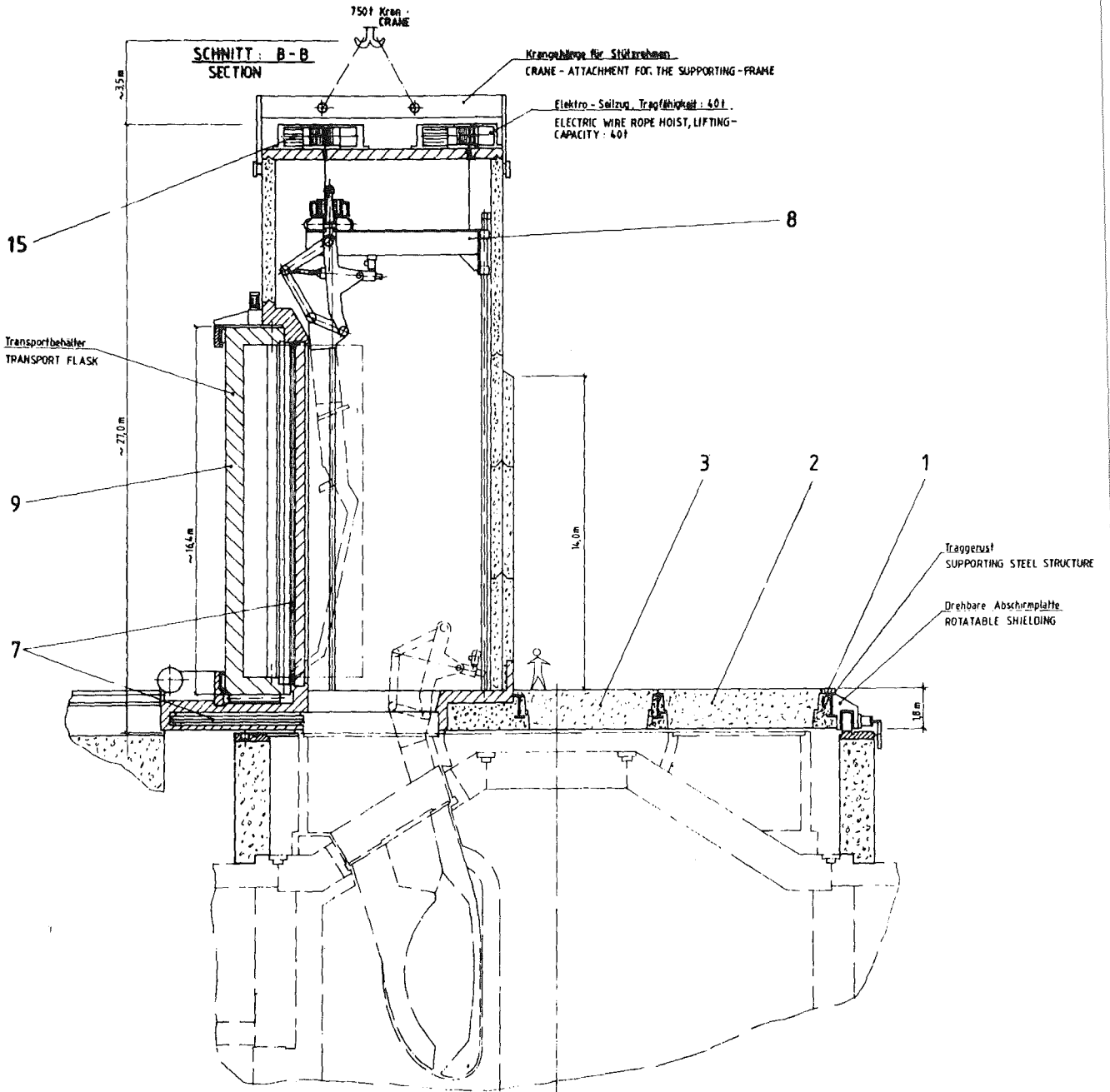


Fig. 88 Blanket handling device - reference concept

blanket segments to the handling device will be integrated in the final report.

Staff:

B. Haferkamp

W. E. Hörl

J. Hübener

W. Link

A. Suppan

Schnitt B - B
SECTION

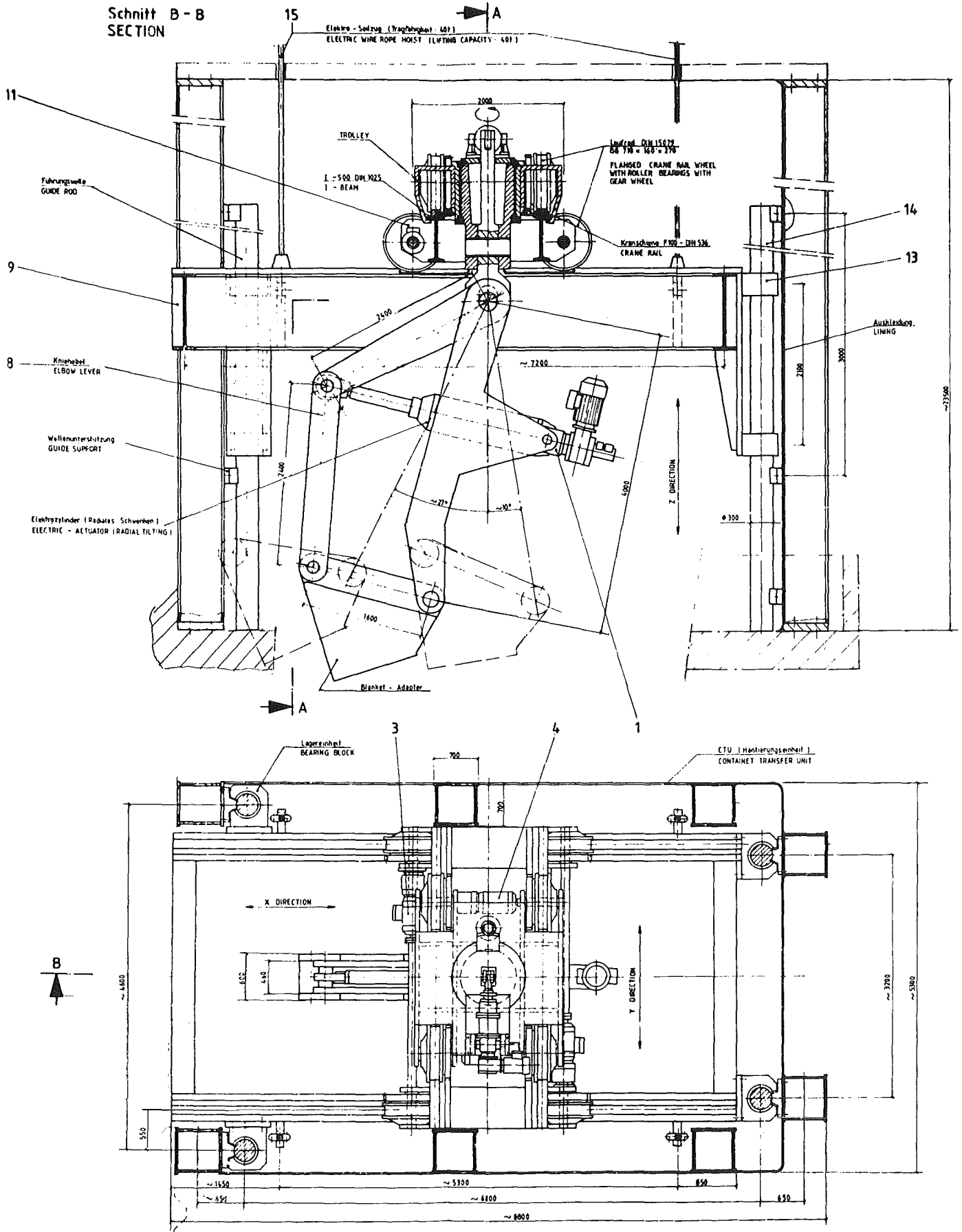


Fig.89: Blanket withdrawal device - reference concept

Appendix I: Table of Fusion Technology Contracts

Task Code No.	Title	KfK Departments
B1	Blanket Design Studies	IMF III, INR, IRB, IT
B 2	Development of Computational Tools for Neutronics	INR
B6	Corrosion of Structural Materials in Flowing Pb-17Li	IMF I, IMF II
B 6.3	Fatigue of Structural Material in Pb-17Li	IMF I, IMF II
B9	Tritium Extraction from Liquid Pb-17Li by the Use of Solid Getters	IT
B 11-16	Development of Ceramic Breeder Materials	IMF I, IMF III, INR, IRCH
B 15.3	End of Life of Solid Breeding Materials in Fast Neutron Flux	IMF I, IMF III, INR
M1	The Large Coil Task	ITP
M 3	Development of High Field Composite Conductors	ITP
M 4	Superconducting Poloidal Field Coil Development	ITP
M 8	Design and Construction of a Poloidal Field Coil for TORE SUPRA as NET-Prototype Coil	ITP
M 9	Structural Materials Fatigue Characterization at 4 K	ITP
M 12	Low Electrical Conductivity Structures Development	IMF IV, ITP
MAT 1.6	Development and Qualification of MANET 1	IMF II
MAT 1.9	Pre- and Post-Irradiation Fatigue Properties of 1.4914 Martensitic Steel	IMF II
MAT 1.11	Post-Irradiation Fracture Toughness of Type 1.4914 Martensitic Steel	IMF II
MAT 2.2	In-Pile Creep-Fatigue Testing of Type 316 and 1.4914 Steels	IMF II, IMF III
MAT 6/ MAT 13	Ceramics for First-Wall Protection and for RF Windows	IMF I
MAT 9.2	Investigation of Fatigue Under Dual Beam Irradiation	IMF II
MAT 18	Development of Low Activation Ferritic-Martensitic Steels	IMF II
N1	Design Study of Plasma Facing Components	INR, IRB, IRE
N2	Shield Design Studies	IMF III
N3	Development of Procedures and Tools for Structural Design Evaluation	IMF IV
N5	Development of Theory and Tools for Evaluation of Magnetic Field Effects on Liquid-Metal Breeder Blankets	IRB

N6	Studies of Pebble Beds of Ceramic Compounds	INR
RM1	Background Studies on Remote Maintenance	IT
RM2	Mechanical Components Assembly	IT
RM 3	Handling Equipment for In-Vessel Components	IDT, IRE, IT
S + E 4.1.2	Safety Aspects of the Cryosystem	IRE
S + E 4.1.3	Safety Aspects of Superconducting Magnets	IDT, IRE, ITP
S + E 5.4	Overall Plant Accident Scenarios for NET	IRE
S + E 5.5	Development of Safety Guidelines for the Design of NET	IRE
S + E 7	Generic Environmental Impact Assessment for a Fusion Facility	INR, IMK
T 6	Industrial Development of Large Components for Plasma Exhaust Pumping	IT
T 7	Optimization of Cryogenic Vacuum Pumping of Helium	IT
T 10 A	Plasma Exhaust Purification by Means of Cyrosorption on Molecular-Sieves or Alternative Adsorbents	IRCH
T 10 C	Plasma Exhaust Gas Purification by Use of Hot-Metal Getters	IRCH
T 10 E	Adsorption of DT on Heated Metal Beds other than Uranium	IRCH
T 10 H	Catalyst Development for the Exhaust Purification Process	IRCH
Development of ECRH Power Sources (This task is part of the Fusion Physics Programme of the EC.)		IDT, ITP

Appendix II: Table of NET Contracts

Theme	Contract No.	Working Period
Study about the NET TF Pancake Test	240/86-6 FU-D/NET	05/86 - 04/88
Evaluation of Crack Growth Delay in Multilayer Sheets	253/86-11/FU-D/NET	11/86 - 09/88
CAD Data Exchange between NET and KfK	265/87-3/FU-D/NET	03/87 - 09/88
CAD Data Exchange for ITER	285/88-1/FU-D/NET	01/88 - 04/88
Study of a Plasma Exhaust Purification System for NET based on Catalytic Reduction of Impurities: Phase 1 Conceptual Study	272/87-8/FU-D/NET	10/87 - 03/88
NET Blanket Handling Device	282/87-10/FU-D/NET	11/87 - 10/88
Electrical Connectors for Remote Handling	313/88-7 FU-D/NET	09/88 - 05/89

Appendix III: KfK Departments contributing to the Fusion Project

Kernforschungszentrum Karlsruhe GmbH Telephone (07247) 82-1
 Postfach 3640 Telex 7 826 484
 D-7500 Karlsruhe 1 Telefax/Telecopies (0) 07247/825070
 Federal Republic of Germany

KfK Department	KfK Institut/Abteilung	Director	Ext.
Institute for Data Processing in Technology	Institut für Datenverarbeitung in der Technik (IDT)	Prof. Dr. H. Trauboth	5700
Institute for Materials and Solid State Research	Institut für Material- und Festkörperforschung (IMF)	I. Prof. Dr.K.-H. Zum Gahr	3897
		II. Dr. K. Anderko	2902
		III. Prof. Dr.K. Kummerer	2518
		IV. Prof. Dr. D. Munz	4815
Institute for Neutron Physics and Reaktor Engineering	Institut für Neutronenphysik und Reaktortechnik (INR)	Prof. Dr. G. Keßler	2440
Institute for Reaktor Components	Institut für Reaktorbau- elemente (IRB)	Prof. Dr.U. Müller	3450
Institute for Radiochemistry	Institut für Radiochemie (IRCH)	Prof. Dr. H.J. Ache	3200
Institute for Reaktor Development	Institut für Reaktor- entwicklung (IRE)	Prof. Dr. D. Smidt	2550
Central Engineering Department	Hauptabteilung Ingenieur- technik (IT)	Dr. H. Rininsland	3000
Institute for Technical Physics	Institut für Technische Physik (ITP)	Prof. Dr. P. Komarek	3500
Institute for Meteorology and Climate Research	Institut für Meteorologie und Klimaforschung	Prof. Dr. F. Fiedler	2093

Appendix IV: Fusion Project Management Staff

